JSCSEN 86(4)341–444(2021)

ISSN 1820-7421(Online)

Journal of the Serbian Chemical Society

Electronic version

VOLUME 86

No 4

BELGRADE 2021

Available on line at

www.shd.org.rs/JSCS/

The full search of JSCS is available through

DOAJ DIRECTORY OF OPEN ACCESS JOURNALS

www.doaj.org

Journal of the Serbian Chemical Society
JSCS-info@shd.org.rs • www.shd.org.rs/JSCS

J. Serb. Chem. Soc. Vol. 86, No. 4 (2021)

CONTENTS*

Published by the Serbian Chemical Society
Karnegijeva 4/III, P.O. Box 36, 11120 Belgrade, Serbia
Printed by the Faculty of Technology and Metallurgy
Karnegijeva 4, P.O. Box 35-03, 11120 Belgrade, Serbia

* For colored figures in this issue please see electronic version at the Journal Home Page: http://www.shd.org.rs/JSCS/

Journal of the Serbian Chemical Society
JSCS-info@shd.org.rs • www.shd.org.rs/JSCS
J. Serb. Chem. Soc. *86* (4) 341–353 (2021)
JSCS–5425
Survey

SURVEY

Permeability of gas mixtures in glassy polymers with and without plasticization

MASOUD SABERI*

Department of Chemical Engineering, Bushehr Branch, Islamic Azad University, Bushehr, Iran

(Received 15 July, revised 31 July, accepted 4 August 2020)

Abstract: In this research, the solubility, permeability and diffusivity of gas mixtures through glassy polymers were comprehensively studied. The diffusivity of the components in the mixture was assumed to be a function of the concentration of all components in the mixture. Then, the permeability of pure species was expanded to the gas mixtures and to check the validity, the model was fitted to the experimental data for permeation of CO_2/CH_4 through different glassy membranes and the parameters of the model were calculated. Afterwards, the obtained parameters were used for predicting the permeability of CO_2 and CH_4 in the mixture. The results showed that the solubility, diffusivity, and the permeability of CO_2 in the glassy polymers are suppressed in the presence of CH_4 as well as plasticization. Moreover, the diffusivity (D) for pure CO_2 is significantly pressure dependent in the presence of plasticization whereas with the increase in the CH_4 fraction, this dependency decreases due to the reduction in the plasticization.

Keywords: gas separation; membrane; plasticization; solubility; diffusivity.

INTRODUCTION

Polymeric membranes are widely used in the natural gas separation process. For removal of carbon dioxide (CO_2), glassy polymeric membranes are often preferred over rubbery polymeric membranes because of their higher CO_2/CH_4 or CO_2/N_2 selectivity.[1–6] Although some types of glassy membranes have a good performance in CO_2 separation, the performance of these membranes can be hindered by the plasticization phenomenon.[7–12] Therefore, CO_2 permeability increases with the feed pressure.[7–13] On the other hand, permeability of pure inert gases, such as CH_4 or N_2, has a decreasing trend with the pressure.[14–16] Thus, the ideal selectivity of CO_2/N_2 or CO_2/CH_4 increases with feed pressure.[13–16] However, the behavior of mixed gas feeds is significantly different from pure

* E-mail: msd.saberi@gmail.com
https://doi.org/10.2298/JSC200715046S

species. In the presence of plasticization, the permeabilities of both CO_2 and N_2 or CH_4 increase. But N_2 or CH_4 generally have larger increases than CO_2, resulting in decreasing selectivity.[1,10,14,17,18] Thus, the actual selectivity is lower than ideal selectivity at a special pressure.[1,14,19] Raymond *et al.*[19] reported that for mixed gas feed of CO_2 and CH_4 with equal composition, the actual selectivity at 5 atm* is well predicted by pure gases, whereas at 20 atm, the actual selectivity was much lower than ideal selectivity. It was due to plasticization of membranes at 20 atm pressure. In addition, ideal selectivity of CO_2 and CH_4 for polyimide (6FDA-mPD) was reported to be about 60 at a feed pressure of 17.5 atm, whereas the actual selectivity for feed with equal composition of these gases was observed about 4.[20]

Therefore, for a proper prediction of transport behavior for gas mixtures, especially in the presence of plasticization, it is essential to represent accurately the experimental results. Then, an accurate and simple model is required to be used for all the different behaviors of gases in glassy polymers.

Different approaches were developed to describe the solubility and transport of gases and vapors in glassy polymers. Among these models, the dual mode sorption (DMS) and non-equilibrium lattice fluid (NELF) models are well-known models. It should be mentioned that, although NELF model has been extended for all permeability behavior of gaseous in glassy polymers, it is used less than the DMS model because of its complexity and long calculation times. DMS, a model with empirical parameters, is widely used mainly due to its remarkable simplicity. Although, different models with different assumptions have been developed based on this theory to investigate the permeability of pure and mixed gases in glassy polymers, less attention has been paid for predicting permeation of mixed gases through glassy polymers in the presence of plasticization. In our previous works, we extended a model for permeation of gas mixtures in glassy polymers based on DMS model with no predictive capability.[21,22] In the present study, a comprehensive model based on the DMS model was developed to predict the permeation behavior of mixed gases through glassy polymers with and without plasticization using pure data for solubility and permeability. To achieve this aim, the diffusivity of all species in the mixture is assumed to be a function of the concentration of all components in the mixture. Then, for determining the parameters and evaluation of the accuracy of the model, the predictions of the model were compared against experimental data for the permeation of different groups of gas mixture in different glassy polymers.

* 1 atm = 101325 Pa

THEORY AND BACKGROUND

Solubility

Based up on the DMS model, two mechanisms of sorption occur in glassy polymers: *i*) ordinary dissolution based on the Henry's law and *ii*) "hole-filling" according to the Langmuir theory. The equilibrium isotherm for a pure gas A based on the DMS model is expressed as:[21-23]

$$C_A = C_{DA} + C_{HA} = k_{DA} p_A + C'_{HA} b_A p_A / (1 + b_A p_A) \quad (1)$$

where C is the gas concentrations in the polymer (cm^3 STP/cm^3 polymer), C_D is the Henry's solubility, represents ordinary dissolution, C_H is Langmuir solubility, represents sorption in microvoids or holes, k_D is Henry's law solubility coefficient (cm^3 STP/cm^3 polymer.atm), C'_H is the hole saturation constant (cm^3 STP/cm^3 polymer), b is the hole affinity constant (atm^{-1}) and p is pressure (atm). The solubility coefficient of gas A in polymeric membranes is defined as:[21,22]

$$S_A = C_A/p_A \quad (2)$$

Koros *et al.* extended the DMS model for gas mixture systems and the sorption of components A and B of a binary gas mixture is expressed as:[23]

$$C_A = k_{DA} p_A + C'_{HA} b_A p_A / (1 + b_A p_A + b_B p_B) \quad (3)$$

$$C_B = k_{DB} p_B + C'_{HB} b_B p_B / (1 + b_A p_A + b_B p_B) \quad (4)$$

Permeability

Based on the partial immobilization model (PIM), a fraction F of the sorbed gases in the Langmuir sites are mobile and the remainder ($1-F$) are immobile whereas the whole gas dissolved in the Henry's region is mobile. The total concentration of the mobile part of the adsorbed gas is C_m with a diffusion coefficient D. F is the immobilization factor and depends on the nature of penetrant–polymer system as well as the system temperature.[24,25]

The flux (N) of component i is expressed as follows:[21]

$$N_i = -D_i\left(\frac{\partial C_{mi}}{\partial x}\right) \quad (5)$$

where:[21]

$$C_{mi} = C_{Di} + F_i C_{Hi} = k_{Di} p_i + F_i C'_{Hi} b_i p_i / (1 + b_i p_i) \quad (6)$$

For the diffusivity of species i, a simple exponential relationship with the penetrant mobile concentration was found effective and is given by:[26,27]

$$D_i = D_{i0}\exp(\beta_i C_{mi}) \quad (7)$$

where D_{i0} is the diffusion coefficient of pure gas at zero penetrant concentration, and β_i is the plasticization factor.

It should be noted that Eq. (7) could be used for all gases, including plasticizer or not. In the absence of plasticization (*i.e.*, $\beta_i = 0$), diffusivity will be constant and would not change with pressure.

Then, Eqs. (5)–(7) yield the following expression for the flux of the penetrant gas in glassy polymers:

$$N_i = -\frac{D_{i0}}{l}\int_{C_{mi1}}^{C_{mi2}} \exp(\beta_i C_{mi})\,\mathrm{d}C_{mi} \quad (8)$$

where subscripts 2 and 1 represent the upstream and downstream conditions and when the downstream pressure is considered zero, $C_{mA1} = 0$.

Toni *et al*. considered the two mobility coefficients related to the concentration of both penetrants,[28] whereas the diffusivities for components A and B in the binary gas mixture were assumed to be related to the concentration of both penetrants and obtained by:

$$D_A = D_{A0}\exp(\beta_A C_{mA} + \beta_B C_{mB}) \quad (9)$$

$$D_B = D_{B0}\exp(\beta_A C_{mA} + \beta_B C_{mB}) \quad (10)$$

where D_{A0}, D_{B0}, β_A and β_B were obtained from pure state, and:

$$C_{mA} = C_{DA} + F_A C_{HA} = k_{DA} p_A + F_A C'_{HA} b_A p_A / (1 + b_A p_A + b_B p_B) \quad (11)$$

$$C_{mB} = C_{DB} + F_B C_{HB} = k_{DB} p_B + F_B C'_{HB} b_B p_B / (1 + b_A p_A + b_B p_B) \quad (12)$$

Again, combining Eq. (5) and Eqs. (9)–(12) and integrating, yields the following expression for the flux of components A and B in glassy polymers:

$$N_A = -\frac{D_{A0}}{l}\int_{C_{mA1}}^{C_{mA2}} \exp(\beta_A C_{mA} + \beta_B C_{mB})\,dC_{mA} \quad (13)$$

$$N_B = -\frac{D_{B0}}{l}\int_{C_{mB1}}^{C_{mB2}} \exp(\beta_A C_{mA} + \beta_B C_{mB})\,dC_{mB} \quad (14)$$

It is worth mentioning that for integrating Eq. (13), C_{mA} and C_{mB} should be written in term p_A and for Eq. (14) should be written in term p_B.

Furthermore, under steady state conditions, the permeability and selectivity are given by:[22]

$$P_i = \frac{N_i l}{p_{i2} - p_{i1}} \quad (15)$$

where l is the membrane thickness.

RESULTS AND DISCUSSION

The mathematical procedure to predict the permeation of mixed gas through glassy polymeric membranes is as follows:

1. Calculation of parameters of the DMS model (Eq. (1)) for pure species by fitting this equation to the experimental data of the isotherms.

2. Using the obtained parameters from step 1, fitting Eq. (8) to the experimental data for permeability of pure species and the calculation of parameters β, F and D_0 for the pure species.

3. Using the obtained parameters of steps 1 and 2 in conjunction with Eqs. (13) and (14), for the prediction of the permeability of the species in the gas mixture.

It is worth noting that the parameters of the DMS model and the non-linear proposed models are obtained by the least squares regression technique using MATLAB software.

To validate the model, comparing with the experimental data for the permeation of CO_2/CH_4 mixtures through different glassy membranes including poly-

sulfone (PSf), polyetherimide (PEI), polyhydroxyether (PH), polyarylate (PAr) and cellulose acetate (CA) are investigated.[15,29–31]

Solubility

In order to study the permeability behavior of CO_2/CH_4 gaseous mixture, the parameters of the sorption isotherm of pure CO_2 and CH_4 in the glassy polymers is required. The DMS parameters for CO_2 and CH_4 in the different glassy polymers, which were obtained by fitting the DMS model to the experimental data, are reported in Table I. Then, by consideration the parameters of Table I, and using Eqs. (3) and (4), the solubility of the species in the gas mixture were predicted.

TABLE I. DMS parameters for pure CO_2 and CH_4 in the different glassy polymers at 35 °C

Polymer	Gas	k_D / (cm^3 STP/(cm^3 atm))	C'_H / (cm^3 STP/cm^3)	B / atm^{-1}	Reference
PSf	CO_2	0.664	17.91	0.326	29
	CH_4	0.161	9.86	0.070	
PH	CO_2	0.289	10.01	0.184	29
	CH_4	0.051	2.70	0.067	
PEI	CO_2	0.758	25.02	0.366	29
	CH_4	0.207	7.31	0.136	
PAr	CO_2	0.631	22.69	0.215	29
	CH_4	0.181	6.45	0.100	
CA	CO_2	1.362	22.58	0.248	15
	CH_4	0.190	2.504	0.132	

As mentioned in a previous work,[21,22] the solubility–pressure isotherm for CO_2 and CH_4 and their mixtures in glassy polymers, at lower pressures severely increases and with increasing pressure, a decrease in the sorption slope occurred. For higher pressures, this slope is almost constant and the sorption isotherm changes linearly, like the sorption of gases in rubbery polymers. This trend of sorption is because at low pressures, gas molecules adsorbed in the Henry and Langmuir sites and for higher pressures Langmuir sites will be occupied. For gas mixtures, the presence of the second component (*i.e.*, CH_4) inhibited the sorption of first component (CO_2) by occupation of some sites of the Langmuir portion. Then, the sorption of CO_2 is suppressed by the presence of CH_4 in the mixture (Fig. 1).

The solubility selectivity of CO_2/CH_4 *vs*. pressure is shown in Fig. 2. Solubility selectivity is found to be significantly higher in mixtures compared to the pure condition. This could be attributed to competitive sorption whereby the solubility of CO_2 decreases in the presence of CH_4 as well as CH_4. It should be mentioned that the decrease in CH_4 solubility is more than that of CO_2 solubility due to higher hole affinity constant of CO_2 ($b_{CO_2}>b_{CH_4}$) resulting in an increase in the solubility selectivity. As could be observed, the ideal solubility selectivity

increases with increasing CH_4 fraction at constant pressure as reported by Vopicka *et al.*[20]

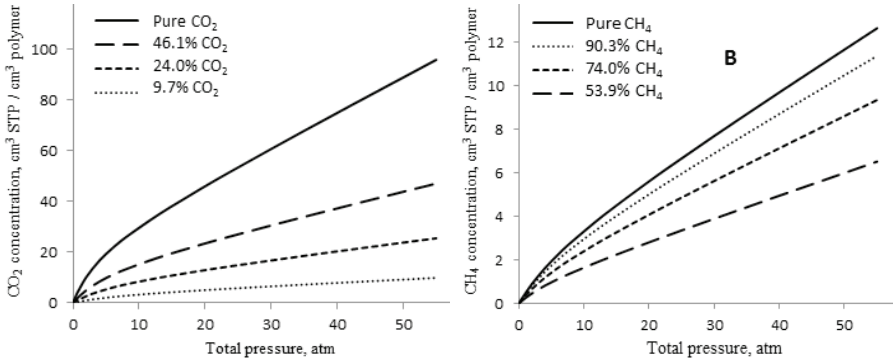

Fig. 1. Solubility of: A) CO_2 and B) CH_4 in CA glassy polymer.

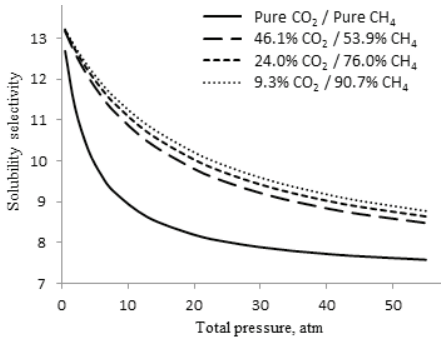

Fig. 2. Solubility selectivity of CO_2/CH_4 in CA glassy polymer.

Permeation without plasticization

The permeability of pure CO_2 and CH_4 in different glassy polymers was fitted using experimental data from the literature[30] and the parameters of the model, including β, F and D_0 for CO_2 and CH_4, are reported in Table II (also determined in the literature[30]). The permeability–pressure plots have a decreasing and/or constant trend in all cases. In these cases, there is no plasticization ($\beta = 0$), then, the diffusivity is constant. In this case when there was no plasticization, the decreasing and/or constant trends for permeability is related to the solubility coefficient and is controlled by the immobilization factor (F), which shows the mobile parts of the sorbed gas in the Langmuir region.

The predictions of the model for CO_2 and CH_4 gases of 50/50 volume ratio mixture in different glassy membranes using Eqs. (13) and (14) compared to the experimental data from the literature[31] are shown in Fig. 4a and b. At a glance, almost a small suppression in permeability in gas mixture is observed compared to the pure species. As mentioned above, solubility of species in the presence of

second component is reduced compared to pure species due to occupation of Langmuir sites, which resulted in a reduction in the diffusivity as well as permeability. An acceptable prediction for all cases could be observed.

TABLE II. Parameters of Eq. (8) for permeation without plasticization ($\beta = 0$)[30]

Polymer	Gas	F	$D_0 \times 10^8$ / cm^2 s^{-1}
PSf	CO_2	0.118	4.53
	CH_4	0.174	0.690
PH	CO_2	0.094	0.877
	CH_4	0.072	0.246
PEI	CO_2	0.063	1.14
	CH_4	0.073	0.113
PAr	CO_2	0.126	6.90
	CH_4	0.160	1.30

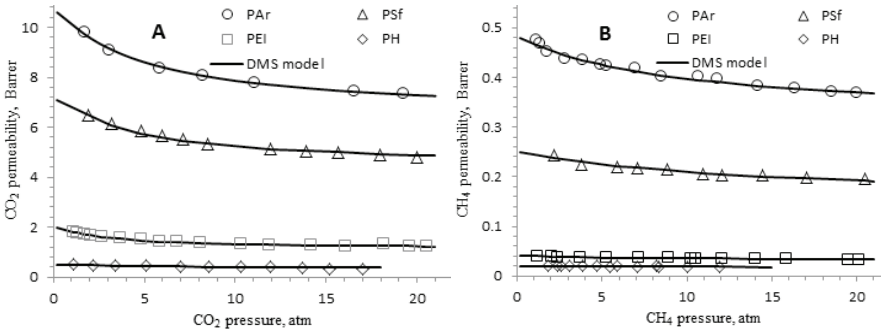

Fig. 3. Permeability of pure: A) CO_2 and B) CH_4 in different glassy polymers without plasticization (experimental data from the literature[30]).

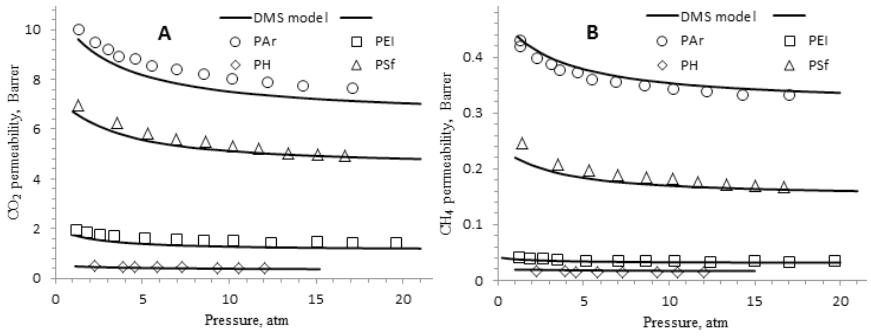

Fig. 4. Permeability of: A) CO_2 and B) CH_4 gases of 50/50 volume ratio mixture in different glassy polymers without plasticization (experimental data from the literature[31]).

Permeation with plasticization

Permeability. The permeability behavior of pure CO_2 and CH_4 through the CA membrane is shown in Fig. 5. These figures present experimental data from

the literature[15] with predictions of the model, calculated by Eq. (8), using the parameters β, F and D_0 for CO_2 and CH_4 listed in Table III. For pure CO_2, the permeability increases with increasing pressure due to the higher degree of plasticization of the CA membrane. Due to the high sorption of CO_2, which is a condensable gas, the polymer matrix swells and the interaction between adjacent segments of the polymer chain reduces. Therefore, due to the increase in segmental mobility and the free volume of polymer matrix, the diffusivity increases with increasing pressure. On the other hand, the solubility coefficient decreases with increasing pressure. Since, the increase in the diffusivity overcomes the decrease in solubility coefficient, CO_2 permeability increases with increasing pressure. For CH_4, which has low solubility in the membrane, the permeability decreases with increasing pressure. In this case, plasticization does not occur, and diffusivity is constant. On the other hand, the solubility coefficient decreases with pressure. Then, the permeability decreases with increasing pressure.

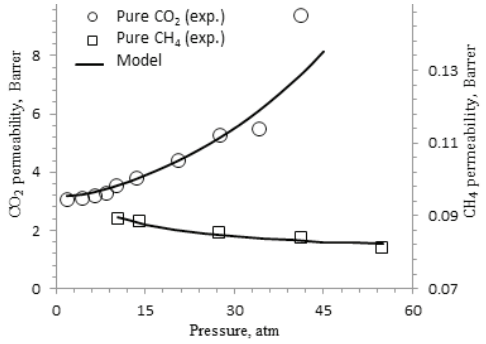

Fig. 5. Permeability of pure CO_2 and CH_4 penetrants in the CA membrane (experimental data from the literature[15]).

TABLE III. Infinite dilution diffusivity and plasticization factor for the various penetrants in the CA membrane

Polymer	Gas	β	F	$D_0 \times 10^7$ / cm^2 s^{-1}
CA	CO_2	0.031	0.06	1.45
	CH_4	0	0.38	0.29

In addition, comparing the experimental data for the permeability of CO_2 in the gas mixture feed with different compositions from the literature[15] and the predictions of the model using parameters from Table II is shown in Fig. 6.

For a feed with 46.1 % CO_2 and the rest CH_4, the permeability decreases with increasing pressure up to about 30 atm and then increases and 30 atm is called the “plasticization pressure”. The aforementioned solubility coefficient decreases with increasing pressure and in the presence of CO_2 as a plasticizer component, the diffusivity increases with increasing pressure. For a feed with 46.1 % CO_2, at pressures lower than 30 atm, the decrease in the solubility coefficient overcomes the increase in the diffusivity whereas at higher pressures, the

increase in the diffusivity dominates. Indeed, by adding CH_4 as the second component to the feed, some sites for sorption of CO_2 are occupied by CH_4 molecules so that the solubility of CO_2 in the mixture declines compared to pure CO_2. By suppression in the CO_2 solubility, diffusivity of CO_2 lowers at a specific pressure, consequently CO_2-induced plasticization decreases. It means that CH_4 in the feed acts as anti-plasticizer. For higher fractions of CH_4 in the feed, the effect of anti-plasticization increases and the permeability with the increase in the pressure decreases. Therefore, by introducing CH_4 to the feed, CO_2-induced plasticization is suppressed. As can be seen, the prediction of the model for permeability behavior is almost acceptable.

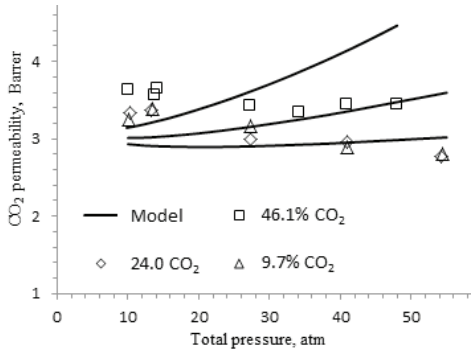

Fig. 6. Permeability of CO_2 in mixtures with different compositions *vs*. pressure, comparison between the experimental data from the literature[15] and the model prediction.

Moreover, the experimental data and the predictions of the model for CH_4 in gas mixture feeds with different compositions using parameters in Table II are compared in Fig. 7. As observed, for a feed with 53.9 % CH_4, the permeability of CH_4 passes through a minimum similar to the permeability of CO_2 in Fig. 3. This behavior is due to the presence of CO_2, which causes the membrane to plasticize. In addition, for feeds with higher fractions of CH_4, plasticization decreases due to the reduction of CO_2 sorption and diffusion, and hence, for feeds with the fractions higher than 53.9 % of CH_4, the CH_4 permeability decreases and/or is constant with increasing in pressure. Furthermore, with increasing CH_4 fraction in the feed, the CH_4 permeability at specific pressures is reduced following suppression

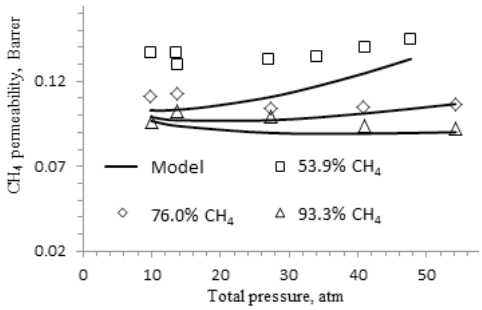

Fig. 7. Permeability of CH_4 in mixtures of different compositions *vs*. pressure, comparison between the experimental data from the literature[15] and the model calculation.

of plasticization.

Diffusivity

The estimated diffusivity *vs*. pressure for CO_2 and CH_4 in the pure state and in the gas mixture derived from Eqs. (9) and (10) using parameters from Tables I and II is illustrated in Fig. 8a and b. For pure CO_2, stronger dependency of D on pressure was observed, so that D increases significantly with increasing pressure due to higher degree of plasticization. For feeds with different fractions of CH_4, because of the reduction in the plasticization, the effect of pressure on D for CO_2 became very weak and the dependency of D on pressure decreases with increasing CH_4 fraction.

For pure CH_4, D is constant and did not change with increasing pressure. By adding 9.7 % CO_2 to the feed, a very weak dependency of D on pressure was observed and this dependency increased with increasing CO_2 fraction due to the increase in the plasticization, so that for feeds with 46.1 % CO_2, D for CH_4 increased significantly. Additionally, at a specific pressure, D for CH_4 decreases with increasing CH_4 fraction. It should be mentioned that although with increasing CH_4 fraction in the feed, the CH_4 sorption increases, the swelling and the plasticization affect decreases due to reduction in CO_2 sorption. The latter reason overcomes the results in the reduction in the diffusivity of CH_4 with increasing CH_4 fraction at a specific pressure.

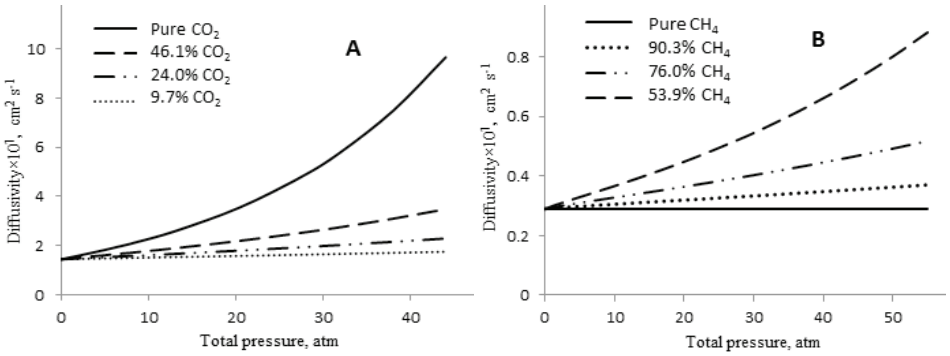

Fig. 8. Diffusivity of: A) CO_2 and B) CH_4 in the pure state and as mixtures in the CA membrane.

CONCLUSIONS

The permeation behavior of mixed gases through glassy membranes was significantly different from pure species, especially in the presence of the plasticizeation phenomenon. The presence of the second component, such as CH_4 or N_2, along with CO_2 in the feed led to a decrease in the CO_2 solubility resulting in a decrease in diffusivity, permeability and the plasticization effect. This research was focused on gas mixtures and a model was developed for the prediction the

permeability of the species in mixed gases through glassy polymers with and without plasticization. Then, by comparing the proposed model for the experimental data of permeation of pure CO_2 and CH_4 through the different glassy polymer membranes, the parameters of the model were calculated. Then, these parameters were used for predicting the permeability of gases in the mixtures. The results showed that the presence of CH_4 in the feed reduces the permeability of CO_2 as well as the plasticization. Moreover, the results show that D for pure CO_2 significantly changes with pressure and with the addition of CH_4 to the feed, this dependency decreased. For a feed with 53.9 % CH_4 (46.1 % CO_2) the D value for CH_4 increased with increasing pressure but for higher fractions of CH_4 in the feed, this dependency almost disappeared.

Acknowledgements. This research was supported by Islamic Azad University, Bushehr Branch.

ИЗВОД

ПРОПУСТЉИВОСТ СМЕШЕ ГАСОВА КРОЗ ПОЛИМЕРЕ У СТАКЛАСТОМ СТАЊУ СА ПЛАСТИФИКАЦИЈОМ И БЕЗ ЊЕ

MASOUD SABERI

Department of Chemical Engineering, Bushehr Branch, Islamic Azad University, Bushehr, Iran

У овом истраживању проучавана је растворљивост, пропустљивост и дифузивност смеша гасова кроз полимере у стакластом стању. Претпоставља се да је дифузивност компонената у мешавини функција концентрације свих компоненти у смеши. Затим се пропустљивост чистих компонената проширује на смеше гасова и за проверу ваљаности се проверава модел фитовањем експерименталних података за пермеабилност CO_2/CH_4 кроз различите мембране у стакластом стању и израчунавају се параметри модела. Након тога, тако добијени параметри се користе за предвиђање пропустљивости CO_2 и CH_4 у смеши. Резултати показују да су растворљивост, дифузивност, а такође и пропустљивост CO_2 кроз полимере у стакластом стању смањени у присуству CH_4 и пластификатора. Штавише, дифузивност за чисти CO_2 значајно зависи од притиска у присуству пластификатора док се с повећањем удела CH_4 та зависност смањује због смањења пластификације.

(Примљено 15. јула, ревидирано 31. јула, прихваћено 5. августа 2020)

REFERENCES

1. T. Visser, N. Masetto, M. Wessling, *J. Memb. Sci.* **306** (2007) 16 (https://doi.org/10.1016/j.memsci.2007.07.048)
2. Y. Liu, R. Wang, T. S. Chung, *J. Memb. Sci.* **189** (2001) 231 (https://doi.org/10.1016/S0376-7388(01)00415-X)
3. S. Kanehashi, T. Nakagawa, K. Nagai, X. Duthie, S. Kentish, G. Stevens, *J. Memb. Sci.* **298** *(*2007) 147 (https://doi.org/10.1016/j.memsci.2007.04.012)
4. C. Ma, W. J. Koros, *J. Memb. Sci.* **428** (2013) 251 (https://doi.org/10.1016/j.memsci.2012.10.024)
5. S. S. Hosseini, J. A. Dehkordi, P. K. Kundu, *Chem. Prod. Proc. Mod.* **11** (2016) 7 (https://doi.org/10.1515/cppm-2015-0051)

6. K. Ghasemzadeh, M. Jafari, A. A. Babalou, *Chem. Prod. Proc. Mod.* **11** (2016) 23 (https://doi.org/10.1515/cppm-2015-0054)
7. G. Kapantaidakis, G. Koops, M. Wessling, S. Kaldis, G. Sakellaropoulos, *AIChE J.* **49** (2003) 1702 (https://doi.org/10.1002/aic.690490710)
8. A. Bos, I. Pünt, H. Strathmann, M. Wessling, *AIChE J.* **47** *(*2001) 1093 (https://doi.org/10.1002/aic.690470515)
9. G. Dong, H. Li, V. Chen, *J. Memb. Sci.* **369** (2011) 206 (https://doi.org/10.1016/j.memsci.2010.11.064)
10. A. Bos, I. Pünt, M. Wessling, H. Strathmann, *Sep. Purif. Technol*. **14** (1998) 27 (https://doi.org/10.1016/S1383-5866(98)00057-4)
11. A. Ismail, W. Lorna, *Sep. Purif. Technol*. **27** *(*2002) 173 (https://doi.org/10.1016/S1383-5866(01)00211-8)
12. A. Bos, I. Pünt, M. Wessling, H. Strathmann, *J. Memb. Sci*. **155** (1999) 67 (https://doi.org/10.1016/S0376-7388(98)00299-3)
13. E. Sada, H. Kumazawa, P. Xu, S. T. Wang, *J. Polym. Sci.* **28** (1990) 113 (https://doi.org/10.1002/polb.1990.090280110)
14. T. Visser, G. Koops, M. Wessling, *J. Memb. Sci*. **252** (2005) 265 (https://doi.org/10.1016/j.memsci.2004.12.015)
15. A. Houde, B. Krishnakumar, S. Charati, S. Stern, *J. Appl. Polym. Sci.* **62** (1996) 2181 (https://doi.org/10.1002/(SICI)1097-4628(19961226)62:13<2181::AID-APP1>3.0.CO;2-F)
16. S. Jordan, W. J. Koros, *J. Polym. Sci.* **28** (1990) 795 (https://doi.org/10.1002/polb.1990.090280602)
17. A. L. Khan, X. Li, I. F. Vankelecom, *J. Memb. Sci.* **372** (2011) 87 (https://doi.org/10.1016/j.memsci.2011.01.056)
18. M. Donohue, B. Minhas, S. Lee, *J. Memb. Sci.* **42** (1989) 197 (https://doi.org/10.1016/S0376-7388(00)82376-5)
19. P. Raymond, W. J. Koros, D. Paul, *J. Memb. Sci.* **77** *(*1993) 49 (https://doi.org/10.1016/0376-7388(93)85234-N)
20. O. Vopička, M. GraziaDe Angelis, G. Cesare Sarti, *J. memb. Sci.* **449** (2002) 97 (https://doi.org/10.1016/j.memsci.2013.06.065)
21. M. Saberi, A. A. Dadkhah, S. A. Hashemifard, *J. Memb. Sci.* **499** (2015) 164 (https://doi.org/10.1016/j.memsci.2015.09.044)
22. M. Saberi, S. A. Hashemifard, A. A. Dadkhah, *RSC Adv.* **6** (2016)16561 (https://doi.org/10.1039/C5RA23506E)
23. W. J. Koros, *J. Polym Sci*. **18** (1980) 981 (https://doi.org/10.1002/pol.1980.180180506)
24. X. Duthie, S. Kentish, C. Powell, K. Nagai, G. Qiao, G. Stevens, *J. Memb. Sci*. **294** (2007) 40 (https://doi.org/10.1016/j.memsci.2007.02.004)
25. C. A. Scholes, G. Q. Chen, G. W. Stevens, S. E. Kentish, *J. Memb. Sci*. 346 (2010) 208. (https://doi.org/10.1016/j.memsci.2009.09.036)
26. S. Stern, V. Saxena, *J. Memb. Sci.* **7** (1980) 47 (https://doi.org/10.1016/S0376-7388(00)83184-1)
27. V. Saxena, S. Stern, *J. Memb. Sci.* **12** (1982) 65 (https://doi.org/10.1016/0376-7388(82)80004-5)
28. E. Toni, M. Minelli, G. C. Sarti, *Fluid Phase Equilib.* **455** (2017) 54 (https://doi.org/10.1016/j.fluid.2017.09.025)
29. T. Barbari, W. J. Koros, D. Paul, *J. Polym. Sci*. **26** (1988) 729 (https://doi.org/10.1002/polb.1988.090260402)

30. T. Barbari, W. J. Koros, D. Paul, *J. Polym. Sci.* **26** (1988) 709 (https://doi.org/10.1002/polb.1988.090260401)
31. T. Barbari, W. J. Koros, D. Paul, *J. Memb. Sci.* **42** (1989) 69 (https://doi.org/10.1016/S0376-7388(00)82366-2).

Journal of the Serbian Chemical Society
JSCS-info@shd.org.rs • www.shd.org.rs/JSCS
J. Serb. Chem. Soc. *86* (4) 355–366 (2021)
JSCS–5426
Original scientific paper

Achillea clypeolata Sibth. & Sm. essential oil composition and QSRR model for predicting retention indices

MILICA AĆIMOVIĆ[1]*, LATO PEZO[2], MIRJANA CVETKOVIĆ[3], JOVANA STANKOVIĆ[3] and IVANA ČABARKAPA[4]

[1]*Institute of Field and Vegetable Crops Novi Sad, Maksima Gorkog 30, 21000 Novi Sad, Serbia,* [2]*University of Belgrade, Institute of General and Physical Chemistry, Studentski trg 10–12, 1000 Belgrade, Serbia,* [3]*University of Belgrade, Institute of Chemistry, Technology and Metallurgy, Njegoševa 12, 11000 Belgrade, Serbia and* [4]*University of Novi Sad, Institute of Food Technology, Bulevar cara Lazara 1, 21000 Novi Sad, Serbia*

(Received 24 May 2020, revised 17 January, accepted 5 February 2021)

Abstract: The aim of this study was the prediction model of retention indices of compounds from the aboveground parts of *Achillea clypeolata* Sibth. & Sm. essential oil, obtained by hydrodistillation and analysed by GC–MS. The quantitative structure–retention relationship analysis was applied in order to anticipate the retention time of the obtained compounds. The selection of the seven molecular descriptors was done by a genetic algorithm. The chosen descriptors were uncorrelated and were used to construct an artificial neural network. A total of 40 experimentally obtained retention indices was used to build this prediction model. The coefficient of determination for the training, testing and validation cycles were: 0.950, 0.825 and 1.000, respectively, indicating that this model could be used for prediction of retention indices for *A. clypeolata*, essential oil compounds.

Keywords: hydrodistillation; GC–MS; artificial neural networks.

INTRODUCTION

Achillea clypeolata Sibth. & Sm., yellow or moonshine yarrow, is a Balkan endemic species, spread across North and Central Greece, South Albania, North Macedonia, East Serbia, Bulgaria, Southeast Romania, West and European Turkey according to a study by Nedelcheva.[1] It is dominantly diploid ($2n$ = 18), a perennial species, shortly tomentose, silver–grey. Erect stem, simple and up to 60 cm long. The rhizome is well developed and woody. Leaves are pinnatisec, plane, and weakly glandular–punctate. Basal leaves are 8–20 cm long and 2–4.5 cm wide, petiolate, the lobes ovate, serrate to pinnatifid, with acute teeth. Cauline leaves all more or less distant, about twice as long as the internodes, while the

* Corresponding author. E-mail: acimovicbabicmilica@gmail.com
https://doi.org/10.2298/JSC200524008A

upper leaves are 1–2 cm, sessile. Corymbs with many capitulars, peduncles, 2 mm tomentose. Involucres 3–4 mm in diameter, bracts elliptical or lanceolate, 1.5 mm. Ligules 1 mm yellow. Peripheral flowers with rounded ligules 5-fold shorter than involucres. It blooms from June to July. Pollination is entomophylous and anemophylous, with dispersal of fruits and seeds in its habitats. However, in nature it hybridizes with *A. neilreichii*, *A. setacea* and *A. panonica*. This plant is heliophytic, termophyte that occupies dry, neutral soils in arid meadows. Nowadays, it spontaneously grows only on limestone in Serbia, and it is listed as a critically endangered species. According to Contreras–Medina and Luna–Vega,[2] the plant is economically important, as a decorative plant, and has been identified as important to the plant genetic fund.

A. clypeolata tastes bitter like mugwort. This species is rich in sesquiterpenes, diterpenes and phenolic compounds, as well as flavonoids.[3–6] Furthermore, the content of essential oil is low (0.05–0.1 %), and according to the essential oil composition, there are two chemotypes.[7] According to a study by Simić *et al.*,[8] one chemotype contains *E*-γ-bisabolene, 1,8-cineole, borneol and caryophyllene oxide. The other one contains 1,8-cineole and camphor as the dominant compounds as documented in thestudy by Chalcat *et al.*[9]

However, this plant is not investigated thoroughly, only its antioxidant and antimicrobial properties have been confirmed to the present day. Antioxidant activity of *A. clypeolata* leaf, flower, and root methanolic extract is determined by total reducing power assay and DPPH. It was reported that total reducing power ranged between 10.66 mg AAE/ml for root extract, to 11.90 mg AAE/ml for flower extract. *In vitro* DPPH tests showed similar antioxidant activities, and according to these results *A. clypeolata* can be used as a potential natural antioxidant source.[6] Investigations by Simić *et al.*[8] showed that *A. clypeolata* essential oil express antimicrobial activity against *Escherichia coli*, *Klebsiella pneumoniae*, *Pseudomonas aeruginosa* and *Staphylococcus aureus*. However, its wide application is recorded in traditional medicine of Bulgaria and Serbia. In her study, Nedelcheva,[1] stated that, in Bulgaria, it is used to treat: hemorrhoids, wounds, bleeding, gastro-intestinal atony, bed wetting, kidney inflammation, amenorrhoea, inflamed gums and liver diseases. However, Zlatković *et al.*[10] concluded that in Serbian traditional medicine it is mainly used as an antidiabetic drug.

In the study by Wolfender *et al.*,[11] quantitative structure retention relationship (QSRR) provides insight in relation between the chemical structure and the physicochemical or biological properties. A systematic study was presented in the paper by Héberger,[12] where the QSRR analysis in gas chromatography (GC) was presented for planar chromatography, column liquid and micellar liquid chromatography and affinity chromatography. Lately, numerous publications have been related to the QSRR analysis.[13,14] The chemical compound structure is explored by their mathematical models, presented by so–called molecular des-

criptors, which transfer the compound data through the symbolic representation of a molecule into a numerical value as reported by Khezeli *et al.*[15] Marrero-Ponce *et al.*[16] determined that the molecular descriptors should be chosen to avoid overfitting, in order to obtain statistically significant results, and to establish clear relationships between molecular structure and its descriptors. In a study by Micić *et al.*,[17] it was shown that GC–MS is a unique technique that yields a large number of the quantitatively comparable, reproducible data and exact retention time for large sets of compounds.

In a study by Tropsha and Golbraikh,[18] the numerical model that represents the relation between the molecular descriptors and the retention time can be established by numerous machine learning algorithms, or by using the artificial neural network (ANN), which is used in this study, and has already been proven to be an excellent tool according to the literature.[11,19]

The aim of this paper was to establish a new QSRR model for predicting the retention times of chemical compounds in *A. clypeolata* essential oil obtained by hydrodistillation and analyzed by GC–MS using the genetic algorithm (GA) variable selection method and the artificial neural network (ANN) model.

MATERIAL AND METHODS

Plant material

A. clypeolata was collected on 7th July 2018, on Mt. Rtanj. The plant species were in full flowering stage by this date. The plant aboveground parts were cut manually at the upper 15 cm of the plant, and the biomass was placed in an air-dryer until constant weight at 35 °C to avoid essential oil losses. Voucher specimens were confirmed and deposited at the Herbarium BUNS, the University of Novi Sad, Faculty of Sciences, Department of Biology and Ecology, under the acquisition number 2-1448.

Essential oil extraction

Air-dried aerial parts of *A. clypeolata* were submitted to hydrodistillation (Clevenger apparatus, 3 h). Then, the essential oil was dried over anhydrous sodium sulfate and stored in a dark glass vial at 4 °C for further analysis. Dried aerial parts of *A. clypeolata* were found to contain 0.04 % of pale–yellow oil.

Essential oil analysis

The essential oil was analyzed using an HP 5890 gas chromatograph coupled to an HP 5973 MSD and fitted with a capillary column HP–5MS (30 m×0.25 mm×0.25 μm film thickness). Analytical conditions were as follows: helium was used as carrier gas; inlet pressure was 25 kPa; linear velocity: 1 ml/min at 210 °C; injector temperature: 250 °C; injection mode: splitless. MS scan conditions were: source temperature, 200 °C; interface temperature, 250 °C; electron energy, 70 eV; mass scan range, 40–350 amu. Temperature program: 60 to 285 °C at a rate of 4.3 °C/min. The components were identified based on their linear retention index relative to C8–C32 *n*-alkanes, comparison with data reported in the literature (Wiley and NIST databases). Percentage (relative) of the identified compounds was computed from GC peak area.

QSRR analysis

The molecular structure dataset was presented in the form of .smi files (simplified molecular input line entry specification) which were used in the molecular descriptors calculation. The .smi files were collected from Pub Chem. The similar approach was noticed in a paper by Matyushin *et al.*,[20] where .smi notation of the molecule structure was used as an input for the model. In that study, a neural network was used for the estimation of gas chromatographic retention indices on non-polar stationary phases. In the study by Dong *et al.*,[21] the calculation of the specified molecular descriptors for each chemical compound was performed using molecular descriptor software PaDel as in the study by Yap.[22] After the calculation was completed, the data were randomly separated and independently chosen into training, testing and validation sets (60, 20 and 20 % of data, respectively), in order to determine the predictive artificial neural network model (ANN). A series of 100,000 randomly generated ANN topologies were tested, changing the number of hidden neurons (from 1 to 20) and initial values of weights and biases the training process. The optimization process was performed based on validation error minimization. ANN was developed to form a reliable model to predict the retention times from PaDel-calculated descriptors. The evaluation of the performances of the developed model was done by comparing the predicted and experimentally obtained retention times of the observed chemical compounds used for the model construction. The model overfitting was also checked. All calculations were performed by an eight-core personal computer and the PaDel database was used to calculate the molecular descriptors (which included 1D, 2D and 3D descriptors, Micić *et al.*[17]). The genetic algorithm (GA) must be applied in order to reduce the number of parameters (calculated by PaDel). This task was performed, using Heuristic Lab, to select the most relevant molecular descriptors for *RT* prediction. GA is a stochastic optimization method inspired by evolution theory.[23,24] The correlation between the descriptors was examined and collinear descriptors were detected using factor analysis. Statistical investigation of the data has been performed mainly by the Statistica 10 software.[25]

Artificial neural network (ANN)

A multi-layer perceptron model (MLP) covered input, hidden and output layer was used, considering that it is proven to be quite capable of approximating nonlinear functions.[26] Broyden–Fletcher–Goldfarb–Shanno (BFGS) algorithm was used for ANN modelling. ANN results, including the weight values, depend on the initial assumptions of parameters necessary for ANN construction and fitting.[27,28] A series of various topologies were used, in which the number of hidden neurons varied from 10 to 20 and the training process of each network was run 100,000 times with random initial values of weights and biases. The optimization process was performed on the basis of validation error minimization. ANN calculations were performed with Statistica 10. Yoon's interpretation method was used to determine the relative influence of molecular descriptors on retention time.[29] This method was applied based on the weight coefficients of the developed ANN.

RESULTS AND DISCUSSION

Chemical profile of A. clypeolata essential oil

In the *A. clypeolata* essential oil 40 compounds were detected, that represented 99.3 % of total oil composition (Table I). Among them 3 not identified compounds (NI) compromised 1.0 %. As it can be seen, the most abundant compounds in *A. clypeolata* essential oil were 1,8-cineole (45.1 %) and camphor (18.2 %). Sixteen compounds had average relative abundance over 1.0 %. Mono-

terpene hydrocarbons (55.7 %) and their oxygenated derivatives (29.5 %) were dominant in the chemical composition.

TABLE I. Quantitative profile of *A. clypeolata* essential oil

No.	Compound	Formula	*RI*[a], min	*RI*[b], min	Content, %
1	Tricyclene	$C_{10}H_{16}$	927	921	0.1
2	*α*-Thujene	$C_{10}H_{16}$	929	928	0.1
3	*α*-Pinene	$C_{10}H_{16}$	936	932	1.1
4	Camphene	$C_{10}H_{16}$	950	946	2.3
5	Thuja-2,4(10)-diene	$C_{10}H_{14}$	955	953	0.1
6	Sabinene	$C_{10}H_{16}$	975	969	0.3
7	*β*-Pinene	$C_{10}H_{16}$	979	974	1.4
8	dehydro-1,8-Cineole	$C_{10}H_{16}O$	993	988	0.1
9	*α*-Terpinene	$C_{10}H_{16}$	1016	1014	0.6
10	*p*-Cymene	$C_{10}H_{14}$	1022	1020	3.1
11	1,8-Cineole	$C_{10}H_{18}O$	1028	1026	45.1
12	*γ*-Terpinene	$C_{10}H_{16}$	1053	1054	1.2
13	*p*-Mentha-2,4(8)-diene	$C_{10}H_{16}$	1081	1083	0.2
14	Linalool	$C_{10}H_{18}O$	1092	1095	0.4
15	*Z*-*p*-Menth-2-en-1-ol	$C_{10}H_{18}O$	1114	1118	0.2
16	*α*-Campholenal	$C_{10}H_{16}O$	1119	1122	0.2
17	Camphor	$C_{10}H_{16}O$	1136	1141	18.2
18	*Z*-Chrysanthenol	$C_{10}H_{16}O$	1156	1160	0.3
19	Borneol	$C_{10}H_{18}O$	1159	1165	2.7
20	*δ*-Terpineol	$C_{10}H_{18}O$	1161	1162	0.6
21	Terpinen-4-ol	$C_{10}H_{18}O$	1172	1176	2.8
22	*α*-Terpineol	$C_{10}H_{18}O$	1186	1190	2.4
23	Myrtenal	$C_{10}H_{14}O$	1192	1195	0.3
24	Thymol	$C_{10}H_{14}O$	1290	1289	0.9
25	Carvacrol	$C_{10}H_{14}O$	1300	1298	0.5
26	*E*-Caryophyllene	$C_{15}H_{24}$	1417	1408	0.5
27	*allo*-Aromadendrene	$C_{15}H_{24}$	1458	1458	1.3
28	Germacrene D	$C_{15}H_{24}$	1479	1484	1.2
29	NI[c]-1		1484	–	0.2
30	*γ*-Cadinene	$C_{15}H_{24}$	1512	1513	1.2
31	*δ*-Cadinene	$C_{15}H_{24}$	1521	1522	0.2
32	NI[c]-2		1571	–	0.4
33	Spathulenol	$C_{15}H_{24}O$	1573	1577	0.4
34	Caryophyllene oxide	$C_{15}H_{24}O$	1578	1582	3.2
35	*β*-Oplopenone	$C_{15}H_{24}O$	1603	1607	0.2
36	Muurola-4,10(14)-dien-1-*β*-ol	$C_{15}H_{24}O$	1622	1630	0.3
37	Caryophylla-4(12),8(13)-dien-5-*α*-ol	$C_{15}H_{24}O$	1630	1627	0.7
38	*epi*-*α*-Cadinol	$C_{15}H_{26}O$	1635	1638	2.4
39	*α*-Cadinol	$C_{15}H_{26}O$	1648	1652	1.5
40	NI[c]-3		1680	-	0.4
Monoterpene hydrocarbons					55.7
Oxygenated monoterpenes					29.5
Sesquiterpene hydrocarbons					4.4

TABLE I. Continued

Compound	Formula	RI^a, min	RI^b, min	Content, %
Oxygenated sesquiterpenes				8.7
NI[c]				1.0
Total identified				99.3

[a]Retention index experimental; [b]retention index from the NIST web book database; [c]not identified compound with mass spectrum –*m*/*z* (intensity): **NI–1**: 41.05 (17.0), 43.00 (9.0), 57.00 (100.0), 80.95 (10.0), 85.00 (50.0), 91.00 (9.0), 118.95 (35.0), 121.10 (8.0), 133.85 (11.0), 236.15 (12.0); **NI–2**: 41.05 (33.0), 57.00 (69.0), 66.95 (29.0), 69.05 (38.0), 79.05 (41.0), 91.00 (42.0), 105.00 (28.0), 134.00 (46.0), 135.00 (100.0), 150.00 (44.0); **NI–3**: 41.05 (34.0), 66.95 (40.0), 79.00 (72.0), 81.00 (45.0), 90.95 (80.0), 93.00 (42.0), 104.95 (49.0), 107.00 (48.0), 109.00 (100.0), 159.05 (61.0)

The prevailing compounds in the oils of *A. clypeolata* from Mt. Rtanj (43°46′34″ N, 21°53′36″ E), collected during July 1996, were 1,8-cineole (38.6 %) and camphor (19.9 %) in the study by Chalcat *et al.*[9]

It can be concluded that this slight variation in the chemical composition could be caused by the climate conditions during the year, collection time and exposition. Furthermore, aerial parts of *A. clypeolata* from the Mt. Rudina (43°41′35″ N, 21°55′18″ E) had significantly different composition: *E*-γ-bisabolene (17.9 %), 1,8-cineole (16.0 %), borneol (11.9 %) and caryophyllene oxide (11.5 %) as reported by Simić *et al.*[8] However, this diversity could be a phenomenon of endemism within genus according to Radulović *et al.*[30]

QSRR model validation

Prior to the GA calculation, the factor analysis was performed in order to eliminate the descriptors with equal or almost equal values for the examined molecules. Only one of the inter–correlated descriptors remained in the GA calculation. As a result of this preliminary consideration, about 400 descriptors remained for GA calculation. GA was used to select the most appropriate molecular descriptors for *RI* prediction, and the selection of the most relevant descriptors was done using the evolution simulation.[31,32] The number of elements on each chromosome (*i.e.*, observed compounds) was equal to the number of the molecular descriptors obtained in the PaDel base. The number of the elements was kept relatively low to maintain a small subset of descriptors according to a study by Todeschini and Consonni.[33] As a result, the probability of generating zero for an element was set at least 60 % greater than the probability of generating the value of one. The operators used were crossover and mutation. The probability of application of these operators was varied linearly with generation renewal (0.5 % for mutation and 90 % for crossover). A population size of 100 individuals was chosen for GA, and evolution was allowed for over 50 generations. The predicted retention indices and molecular descriptors were presented in Fig. 1 and also in Ttable S-I of the Supplementary material to this paper, confirming the adequate

prediction capabilities of the constructed ANN, by showing the relationship between the predicted and experimental retention values.

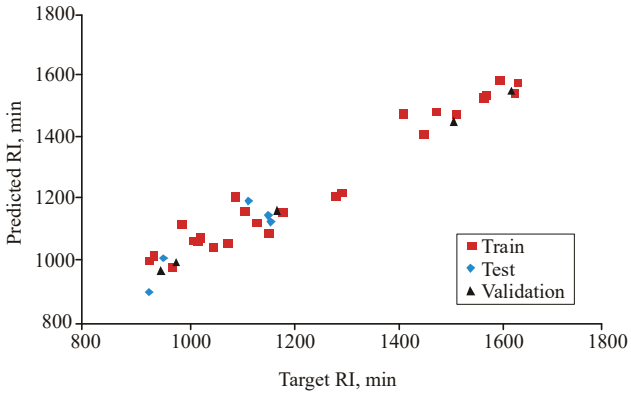

Fig. 1. Comparison of experimentally obtained *RI*s with ANN predicted values.

The principal component analyses (Fig. S-1 of the Supplementary material) showed the groups of chemical compounds in the first factor plane. These groups were mostly different according to molecular descriptors: VP-0, IC0 and ETA Epsilon 3.

The evolution of the generations was stopped when 90 % of the generations took the same fitness.

The ANN results, including the weight coefficients, depend on the initial presumptions of parameters which are vital for ANN development and fitting. Likewise, the number of neurons in the hidden layer can alter the result of the ANN model.

As a result, the seven most significant molecular descriptors selected by GA were: 2D autocorrelation descriptors (AATS0v – average Broto–Moreau autocorrelation – lag 0 / weighted by van der Waals volumes, and AATSC4c – average centered Broto–Moreau autocorrelation – lag 4 / weighted by charges)[33], 2D Barysz matrix descriptor (VR2 Dzi – normalized Randic–like eigenvector-based index from Barysz matrix / weighted by first ionization potential);[32] Chi path descriptors (VP-0 – valence path, order 0;[34] extended topochemical atom descriptor (ETA Epsilon 3, which shows a measure of electronegative atom count);[34] information content descriptors (IC0 – information content index (neighborhood symmetry of 0-order and BIC2 – bond information content index (neighborhood symmetry of 2-order).[33]

These descriptors encode different aspects of the molecular structure and were applied to develop a QSRR model. Table II represents the correlation matrix among these descriptors (none of the correlations were statistically significant).

TABLE II. The correlation coefficient matrix for the selected descriptors by GA

	AATSC4c	VR2Dzi	VP-0	ETAEpsilon3	IC0	BIC2
AATS0v	0.059	–0.015	–0.149	0.124	–0.034	0.143
AATSC4c		0.209	0.151	0.059	0.046	0.175
VR2Dzi			0.166	0.200	–0.131	0.177
VP-0				0.151	–0.012	0.151
ETAEpsilon3					–0.232	–0.297
IC0						0.022

The calibration and predictive capability of a QSRR model should be tested through model validation. The most widely used squared correlation coefficient (r^2) can provide a reliable indication of the fitness of the model, thus, it was employed to validate the calibration capability of a QSRR model.

Artificial neural network (ANN)

In order to explore the nonlinear relationship between *RI*s and the selected descriptors, ANN technique was used to build models. The ability to generalize the model was evaluated by an external test set. The statistical results of the MLP 7-8-1 network is shown in Table III.

TABLE III. ANN model summary (performance and errors), for training, testing and validation cycles; performance term represent the coefficients of determination, while error terms indicate a lack of data for the ANN model

Net. name	Performance			Error			Train. algor.	Error funct.	Hidden activat.	Output activat.
	Train.	Test.	Valid.	Train.	Test.	Valid.				
MLP 7-8-1	0.950	0.825	1.000	1656.639	1236.916	531.5842	BFGS 8	SOS	Exponential	Tanh

The predicted *RI*s presented in Table S-I confirm the good quality of the constructed ANN, by showing the relationship between the predicted and experimental retention values. The obtained results reveal the reliability of the ANN models for predicting the *RI*s of compounds in *A. clypeolata* essential oil determined by GC–MS. There are two groups of compounds according to the carbon chain length, first monoterpenes (C_{10}) and the second group sesquiterpenes (C_{15}). The two compounds (*cis* and *trans* isomers) are allocated from other monoterpenes. The retention indices of monoterpene compounds were in the range of 927 and 1300, while in the case of sesquiterpenes indices ranged between 1417 and 1648. Furthermore, thymol and carvacrol are the structures containing both a phenyl and a hydroxy group, suggesting both benzene and 1-butanol as model compounds according to a study by Roon *et al.*[36]

Molecular descriptors

Separation of compounds in GC and their retention indices are linked to affinity towards mobile and stationary phases. Affinity and solubility of the separ-

ated molecules directly depend on their chemical structure and physicochemical properties, which could be expressed by molecular descriptors. We have utilized seven molecular descriptors for predictions of RI in the obtained ANN model.

2D average Moreau–Broto are spatial autocorrelation descriptors,[37] and could be weighted with charges (AATSC4c) or by van der Waals volumes (AATS0v). According to Hollas,[38] these descriptors explain the molecular structure and physicochemical features of atoms. 2D autocorrelation descriptors are obtained by interatomic distances obtained within the geometry matrix which is determined by the set of atomic characteristics.[33] García-Domenech *et al.*[39] determined that Chi path descriptors belong to the group of connectivity indices which show the numerical possibilities of two identical molecules encountering each other and are obtained from the bond accessibilities. The Chi path index descriptor, used in this work, was the average simple path order 1 (VP–0). 2D Barysz distance matrix is a weighted distance matrix accounting simultaneously for the presence of heteroatoms and multiple bonds in the molecule, and VR2 Dzi was used in the study by Todeschini and Consonni.[33] Information content descriptors were calculated as information content of molecules, based on the calculation of equivalence classes from the molecular graph. The indices of neighbourhood symmetry also take into account neighbour degree and edge multiplicity. The used Information content descriptors were IC0 and BIC2. Extended topochemical atom descriptor ETA Epsilon 3 was used in research by Roy and Ghosh,[35] as a measure of electronegative atom count. The influence of seven most important input variables, identified using genetic algorithm on *RI* was studied in this section. VP0 was the most influential parameter with approximately relative importance of 72.1 %, while the influence of IC0 and AATS0v were 6.6 and 5.1%, respectively. ETA Epsilon 3 and VR2 Dzi were influential at levels 4.9 and 3.9 %, respectively. The influence of BIC2 and AATSC4c were 3.8 and 3.7 %.

CONCLUSION

A. clypeolata essential oil obtained by hydrodistillation was analyzed by GC–MS. Analysis showed that the most abundant compounds were *p*-cymene (24.4 %), limonene (13.5 %) and linalool (8.3 %). The QSRR model for estimating retention times of essential oil compounds was developed for a series of 40 compounds employing the ANN modelling approach. The results demonstrated that the ANN model was adequate in predicting retention times of the *A. clypeolata* essential oil compounds. A suitable model with high statistical quality and low prediction errors was derived. The following seven molecular descriptors were suggested by genetic algorithm: two 2D average Moreau–Broto descriptors (AATSC4c and AATS0v), Chi path descriptor VP-0, 2D Barysz distance matrix

descriptor VR2 Dzi, two Information content descriptors (IC0 and BIC2), and Extended topochemical atom descriptor ETA Epsilon 3.

Selected molecular descriptors were not auto correlated which was suggested by correlation coefficient matrix; thus, descriptors were suitable for QSRR analysis.

The results demonstrated that the ANN model was adequate in predicting the RIs of the compounds in *A. clypeolata* essential oil obtained by hydrodistillation and analyzed by GC–MS. The coefficient of determination for training cycle was 0.950, which is a good indication that this model could be used as a fast mathematical tool for prediction of retention time values for compounds in *A. clypeolata* essential oil obtained by GC–MS analysis due to low prediction error and moderately high r^2.The suitable model with high statistical quality and low prediction errors was derived, and it could be further used for estimation RI of newly detected compounds.

Acknowledgments. The Authors gratefully acknowledge Adonis Sokobanja Ltd. for their administrative and technical support. We would especially like to thank Nebojša Stanojević for his help during collection of *A. clypeolata at* Mt. Rtanj. The Authors are grateful to Milica Rat, PhD, Research Associate and Curator Assistant in Herbarium BUNS, Novi Sad, Serbia, for identifying and archiving this plant species.

SUPPLEMENTARY MATERIAL

Predicted retention indices and molecular descriptors of essential oil compounds in *A. clypeolata* obtained by hydrodistillation and PCA ordination of molecular descriptors are available electronically from the Journal web site, http://www.shd.org.rs/JSCS/, or from the corresponding author on request.

И З В О Д

ХЕМИЈСКИ САСТАВ ЕТАРСКОГ УЉА *Achillea clypeolata* Sibth. & Sm. И QSRR МОДЕЛ ЗА ПРЕДВИЂАЊЕ РЕТЕНЦИОНОГ ВРЕМЕНА

МИЛИЦА АЋИМОВИЋ[1], ЛАТО ПЕЗО[2], МИРЈАНА ЦВЕТКОВИЋ[3], ЈОВАНА СТАНКОВИЋ[3] и ИВАНА ЧАБАРКАПА[4]

[1]Институт за ратарство и повртарство Нови Сад, Максима Горког 30, 21000 Нови Сад, [2]Универзитет у Београду, Институт за општу и физичку хемију, Студентски трг 10–12, 1000 Београд, [3]Универзитет у Београду, Институт за хемију, технологију и металургију, Његошева 12, 11000 Београд и [4]Универзитет у Новом Саду, Институт за храну Технологија, Булевар цара Лазара 1, 21000 Нови Сад

Циљ ове студије био је израда модела за предвиђања ретенционог времена хемијских једињења из есенцијалног уља надземних делова биљке *Achillea clypeolata* Sibth. & Sm., добијеног хидродистилацијом и анализираног GC–MS техником. Квантитативна анализа хемијске структуре и предвиђања ретенционог времена (quantitative structure––retention relationship – QSRR) је примењена да би се предвидело време задржавања хемијских једињења добијених коришћењем GC–MS анализе. Избор седам молекулских дескриптора извршен је коришћењем факторске анализе и генетског алгоритма. Примећено је да изабрани дескриптори нису били у међусобној корелацији, па су коришћени као улазни подаци при изградњи вештачке неуронске мреже. У изградњи модела предвиђања ретенционих времена коришћено је укупно 40 експериментално добијених ретенционих времена. Коефицијент детерминације током циклуса припреме, тестирања и

валидације достигао је вредности 0,950; 0,825 и 1,000, редом, што указује на то да се овај модел може користити за предвиђање ретенционих времена хемијских једињења добијених из есенцијалног уља *A. clypeolata*.

(Примљено 24. маја 2020, ревидирано 17. јануара, прихваћено 5. фебруара 2021)

REFERENCES

1. A. Nedelcheva, *J. Appl. Pharm. Sci.* **2** (2012) 165 (https://doi.org/10.7324/JAPS.2012.2828)
2. R. Contreras-Medina, I. Luna-Vega, in *Global Advances in Biogeography*, L. Stevens, Ed., InTech, Rijeka, 2012, pp. 61–70 (https://doi.org/10.5772/34315)
3. I. Aljančić, S. Macura, N. Juranić, S. Anđelković, N. Ranđelović, S. Milosavljević, *Phytochemistry* **43** (1996) 169 (https://doi.org/10.1016/0031-9422(96)00271-3)
4. M. Todorova, M. Krasteva, M. Markova, E. Tsankova, R. Taskova, D. Peev, *Phytochemistry* **49** (1998) 2371 (https://doi.org/10.1016/S0031-9422(98)00201-5)
5. I. Werner, P. Mucaji, A. Presser, S. Glasl, *Z. Naturforsch*. **62** (2007) 267 (https://doi.org/10.1002/chin.200725175)
6. J. Cvetkovic, M. Dimitrijevic, M. Ilic, S. Simonovic, V. Stankov-Jovanovic, V. Mitic, G. Stojanovic, in *Proceedings of Congress of Chemists and Chemical Engineers of Bosnia and Herzegovina with international participation* (2014), Sarajevo, Bosnia and Hercegovina, *Bulletin of the Chemists and Technologists of Bosnia and Herzegovina*, 2014, p. 99
7. M. Aćimović, M. Zorić, V. D. Zheljazkov, L. Pezo, I. Čabarkapa, J. Stanković Jeremić, M. Cvetković, *Molecules* **25** (2020) 5482 (https://doi.org/10.3390/molecules25225482)
8. N. Simić, R. Palić, V. Ranđelović, *Flavour Fragr. J*. **20** (2005) 127 (https://doi.org/10.1002/ffj.1391)
9. J. C. Chalcat, S. D. Petrovic, Z. A. Maksimović, M. S. Gorunović, *J. Essent. Oil Res.* **15** (2005) 549 (https://doi.org/10.1080/10412905.2005.9698991)
10. B. Zlatković, S. Bogosavljević, A. Radivojević, M. Pavlović,. *J. Ethnopharmacol*. **151** (2014) 704 (https://doi.org/10.1016/j.jep.2013.11.037)
11. J. L. Wolfender, G. Martia, A. Thomas, S. Bertranda, *J. Chromatogr., A* **1382** (2015) 136 (https://doi.org/10.1016/j.chroma.2014.10.091)
12. K. Héberger, *J. Chromatogr., A* **1158** (2007) 273 (https://doi.org/10.1016/j.chroma.2007.03.108)
13. R. Kaliszan, *Chem. Rev.* **107** (2007) 3212 (https://doi.org/10.1021/cr068412z)
14. L. Wu, P. Gong, Y. Wu, K. Liao, H. Shen, Q. Qi, H. Liu, G. Wang, H. Hao, *J. Chromatogr., A* **1303** (2013) 39 (https://doi.org/10.1016/j.chroma.2013.06.041)
15. T. Khezeli, A. Daneshfar, R. Sahraei, *Talanta* **150** (2016) 577 (https://doi.org/10.1016/j.talanta.2015.12.077)
16. Y. Marrero-Ponce, S. J. Barigye, M. E. Jorge-Rodriguez, T. Tran-Thi-Thu, *Chem. Pap*. **72** (2017) 57 (https://doi.org/10.1007/s11696-017-0257-x)
17. D. Micić, S. Ostojić, L. Pezo, S. Blagojević, B. Pavlić, Z. Zeković, S. Đurović, *Ind. Crops Prod.* **138** (2019) (https://doi.org/10.1016/j.indcrop.2019.06.001)
18. A. Tropsha, A. Golbraikh, *Curr. Pharm. Des.* **13** (2007) 3494 (https://doi.org/10.2174/138161207782794257)
19. B. Zisi, I. Sampsonidis, S. Fasoula, K. Papachristos, M. Witting, H.G. Gika, P. Nikitas, A. Pappa-Louisi *Metabolites* **7** (2017) 7 (https://doi.org/10.3390/metabo7010007)
20. D. D. Matyushin, A. Y.Sholokhova, A. K. Buryak, *J. Chromatogr., A* **1607** (2019) 460395 (https://doi.org/10.1016/j.chroma.2019.460395)

21. J. Dong, D. S. Cao, H. Y. Miao, S. Liu, B. C. Deng, Y. H. Yun, N. N. Wang, A. P. Lu, W. B. Zeng, A. F. Chen, *J. Cheminformatics* **7** (2015) 60 (https://doi.org/10.1186/s13321-015-0109-z)
22. C. W. Yap, *J. Comput. Chem*. **32**,(2011) 1446 (https://doi.org/10.1002/jcc.21707)
23. D. E. Goldberg, *Genetic algorithms in search, optimisation and machine learning*, Addison-Wesley, Longman, Boston, MA, 1989 (ISBN:0201157675) (https://doi.org/10.5860/choice.27-0936)
24. A. Tropsha, *Mol. Inform.* **29** (2010) 476 (https://doi.org/10.1002/minf.201000061)
25. Statistica 10 software (StatSoft, Inc. Statistica, ver. 10, data analysis software system) (http://www.statsoft.com/, last accessed 10 January 2019)
26. R. Aalizadeh, N. S. Thomaidis, A. A. Bletsou, P. Gago-Ferrero, *J. Chem. Inf. Model.* **56** (2016) 1384 (https://doi.org/10.1021/acs.jcim.5b00752)
27. Q. Xu, C. Wei, R. Liu, S. Gu, J. Xu, *Chemom. Intell. Lab. Syst.* **146** (2015) 313 (https://doi.org/10.1016/j.chemolab.2015.06.001)
28. P. Kojic, R. Omorjan, *Chem. Eng. Res. Des.* **125** (2018) 398 (https://doi.org/10.1016/j.cherd.2017.07.029)
29. Y. Yoon, G. Swales, T. M. Margavio, *J. Oper. Res. Soc.* **44** (1993) 51 (https://doi.org/10.1057/jors.1993.6)
30. N. Radulović, B. Zlatković, R. Palić, G. Stojanović, *Nat. Prod. Comm.* **2** (2007) 453 (https://journals.sagepub.com/doi/pdf/10.1177/1934578X0700200417)
31. M. Mohammadhosseini, *Anal. Chem. Lett.* **3** (2013) 226 (https://doi.org/10.1080/22297928.2013.861164)
32. M. Nekoei, M. Mohammadhosseini, E. Pourbasheer, *Med. Chem. Res.* **24** (2015) 3037 (https://doi.org/10.1007/s00044-015-1354-4)
33. R. Todeschini, V. Consonni, *Molecular descriptors for chemoinformatics*, Wiley-VCH Verlag GmbH & Co. KGaA, Weinheim, 2009, p. 27 (ISBN: 978-3-527-31852-0)
34. L. B. Kier, L. H. Hall, *Molecular connectivity in chemistry and drug research*, Academic Press, New York, 1976, p. 1214 (https://doi.org/10.1002/jps.2600660852)
35. K. Roy, G. Ghosh, *J. Chem. Inf. Comput. Sci.* **44** (2004) 559-567. (https://doi.org/10.1021/ci0342066)
36. A. Roon, J.R. Parsons, H. A. J. Govers, *J. Chromatogr., A* **955** (2002) 105 (https://doi.org/10.1016/S0021-9673(02)00200-5)
37. M. T. Scotti, M. B. Fernandes, M. J. P. Ferreira, V. P. Emerenciano, *Bioorgan. Med. Chem*. **15** (2007) 2927 (https://doi.org/10.1016/j.bmc.2007.02.005)
38. B. Hollas, *MATCH* **45** (2002) 27 (http://match.pmf.kg.ac.rs/electronic_versions/Match45/match45_27-33.pdf)
39. R. García-Domenech, J. GálvezJesus, J.V. de Julián-Ortiz, L. Pogliani, *Chem. Rev*. **108** (2008) 1127 (https://doi.org/10.1021/cr0780006).

Journal of the Serbian Chemical Society
JSCS-info@shd.org.rs • www.shd.org.rs/JSCS
J. Serb. Chem. Soc. 86 (4) S87–S88 (2021) *Supplementary material*

SUPPLEMENTARY MATERIAL TO

Achillea clypeolata Sibth. & Sm. essential oil composition and QSRR model for predicting retention indices

MILICA AĆIMOVIĆ[1]*, LATO PEZO[2], MIRJANA CVETKOVIĆ[3], JOVANA STANKOVIĆ[3] and IVANA ČABARKAPA[4]

[1]Institute of Field and Vegetable Crops Novi Sad, Maksima Gorkog 30, 21000 Novi Sad, Serbia, [2]University of Belgrade, Institute of General and Physical Chemistry, Studentski trg 10–12, 1000 Belgrade, Serbia, [3]University of Belgrade, Institute of Chemistry, Technology and Metallurgy, Njegoševa 12, 11000 Belgrade, Serbia and [4]University of Novi Sad, Institute of Food Technology, Bulevar cara Lazara 1, 21000 Novi Sad, Serbia

J. Serb. Chem. Soc. 86 (4) (2021) 355–366

Table S-I. Predicted retention indices and molecular descriptors of essential oil compounds in *A. clypeolata* obtained by hydrodistillation

No	$Ri_{pred.}$	AATS0v	AATSC4c $\times 10^{-4}$	VR2 Dzi	VP-0	ETA Epsilon 3	IC0	BIC2
1	902.5058	182.020	-5.8	8.005	7.146	0.454	0.961	0.577
2	974.3304	182.020	-1.3	10.363	7.146	0.443	0.961	0.768
3	985.0507	182.020	-1.6	14.594	7.146	0.443	0.961	0.768
4	1001.993	182.020	-6.4	5.539	6.983	0.443	0.961	0.698
5	1006.013	194.598	-3.7	8.125	6.724	0.443	0.980	0.776
6	1015.869	182.020	-2.5	9.047	6.983	0.443	0.961	0.742
7	1017.944	182.020	-2.0	15.842	6.983	0.443	0.961	0.742
8	1047.053	183.293	-2.5	5.604	7.555	0.442	1.154	0.670
9	1062.964	182.020	-2.2	13.626	7.146	0.433	0.961	0.688
10	1068.251	194.598	-4.0	6.353	6.887	0.433	0.980	0.629
11	1071.717	172.795	-1.7	6.508	7.814	0.442	1.124	0.545
12	1077.483	182.020	-2.2	5.817	7.146	0.433	0.961	0.688
13	1097.757	182.020	-3.0	7.158	7.146	0.433	0.961	0.768
14	1123.312	172.795	-2.5	4.167	7.723	0.426	1.124	0.777
15	1132.768	172.795	-4.5	9.049	7.671	0.433	1.124	0.705
16	1135.335	183.293	-8.1	6.108	7.555	0.433	1.154	0.748
17	1155.812	183.293	-1.4	6.472	7.607	0.442	1.154	0.670
18	1160.327	183.293	8.8	13.688	7.464	0.442	1.154	0.794
19	1161.855	172.795	-5.0	9.560	7.723	0.442	1.124	0.647
20	1164.145	172.795	-0.6	5.917	7.560	0.433	1.124	0.712
21	1175.352	172.795	-9.4	6.941	7.723	0.433	1.124	0.763
22	1205.055	172.795	2.5	5.780	7.723	0.433	1.124	0.749
23	1214.242	195.469	-0.9	7.911	7.132	0.442	1.183	0.787

* Corresponding author. E-mail: acimovicbabicmilica@gmail.com

Table S-I. Continued

No	$RI_{pred.}$	AATS0v	AATSC4c $\times 10^{-4}$	VR2 Dzi	VP-0	ETA Epsilon 3	IC0	BIC2
24	1220.251	195.469	8.5	7.064	7.257	0.433	1.183	0.725
25	1233.067	195.469	-10.0	7.675	7.257	0.433	1.183	0.725
26	1423.17	182.020	0.4	10.610	10.475	0.440	0.961	0.753
27	1469.839	182.020	-0.4	7.947	10.422	0.446	0.961	0.695
28	1491.72	182.020	-0,9	6.628	10.422	0.433	0.961	0.772
30	1493.986	182.020	-0.03	6.969	10.422	0.440	0.961	0.751
31	1502.399	182.020	0.5	7.513	10.638	0.440	0.961	0.711
33	1543.659	182.879	-0.3	6.024	10.792	0.445	1.106	0.719
34	1555.02	182.879	-1.2	7.221	10.883	0.445	1.106	0.711
35	1556.701	182.879	-1.7	22.398	10.831	0.439	1.106	0.735
36	1572.945	182.879	-6.2	7.221	10.792	0.439	1.106	0.777
37	1597.633	182.879	-4.6	7.351	10.629	0.439	1.106	0.736
38	1601.932	175.651	0.9	16.877	11.162	0.439	1.087	0.737
39	1646.202	173.568	0.9	15.457	10.619	0.418	1.067	0.737

$RI_{pred.}$ – predicted retention time, AATS0v - Average Broto-Moreau autocorrelation - lag 0 / weighted by van der Waals volumes; AATSC4c - Average centered Broto-Moreau autocorrelation - lag 4 / weighted by charges; VR2 Dzi - Normalized Randic-like eigenvector-based index from Barysz matrix / weighted by first ionization potential; VP-0 - Valence path, order 0; ETA Epsilon 3 - Extended topochemical atom descriptor; IC0 - Information content index, neighborhood symmetry of 0-orderand; BIC2 - Bond information content index (neighborhood symmetry of 2-order.

1) Tricyclene; 2) α-Thujene; 3) α-Pinene; 4) Camphene; 5) Thuja-2,4(10)-diene; 6) Sabinene; 7) β-Pinene; 8) dehydro-1,8-Cineole; 9) α-Terpinene; 10) p-Cymene; 11) 1,8-Cineole; 12) γ-Terpinene; 13) p-Mentha-2,4(8)-diene; 14) Linalool; 15) Z-p-Menth-2-en-1-ol; 16) α-Campholenal; 17) Camphor; 18) Z-Chrysanthenol; 19) Borneol; 20) δ-Terpineol; 21) Terpinen-4-ol; 22) α-Terpineol; 23) Myrtenal; 24) Thymol; 25) Carvacrol; 26) E-Caryophyllene; 27) allo-Aromadendrene; 28) Germacrene D; 30) γ-Cadinene; 31) δ-Cadinene; 33) Spathulenol; 34) Caryophyllene oxide; 35) β-Oplopenone; 36) Muurola-4,10(14)-dien-1-β-ol; 37) Caryophylla-4(12),8(13)-dien-5-α-ol; 38) epi-α-Cadinol; 39) α-Cadinol

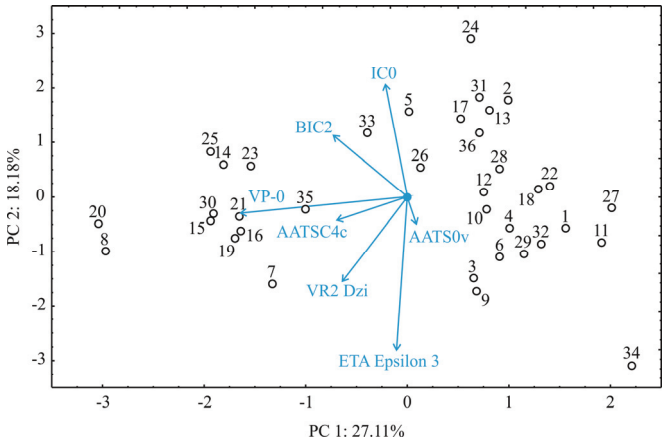

Fig. S-1. PCA ordination of molecular descriptors based on component correlations

Journal of the Serbian Chemical Society
JSCS-info@shd.org.rs • www.shd.org.rs/JSCS
J. Serb. Chem. Soc. *86* (4) 367–380 (2021)
JSCS–5427
Original scientific paper

Encapsulation of peach waste extract in *Saccharomyces cerevisiae* cells

DRAGOLJUB D. CVETKOVIĆ[1], ALEKSANDRA S. RANITOVIĆ[1]*, VANJA N. ŠEREGELJ[1], OLJA LJ. ŠOVLJANSKI[1], JELENA J. VULIĆ[1], BRANISLAV D. JOVIĆ[2] and VLADIMIR B. PAVLOVIĆ[3]

[1]*University of Novi Sad, Faculty of Technology, Bulevar cara Lazara 1, 21000 Novi Sad, Serbia,* [2]*University of Novi Sad, Faculty of Sciences, Department of Chemistry, Biochemistry and Environmental Protection, Trg Dositeja Obradovića 3, 21000 Novi Sad, Serbia and* [3]*University of Belgrade, Faculty of Agriculture, Nemanjina 6, 11080 Zemun, Serbia*

(Received 1 December 2020, revised 2 January, accepted 4 January 2020)

Abstract: As a secondary industrial product, peach waste (PW) presents an ecological problem, but is potentially a rich source of natural antioxidants. A potential and novel way to improve the phytochemical stability of waste rich in phytochemicals is encapsulation in yeast cells that possess good structural characteristics. In the present study, PW extract was encapsulated in non-plasmolyzed, plasmolyzed and living *Saccharomyces cerevisiae* cells using the freeze-drying method. HPLC analysis revealed that β-carotene is the most abundant carotenoid, while epicatechin and catechin are the most abundant phenolics in PW. The highest encapsulation efficiency of carotenoids (86.59 %), as well as phenolics (66.98 %), was obtained with freeze-dried non-plasmolyzed yeast cells used as carriers. Although plasmolysis can cause some changes in the structure and properties of yeast cells, it did not enhance the encapsulation efficiency of present phytochemicals. Successful encapsulation of PW extract in yeast cells was confirmed by FTIR spectroscopy and SEM imaging. The obtained results present the encapsulation of sensitive compounds in yeast cells by freeze-drying as an excellent method for preserving valuable compounds and their potential use in the food and pharmaceutical industries.

Keywords: phenolics; carotenoids; yeast; phytochemical stability; epicatechin; catechin.

INTRODUCTION

In fields of food, agriculture, and drug ingredients, many substances are useful for human health (antioxidants, essential oils, vitamins, *etc*.) and have technological or organoleptic functionalities (enzymes, aroma, natural colorant, *etc*.). Some of them are very sensitive to adverse environmental conditions, such

* Corresponding author. E-mail: sanja@tf.uns.ac.rs
https://doi.org/10.2298/JSC201201001C

as moisture, temperature, oxygen, or undesirable effects of light, or display negative properties of their targets, such as biocides or drugs.[1,2] One of the essential ways for preserving these substances is encapsulation in which small active compounds are surrounded by another material, thereby producing particles with diameters of a few nm to a few mm. The encapsulated substance may be called the core material, the active agent, fill or internal phase, while the surrounding material is called the coat, carrier, external phase or wall material.[3–5] Encapsulation prolongs the shelf life of some products under constantly changing storage conditions, stabilizes the active materials since the wall material acts as a physical barrier for oxygen or other molecules, preventing deleterious reactions, and enable the material to be released in a controlled way in product applications. Among the different techniques of encapsulation, freeze-drying is widely used in the food industry as one of the especially effective methods for bioactive compounds susceptible to degradation at high temperatures.[1,4,5]

The stability and release properties of encapsulates are dependent on the composition of the wall material and hence, various carriers have been used: sugars, cyclodextrins, maltodextrins, modified starches, gums, proteins, and liposomes.[5] The structure of the yeast cell wall made it an excellent and novel encapsulating material for the food industry,[1,4,6–8] which has many advantages over other encapsulation carriers: natural, food-grade, low cost, health benefits, thermostability and slow-release.[3,4,9] *Saccharomyces cerevisiae* cell wall is approximately 70–100 nm thick and is composed of *β*-glucans, a mannoprotein layer, and a small amount of chitin. Due to their phospholipid membranes, yeast cells can behave as liposomes and have been used for the encapsulation of both hydrophobic and hydrophilic molecules, such as essential oils,[10] resveratrol,[11] curcumin,[1] flavor compounds,[8] berberine,[4] chlorogenic acid[6] and enzymes.[7]

Peaches are a popular summer fruit, the increased consumption of which lowers the risk of chronic diseases, such as cardiovascular diseases, cancer, diabetes, *etc*. In the last decades, peach production is about 21 million tones around the world with an annual growth rate of more than 3 %. Peach cultivars rich in carotenoids and phenolics have higher antioxidant activities and represent excellent sources of natural antioxidants.[12] Phenolics in peach include hydroxycinnamic acids, such as caffeic, *p*-coumaric, ferulic, and chlorogenic acids, flavonols, such as quercetin glycosides (quercetin-3-galactoside, quercetin-3-glucoside, quercetin-3-rutinoside), flavanols, such as catechin, epicatechin, procyanidin B1, and anthocyanins, such as cyanidin-3-glucoside and cyanidin-3-rutinoside.[13,14] The carotenoid profile of peach includes *β*-carotene, *β*-cryptoxanthin, lutein, and zeaxanthin.[15]

By-products of plant food processing represent a major disposal problem for the industry concerned, even though they present promising sources of compounds that may be used for their high nutritional and excellent technological

properties.[16,17] Recovery of antioxidants from by-products of food processing plants has gained importance since the replacement of synthetic antioxidants with natural ones has benefits due to health implications and solubilities in food systems.[18] Peaches are composed of approximately 7–9 % of peel tissue and that the exocarp is a concentrated source of nutrients. It can be assumed that over 20 % of the total phytochemical concentration of a peach is lost if the peel is discarded and not consumed.[12] Peach juice by-product contains 37 % of dietary fiber and 0.5–8 % of total polyphenols, mainly kaempferol and quercetin 3-*O*-rutinoside.[19]

This study aimed at evaluating the feasibility of *Saccharomyces cerevisiae* cells as an encapsulation carrier for phytochemicals present in peach waste extract. Simple solvent extraction of peach waste and freeze-drying of the formulated encapsulation solutions was performed, and their potential to entrap and protect the present carotenoids and phenolics were evaluated. The distribution of peach waste extract in yeast cells was studied by Fourier transform infrared analysis and scanning electron microscopy.

EXPERIMENTAL

Preparation of Saccharomyces cerevisiae *cells*

The reference culture of *Saccharomyces cerevisiae* ATCC 9763 was grown on Sabouraud Maltose Agar slants (SMA, Himedia, Mumbai, India) for 48 h at 30 °C. After incubation, the cells were suspended in 5 mL phosphate buffer (pH 6.8), which was used as the inoculum for the second subculturing. The second subculturing was realized in Fernbach flasks with 250 mL Sabouraud Maltose broth (Himedia, Mumbai, India). The flasks were agitated at 180 rpm (Jeio Tech Lab, Korea) for 48 h at 30 °C.

From the yeast suspension, non-plasmolyzed (C1) and plasmolyzed (C2) yeast cells were prepared according to Paramera *et al*.[1] with some modifications. Briefly, before freeze-drying (Martin Christ, Apha 2-4 LSC, Germany), the samples were frozen in a deep freezer (Snijders Labs, Tilburg, The Netherlands). For yeast cell plasmolysis, a 10 % NaCl solution was used. For centrifugation, a Rotina 380R centrifuge (Hettich, Germany) was used. Alive yeast cells (C3) were prepared as the other two samples but without plasmolyzing and freezing.

Extraction of peach waste

Freeze-dried peach waste (PW), obtained using a Alpha 2-4 LSC Martin Christ freeze--drying apparatus (Osterode, Germany), was extracted three times using an acetone:ethanol mixture (36:64 volume ratio) at a solid to solvent ratio 1:20 w/v, with the same volume of solvents. The extraction was performed using a Unimax 1010 laboratory shaker (Heidolph Instruments GmbH, Kelheim, Germany) at 300 rpm, under light protection, at room temperature, for 10 min. The three obtained extracts were filtered (Whatman paper No. 1), combined, and stored in dark bottles at –20 °C until further analysis.

Encapsulation of peach waste extract in S. cerevisiae *cells*

Encapsulation by the freeze-drying technique was conducted following the method described by Šeregelj *et al*.[20] with modifications. Each yeast sample (7 g) was dissolved in 10 mL of water at 60 °C and kept under stirring until the temperature reached 30 °C. Separately, 50 mL of PW extract was combined with sunflower oil (1.5 mL), concentrated under reduced pressure on a rotary evaporator set at 40 °C to remove the organic solvent, and immediately

mixed with the previously prepared carrier solution. The mixtures were homogenized at 11000 rpm for 3 min at room temperature and frozen in a deep freezer. All samples were freeze-dried at –40 °C for 48 h. The obtained encapsulates were stored at –20 °C until further use.

Determination of yeast cell number

The total count of living yeast cells was determined by the plate counting method using SMA as the medium. In C1, the cell number was determined after subcultivation but before freeze-drying. In C2, the cell number was determined after subcultivation and plasmolysis but before freeze-drying. In C3, the cell number was determined after subcultivation. The encapsulation number was determined as E1 (encapsulated peach waste extract in non-plasmolyzed yeast cells), E2 (plasmolyzed freeze-dried yeast cells) as well as E3 (in alive yeast cells). The cells numbers are expressed as log CFU mL^{-1} of suspension and log CF mg^{-1} of encapsulate.

Determination of carotenoids content

Total carotenoid content (*T*Car), expressed as mg β-carotene per 100 g of dry PW or mg *β*-carotene per 100 g of encapsulate, was analyzed spectrophotometrically by the method of Nagata & Yamashita.[21] For the HPLC analysis of carotenoids, a solvent gradient was performed by varying the proportion of solvent A (water:methanol 1:4 v/v) to solvent B (acetone:methanol 1:1 volume ratio) at a flow rate of 1 mL min^{-1} with the following gradient profile: 25 % B 0–3 min; 75 % B 3–6 min; 90 % B 6–10 min; 100 % B 10–18 min; 50 % B 18–25 min; 25 % B 25–32 min. The column temperature was 25 °C and chromatograms were plotted at 450 and 475 nm. The carotenoids were dissolved in hexane and identified by matching the retention time and its spectral characteristics against those of standards.

Determination of phenolics contents

Total phenolic content (*T*Ph), expressed as mg gallic acid equivalents GAE per 100 g of dry PW or mg GAE per 100g of encapsulate, was determined spectrophotometrically by the Folin–Ciocalteau method adapted to microscale. For HPLC analysis of phenolic compounds, chromatograms were recorded using different wavelengths for individual phenolic compounds: 280 nm for hydroxybenzoic acids, 320 nm for hydroxycinnamic acids, and 360 nm for flavonoids following the method of Tumbas Šaponjac *et al.*[22]

Antioxidant activity of peach waste extract and encapsulates

The antioxidant activity of the PW extract and the obtained encapsulates was expressed as μmol Trolox equivalent, *TE* per 100 g of dry PW and μmol *TE* per 100 g of encapsulate, respectively. Three different methods were utilized: the 2,2-diphenyl-1-picrylhydrazyl method (SA) described by Girones-Vilaplana *et al.*,[23] reducing power (RP) by Oyaizu,[21] and *β*-carotene bleaching assay (BCB) by Al-Saikhan *et al.*[24] The SA and RP were performed on 70 % methanol extracts, while BCB was realized on hexane extracts.

Encapsulation efficiency

Determination of carotenoids encapsulation efficiency (*EE*Car, %) was based on the calculation of the concentration of carotenoids detected in the encapsulates (CC) over the initial concentration of carotenoids added to make the encapsulates (IC). The *T*Car concentrations were determined spectrophotometrically by the method described above. Thus, the *EE*Car was determined using Eq. (1):[25]

$$EE\text{Car} = 100(w(\text{CC})/w(\text{IC})) \quad (1)$$

Determination of phenolics encapsulation efficiency (*EE*Ph, %) was performed by the Tumbas Šaponjac *et al.* method.[25] The concentration of the surface phenolics (*SP*) and total

phenolics (*TP*) in the PW encapsulates were determined by the Folin–Ciocalteu method described above. The *EE*Ph was determined using Eq. (2):

$$EE\text{Ph} = 100(w(\text{TP})–w(\text{SP}))/w(\text{TP}) \quad (2)$$

Characterisation of the encapsulates

In order to confirm the encapsulation of peach waste extract in yeast cells, FT-IR analysis was performed among carriers and as well as the obtained encapsulates and PW. The FTIR spectra of the samples were recorded on a Thermo Nicolet Nexus 670 FTIR spectrophotometer using the transmission technique in KBr pellets. For all spectra, 32 scans were recorded and averaged with a resolution of 4 cm^{-1} for each spectrum. A DTGS detector was employed in the IR measurements.

Morphological analysis of the surface of the samples was performed using a JEOL JSM--6390LV scanning electron microscope (JEOL Ltd., Tokyo, Japan). Prior to the analysis, (acceleration voltage 15 kV, beam current 20 nA, spot size 1 mm), the samples were sputter--coated with gold during 100 s under 30 mA ion current on BALTEC SCD 005 sputter coater (Capovani Brothers Inc., Scotia, NY).

Statistical analysis

All experiments were run in triplicate. The results presented are means ± standard deviation (±*SD*, $n = 3$). Statistical analyses were realized using Origin 8.0 SRO software package and Microsoft Office Excel 2010 software. Significant differences were calculated by ANOVA ($p < 0.05$).

RESULTS AND DISCUSSION

A potential and novel way to improve the phytochemical stability of waste rich in phytochemicals is encapsulation in yeast cells that possess good structure characteristics. In this study, the number of yeast cells was determined during the above-mentioned treatments to show how these treatments affect changes in the number of yeast cells. The results of the number of yeast cells in C 1–3 and appropriate encapsulates are given in Table I. According to the obtained results for the cells number, C1 and C3 after subcultivation are similar. In C2, after plasmolysis, the cell number was reduced by about 6 log units, which means that the NaCl concentration for plasmolysis was insufficient for total reduction. According to the gained number in encapsulates after freeze-drying (Table I), showed that these processes significantly inhibit the growth of cells.

TABLE I. Number of *Saccharomyces cerevisiae* cells; data present the mean value of three replicates ±*SD*; values sharing the same letter (a, b and c) in the same row are not significantly different at the 0.05 level according to Tukey's HSD test

Sample number	Number of yeast cells	
	Carriers (C) (log (CFU ml^{-1}))	Encapsulates (E) (log (CFU mg^{-1}))
1	$9.62±0.04^c$	$2.69±0.01^a$
2	$3.69±0.11^a$	$< 4^c$
3	$9.30±0.08^b$	$3.84±0.01^b$

Namely, the freeze-drying process was lethal for almost all cells in E2. In E1, the number was reduced for 7 log units, and in E3 for 6 log units. Plasmolysis can potentially increase the available encapsulation intercellular space and increase encapsulation efficiency. However, the loss in viability does not have a significant effect on yeast loading because encapsulation is mostly driven by passive diffusion of the substance throughout the cell envelope. On the other hand, proteins, polysaccharides, and other cellular components can make retention and interaction of the active ingredient more difficult.[2,9]

The phytochemical profile (carotenoids and phenolics) determined by spectrophotometric and HPLC analyses are presented in Table II. The data from the HPLC analysis revealed the presence of β-carotene as predominant carotenoid and *β*-cryptoxanthin.

The obtained results of the phytochemical content of peach waste extract and encapsulates (Table II) are in accordance with spectrophotometrical data, where E1 exhibited a significantly higher *T*Car ($p < 0.05$) compared with E2 and E3. Giuffrida *et al.*[26] found three free carotenoids (zeaxanthin, *β*-carotene, and *β*--cryptoxanthin) in the peach extract, juice, and jam, whereby *β*-carotene was the most abundant in all samples. The carotenoid profile reported by Dalla Valle *et al.*[15] included *β*-carotene, *β*-cryptoxanthin, lutein, zeaxanthin, and lesser amounts of additional related compounds.

The phenolics profile determined by HPLC analysis includes the presence of four phenolic acids (*p*-coumaric, *p*-hydroxybenzoic, caffeic, and chlorogenic acid), and four flavonoids (catechin, epicatechin, rutin, and quercetin). Epicatechin and catechin are the most abundant compounds, the quantities of which significantly differ among the samples. These findings could be explained by the difference in the applied encapsulation carriers based on yeast pretreatment, as well as their different capacity for bonding various compounds. Similar phenolics and flavonoids profiles were also reported by Stojanovic *et al.*[27] who studied peach pulp and peel extracts. They reported that the peach pulp contains mainly chlorogenic, neochlorogenic, and *p*-coumaric acids, whereas the peel contains chlorogenic, neochlorogenic and *p*-coumaric acids together with several flavanol glycosides in huge amounts. Furthermore, Andreotti, Ravaglia *et al.*[23] detected chlorogenic acid, catechin, epicatechin, rutin, and cyanidin-3-glucoside as the main phenolic compounds of ripened peach fruits. Generally, the present HPLC results showed the presence of the same groups of phenolic compound as in the available literature.

The antioxidant activity of carotenoids is based on the scavenging peroxyl radicals and quenching of single oxygen ($^1O_2$), while phenolics act as reducing agents, free radical scavengers, and quenchers of $^1O_2$ formation.[29] There is no single chemical assay that can accurately evaluate the contribution of the hydrophobic and hydrophilic compounds to the total antioxidant activity of the plants.

Therefore, several assays were performed, *i.e.*, SA and RP with hydrophilic fractions, and BCB with hydrophobic fractions (Fig. 1). The SA and RP tests (Fig. 1) showed significantly higher values for E1 and E3, which could be correlated with the phenolic content of the mentioned encapsulates.

TABLE II. Total and individual contents of carotenoids and phenolics; *: non-plasmolyzed; **: plasmolyzed freeze-dried; ***: alive. Data present the mean value of three replicates±*SD*; values sharing the same letter (a, b, and c) in the same row are not significantly different at the 0.05 level according to the Tukey's HSD test

Compound	Unit	Sample			
		PW extract	Yeast cells		
			E1*	E2**	E3***
Spectrophotometrical analysis					
*T*Car	mg *β*-carotene (100 g^{-1})	1.9±0.3^{d}	1.4±0.1^{c}	0.7±0.0^{b}	0.2±0.1^{a}
*T*Ph	mg GAE (100 g^{-1})	641.6±13.9^{d}	571.4±39.8^{c}	146.8±17.1^{a}	386.5±4.6^{b}
HPLC analysis					
Epicatechin	mg (100 g^{-1})	12.9±2.6^{b}	303.2±2.1^{c}	24.0±0.1^{a}	351.6±1.3^{d}
Catechin		493.3±6.1^{d}	8.5±0.3^{a}	35.7±0.3^{b}	230.9±2.7^{c}
Caffeic acid		3.0±0.1^{c}	0.1±0.0^{a}	0.1±0.0^{a}	0.4±0.0^{b}
p-Coumaric acid		3.0±0.2^{d}	0.3±0.0^{b}	0.1±0.0^{a}	1.2±0.0^{c}
Chlorogenic acid		13.4±0.5^{d}	1.1±0.0^{b}	0.4±0.1^{a}	4.6±0.0^{c}
p-Hydroxybenzoic acid		30.4±1.8^{d}	2.0±0.0^{b}	1.0±0.0^{a}	6.8±0.1^{c}
Rutin		0.3±0.1^{c}	0.2±0.1^{b}	0.1±0.0^{a}	0.1±0.0^{a}
Quercetin		0.2±0.0^{b}	0.1±0.0^{a}	0.2±0.0^{b}	0.1±0.0^{a}
Total phenolics		556.6±14.3^{c}	315.5±2.4^{b}	61.6±4.5^{a}	595.7±12.3^{d}
β-Cryptoxanthin		0.2±0.0^{c}	0.1±0.0^{b}	0.1±0.0^{b}	0.0±0.0^{a}
β-Carotene		1.3±0.2^{c}	1.5±0.3^{c}	0.1±0.0^{a}	0.1±0.0^{a}
Total carotenoids		1.5±0.2^{c}	1.6±0.9^{c}	0.2±0.0^{a}	0.1±0.0^{a}

On the other hand, the BCB assay showed a strong relationship between carotenoids content and their potential to neutralize the linoleate free radicals and other free radicals formed in the *β*-carotene–linoleic acid system.

Phytochemicals derived from plants have numerous health benefits, and the therapeutic potential to cope with oxidative stress caused diseases when consumed at a proper level. These natural antioxidants, especially carotenoids and phenolics, exhibit a wide range of biological effects due to their action as free radical scavengers and inhibitors of lipid peroxidation. Generally, the antioxidant capacities of the samples were strongly dependent on the employed solvent, due to the different antioxidant potential of the compounds with different polarities.[26]

As presented in Table III, *Saccharomyces cerevisiae* yeast cells have been investigated for the encapsulation of hydrophobic (carotenoids) and hydrophilic compounds (phenolics).

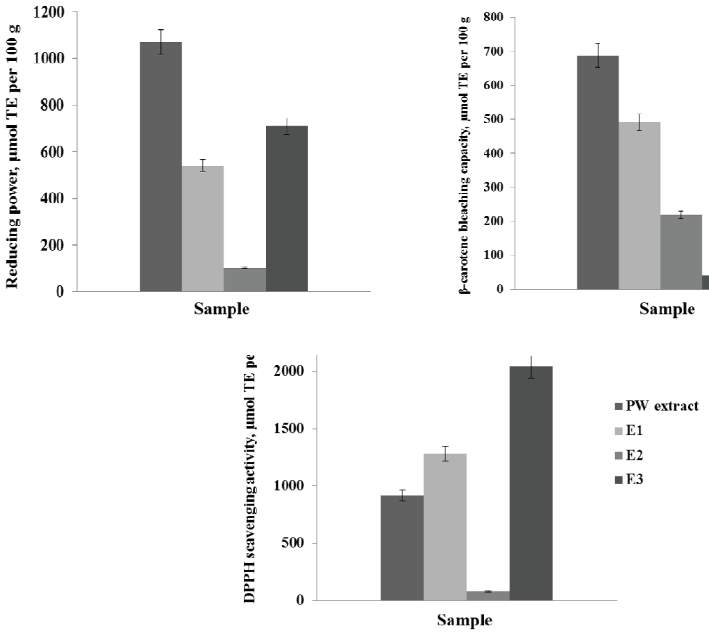

Fig. 1. Antioxidant activity of peach waste extract and encapsulates.

TABLE III. The encapsulation efficiency (%) of carotenoids and phenolics; the data present the mean value of three replicates±*SD*; Values sharing the same letter (a, b, and c) in the same row are not significantly different at the 0.05 level according to the Tukey's HSD test

Yeast sample	Component	
	Carotenoids (*EE*Car)	Phenols (*EE*Ph)
Non-plasmolyzed (E1)	86.59±4.61^{c}	66.98±0.39^{c}
Plasmolyzed freeze-dried (E2)	63.17±6.72^{b}	24.59±4.01^{a}
Alive (E3)	26.97±5.10^{a}	46.82±4.83^{b}

As presented in Table III, the *EE*Car value ranged from 26.97 to 86.59 %. The highest *EE*Car value (86.59 %) was obtained with freeze-dried non-plasmolyzed yeast suspension (E1). The same trend was observed for *EE*Ph, where the application of non-plasmolyzed yeast suspension as the carrier exhibited the highest efficiency (66.98 %). As previously mentioned, the increasing intracellular space by the loss of cytoplasmic materials could be effective concerning the encapsulation efficiency. For this purpose, plasmolysis with a NaCl solution is commonly used as a pretreatment for the reduction of the intracellular contents of cells. Some studies reported a greater increase in the encapsulation efficiency after yeast cell pretreatment. Thus, Shi *et al.*[6] showed a two-fold higher encapsulation efficiency of chlorogenic acid in plasmolyzed yeast cells. Dadkhodazade *et al.*[30] reported the highest *EE* value (76.10 %) obtained with spray-dried plasmolysed yeast cell encapsulates. Kavosi[31] *et al.* revealed increasing purslane oil

encapsulation efficiency from 52.96 to 60.27 % on increasing the intracellular space. However, Paramera *et al.*[1] observed that cell plasmolysis had no significant increase on the encapsulation efficiency of curcumin. According to their explanation, curcumin was entrapped in the yeast cell by its adhesion to the cytoplasmic cell membranes or by interaction with the constituents of the cell walls *via* hydrogen bonds. Therefore, the removal of water-soluble components of the cytoplasm had no significant effect on curcumin uptake. Bishop *et al.*[10] also showed effective encapsulation of essential oils in *Saccharomyces cerevisiae* without prior plasmolysis. Differences among the results could be explained by the permeation of both hydrophobic and hydrophilic molecules, as well as the physicochemical properties of the cell wall.[2] The encapsulation efficiency also depends strongly on the purity of the target molecules.[6] Variations in the results could also be caused by the molecular size of the permeating compounds, diversity of treatments, and encapsulation protocols.

The FT-IR spectra of non-plasmolyzed, plasmolyzed freeze-dried yeast cells, alive yeast cells (C1–C3) and appropriate encapsulates (E1–E3) with PW extract, as well as the initial PW extract, are shown in Fig. 2.

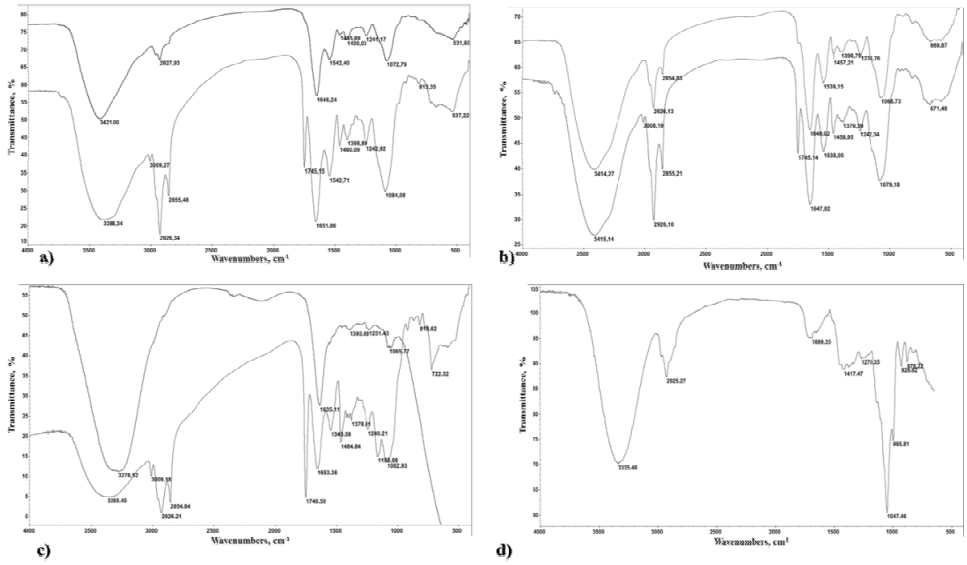

Fig. 2. FT-IR spectra of samples: a) non-plasmolyzed, b) plasmolyzed freeze-dried yeast cells, c) alive yeast cells (C1–C3) and appropriate encapsulates (E1–E3) with PW extract; d) initial PW extract.

Plasmolysis is the phenomenon in which intracellular water is drawn out of the cell and because of the internal water loss, the cell membrane contracts from the cell wall. This phenomenon occurs by modifying the structure of the cell wall

and particularly of the membrane that affects the lipids, proteins, nucleic acids, and carbohydrates of the whole yeast cell, cell wall, and membrane.[1] Due to these changes, some differences between the spectra of non-plasmolyzed, alive, and plasmolyzed yeast cells appeared (Fig. 2a–c). Changes in the region 3000––2800 cm^{-1} indicate modifications of the length of the lipid chains and the structure of the yeast membrane. Changes in the peak shapes in the region 1800–1500 cm^{-1} indicate partial protein degradation mainly involving the yeast cell wall. Peaks within this region are associated with amide I and II signals of the protein, carbonyl stretching modes of the pectic polysaccharides, and the O–H bending mode of water.[32] Changes in peak shapes in the band region 1500–1390 cm^{-1} indicate degradation of one part of the yeast proteins mainly involving the cell membrane and the cell wall, while changes in peak shapes in the region 1100––700 cm^{-1} indicate degradation of the cell wall of the polysaccharides (glucans and mannans). The results showed that plasmolysis disorganized the yeast plasma membrane and increased its fluidity. Furthermore, the yeast cell wall became thinner since the mannoproteins were partially degraded along with β-1,4- and β-1,6-glucans.

From the FT-IR spectra of the PW extract (Fig. 2d) some peaks that belong to carbohydrates (region 1100–700 cm^{-1}) are visible (for example, peaks 1047, 995, 926, 877 cm^{-1}). These peaks did not exist in the spectra of yeast cells, while in the encapsulates,, these peaks disappeared or their shape is changed (Figs. 2a––c). This indicates to the fact that the main bands of the PW extract weakened when they interacted with yeast cell components and that extract molecules are rather located inside the yeast cells. This was confirmed by the fact that the FT--IR spectra of the encapsulates are similar to the spectra of the carriers (Figs. 2a––c). In all three encapsulates, it could be noted that the position of the carbonyl peak was at a high wavenumber value (1745 cm^{-1}). Since the position of the carbonyl group in the proteins (more bonded, less free) is around 1650 cm^{-1}, it could be assumed that this carbonyl group is freer in vibration, *i.e.*, protein degradation has occurred maybe because of interaction with the extract. The results are in accordance with those of Shi *et al.*[6] and Paramera *et al.*[1], who encapsulated chlorogenic acid and resveratrol, as well as curcumin in yeast cells, respectively.

From the results, it could be confirmed that peach PW was successfully incorporated into the yeast cells by intermolecular interactions and their integrity was preserved after the freeze-drying process. This means the different yeasts used as carriers are compatible materials for PW extract encapsulation according to the FT-IR analysis.

The SEM images of non-plasmolyzed, plasmolyzed freeze-dried yeast cells (C1–C2) and corresponding encapsulates (E1–E2), as well as encapsulates in alive yeast cells (E3), are shown in Fig. 3.

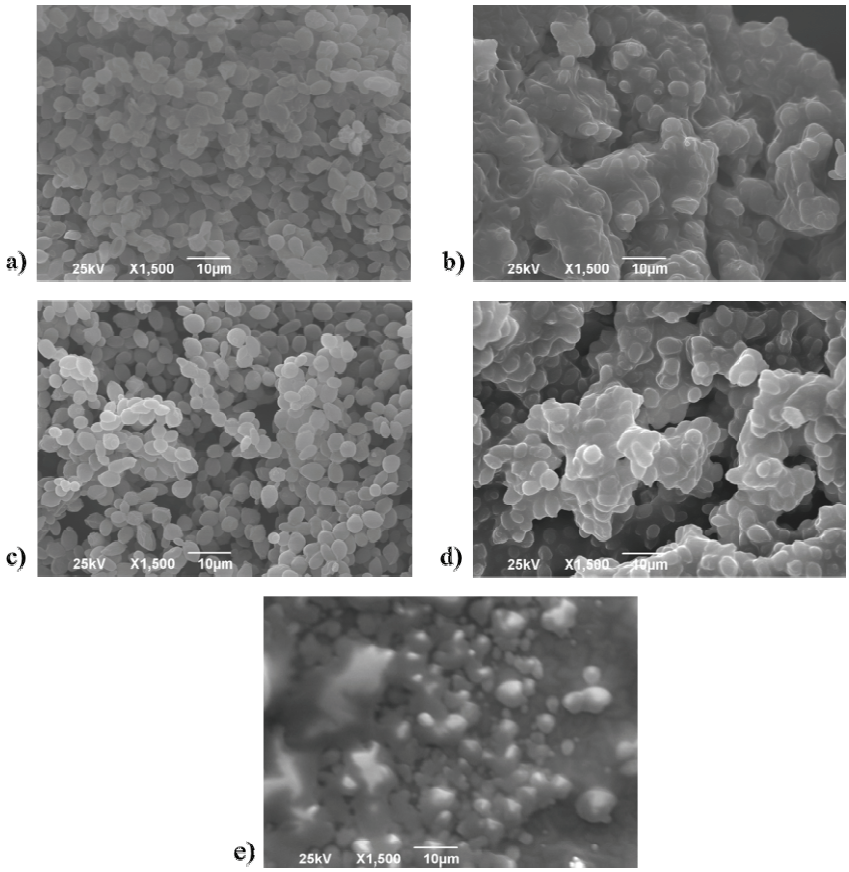

Fig. 3. SEM images of samples: a) non-plasmolyzed and c) plasmolyzed freeze-dried yeast cells (C1–C2), and b, d) appropriate encapsulates (E1–E2), as well as e) encapsulates in alive yeast cells (E3).

It could be seen from Fig 3a–c that the PW extract was successfully encapsulated in yeast cells, both non-plasmolyzed, plasmolyzed, and alive. Additionally, there were no differences in the morphological properties of the cell wall of the yeast cells and PW extract loaded yeast cells, *i.e.*, the surface morphology was intact and with no burst on the surface. This explains the absence of difference in non-plasmolyzed and plasmolyzed yeast cells (Figs. 3a and c) because the plasma membranes are often considered to be the primary site of osmotic injury.[28] The results are in accordance with those of Salari *et al.*[4] who concluded that the encapsulation process did not affect the organization of the cell wall.

CONCLUSIONS

This study shows that peach waste could be encapsulated in non-plasmolyzed, plasmolyzed and living *Saccharomyces cerevisiae* yeast cells. The best

encapsulation efficiency was achieved with freeze-dried, non-plasmolyzed yeast cells, However, Fourier transform infrared spectroscopy and scanning electronic microscopy confirmed encapsulation was also obtained for plasmolyzed, and living cells. Overall, it could be concluded that peach waste, a rich source of valuable bioactive compounds (phenolics and *β*-carotenes), encapsulated in yeast cells as carriers could find possible use in the food and pharmaceutical industries. Struggling with the disposal of organic fruit waste around the world and providing recovery of health–improving substances that have great potential for utilization and high functional properties for the food industry, this study explains carotenoids and phenolics encapsulation in yeast cells which could be a promising technique for the stability of peach waste extract for all production levels.

Acknowledgment. The financial support of the Ministry of Education, Science, and Technological Development of the Republic of Serbia (Contract No. 451–03–68/2020–14/200134) is gratefully acknowledged.

И З В О Д

ИНКАПСУЛАЦИЈА СПОРЕДНОГ ПРОИЗВОДА ПРЕРАДЕ БРЕСКВЕ У ЋЕЛИЈЕ КВАСЦА *Saccharomyces cerevisiae*

ДРАГОЉУБ Д. ЦВЕТКОВИЋ[1], АЛЕКСАНДРА С. РАНИТОВИЋ[1], ВАЊА Н. ШЕРЕГЕЉ[1], ОЉА Љ. ШОВЉАНСКИ[1], ЈЕЛЕНА Ј. ВУЛИЋ[1], БРАНИСЛАВ Д. ЈОВИЋ[2] и ВЛАДИМИР Б. ПАВЛОВИЋ[3]

[1]Универзитет у Новом Саду, Технолошки факултет Нови Сад, Булевар цара Лазара 1, 21000 Нови Сад, [2]Универзитет у Новом Саду, Природно–математички факултет, Трг Доситеја Обрадовића 3, 21000 Нови Сад и [3]Универзитет у Београду, Пољопривредни факултет, Немањина 6, 11080 Земун

Секундарни производ прераде бресквe (PW) представља еколошки проблем, али и потенцијални извор природних антиоксиданата. Један од иновативних начина да се повећа стабилност фитохемикалија из споредних производа јесте инкапсулација у ћелије квасца, који поседује добре структурне карактеристике. У овом раду, PW екстракт је инкапсулиран методом лиофилизације у неплазмолизираним, плазмолизираним и живим ћелијама *Saccharomyces cerevisiae*. HPLC анализом је утврђено да је β-каротен најдоминантнији каротеноид, док су епикатехин и катехин најдоминантнији феноли у PW екстракту. Највећа ефикасност инкапсулације каротеноида (86,59 %), као и фенола (66,98 %) је постигнута приликом инкапсулације PW екстракта у лиофилизиране, неплазмолизиране ћелија квасца. Иако плазмолиза може изазвати промене у структури и особинама ћелије квасца, овај поступак није утицао на повећање ефикасности инкапсулације присутних фитохемикалија. Успешна инкапсулација PW екстракта у ћелије квасца потврђена је и FT-IR спектроскопијом и SEM микроскопијом. На основу резултата овог рада може се закључити да је примењена метода инкапсулације осетљивих једињења у ћелије квасца адекватна основа за стабилизацију вредних компоненти и њихову потенцијалну употребу у прехрамбеној и фармацеутској индустрији.

(Примљено 1. децембра 2020, ревидирано 2. јануара, прихваћено 4. јануара 2021)

REFERENCES

1. E. I. Paramera, S. J. Konteles, V. T. Karathanos, *Food Chem., A* **74** (2011) 125 (https://doi.org/10.1016/j.foodchem.2010.09.063)

2. B. N. Pham-Hoang, C. Romero-Guido, Y. Waché, *Appl. Microbiol. Biotechnol.* **97** (2013) 6635 (https://doi.org/10.1007/s00253-013-5044-1)
3. E. I. Paramera, S. J. Konteles, V. T. Karathanos, *Food Chem., B* **125** (2011) 913 (https://doi.org/10.1016/j.foodchem.2010.09.071)
4. R. Salari, O. Rajabi, Z. Khashyarmanesh, M. Fathi Najafi, B. S. FazlyBazzaz *Iranian J. Pharm. Res.* **14** (2015) 1247 (PMCID: PMC4673954)
5. S. Mokhtari, S. Mahdi Jafari, M. Khomeiri, Y. Maghsoudlou, Y. Ghorbani, *Food Res. Int.* **96** (2017) 1 (https://doi.org/10.1016/j.foodres.2017.03.014)
6. G. Shi, L. Rao, H. Yu, H. Xiang, G. Pen, S. Long, C. Yang, *J. Food Eng.* **80** (2007) 1060 (https://doi.org/10.1016/j.jfoodeng.2006.06.038)
7. C. K. Chow, S. Palecek, *Biotech. Prog.* **20** (2004) 449 (https://doi.org/10.1021/bp034216r)
8. V. Normand, G. Dardelle, P. E. Bouquerand, L. Nicolas, D. J. Johnston, *J. Agric. Food Chem.* **53** (2005) 7532 (https://doi.org/10.1021/jf0507893)
9. E. I. Paramera, V. T. Karathanos, S. J. Konteles, *Yeast cells and yeast-based materials for microencapsulation*, Elsevier Inc., Amsterdam, 2014, p. 267 (https://doi.org/10.1016/C2012-0-00852-6)
10. J. R. P. Bishop, G. Nelson, J. Lamb, *J. Microencapsulation* **15** (1998) 761 (https://doi.org/10.3109/02652049809008259)
11. G. Shi, L. Rao, H. Yu, H. Xiang, H. Yang, R. Ji, *Int. J. Pharm*. **349** (2008) 83 (https://doi.org/10.1016/j.ijpharm.2007.07.044)
12. F. Saidani, R. Giménez, C. Aubert, G. Chalot, J. A. Betrán, Y. Gogorcena, *J. Food Compos. Anal.* **62** (2017) 1 (https://doi.10.1016/j.jfca.2017.04.015)
13. I. Hasbay Adil, I. H. Çetin, M. E. Yener, A. Bayındırlı, *J. Supercrit. Fluids* **43** (2007) 55 (https://doi.org/10.1016/j.supflu.2007.04.012)
14. X. Liao, P. Greenspan, R. B. Pegg, *Food Chem.* **271** (2019) 1 (https://doi.org/10.1016/j.foodchem.2018.07.163)
15. A. Dalla Valle, I. Mignani, A. Spinardi, F. Galvano, S. Ciappellano, *Eur. Food Res. Technol.* **225** (2007) 167 (https://doi.org/10.1007/s00217-006-0396-8)
16. A. Schieber, F. C. Stintzing, R. Carle, *Trends Food Sci. Technol.* **12** (2001) 401 (https://doi.org/10.1016/S0924-2244(02)00012-2)
17. H. Kowalska, K. Czajkowska, J. Cichowska, A. Lenart, *Trends Food Sci. Technol.* **67** (2017) 1 (https://doi.org/10.1016/j.tifs.2017.06.016)
18. I. Hasbay Adil, H. I. Çetin, M. E. Yener, A. Bayındırli, *J. Supercrit. Fluids* **43** (2007) 55 (https://doi.org/10.1016/j.supflu.2007.04.012)
19. S. Rodríguez-González, I. F. Pérez-Ramírez, D. M. Amaya-Cruz, M. A. Gallegos-Corona, M. Ramos-Gomez, O. Mora, R. Reynoso-Camacho, *J. Funct. Foods* **45** (2018) 58 (https://doi.org/10.1016/j.jff.2018.03.010)
20. V. Šeregelj, G. Ćetković, J. Čanadanović-Brunet, V. Tumbas-Šaponjac, J. Vulić, S. Stajčić, *Acta Period. Tech.* **48** (2017) 261 (https://doi.org/10.2298/APT1748261S)
21. M. Nagata, I. Yamashita, *Japan Soc. Food Sci. Technol.* **39** (1992) 925 (https://doi.org/10.3136/nskkk1962.39.925)
22. A. Girones-Vilaplana, P. Mena, D. A. Moreno, C. Garcia-Viguera, *J. Sci. Food Agric*. **94** (2014) 1090 (https://doi.org/10.1002/jsfa.6370)
23. M. Oyaizu, *Japanese J. Nutr. Dietet.* **94** (1986) 307 (https://doi.org/10.5264/eiyogakuzashi.44.307)
24. M. S. Al-Saikhan, L. R. Howard, Jr. JC. Miller, *J. Food Sci.* **60** (1995) 341 (https://doi.org/10.1111/j.1365-2621.1995.tb05668.x)

25. V. Tumbas Šaponjac, G. Ćetković, J. Čanadanović-Brunet, B. Pajin, S. Djilas, J. Petrović, J. Vulić, *Food Chem.* **207** (2016) 27 (https://doi.org/10.1016/j.foodchem.2016.03.082)
26. D. Giuffrida, G. Torre, G. Dugo, *Fruits* **68** (2012) 39 (https://doi.org/10.1051/fruits/2012049)
27. B. T. Stojanovic, S. S. Mitic, G. S. Stojanovic, M. M. Mitic, D. A. Kostic, D. D. Paunovic, B. Arsic, *Notulae Botanicae Horti Agrobotanici Cluj-Napoca* **44** (2016) 175 (https://doi.org/10.15835/nbha44110192)
28. C. Andreotti, D. Ravaglia, A. Ragaini, G. Costa, *Ann. App. Biol.* **153** (1998) 11 (https://doi.org/10.1111/j.1744-7348.2008.00234.x)
29. C. Forni, F. Facchiano, M. Bartoli, S. Pieretti , A. Facchano, D. D'Arcamgelo, S. Norelli, G. Valle , R. Nisini , S. Beninati , C. Tabolacci, R. N. Jadeja, *Bio. Med. Res. Int*. (2019) (ID: 8748253)
30. E. Dadkhodazade, A. Mohammadi, S. Shojaee-Aliabadi, A. M. Mortazavian, L. Mirmoghtadae, S. M. Hosseni, *Food Biophys.* **13** (2018) 231 (https://doi.org/10.1007/s11483-018-9546-3)
31. M. Kavosi, A. Mohammadi, S. Shojaee-Aliabadi, R. Khaksar, S. M. Hosseini, *J. Sci. Food Agric.* **98** (2018) 1 (https://doi.org/10.1002/jsfa.8696)
32. G. J. Morris, L. Winters, G. E. Coulson, K. J. Clarke, *J. Gen. Microbiol.* **129** (1984) 2023 (https://doi.org/10.1099/00221287-132-7-2023).

Journal of the Serbian Chemical Society
JSCS-info@shd.org.rs • www.shd.org.rs/JSCS
J. Serb. Chem. Soc. *86* (4) 381–391 (2021)
JSCS–5428
Original scientific paper

Prediction of retardation factor of protein amino acids in reversed phase TLC with ethanol–sodium azide solution as the mobile phase using QSRR

SUSAN TORABI[1], FATEMEH HONARASA[2] and SAEED YOUSEFINEJAD[3]*

[1]*Deputy of Food and Drug Control, Shiraz University of Medical Sciences, Shiraz, Iran,* [2]*Department of Chemistry, Shiraz Branch, Islamic Azad University, Shiraz, Iran and* [3]*Research Center for Health Sciences, Institute of Health, Department of Occupational Health Engineering, School of Health, Shiraz University of Medical Sciences, Shiraz, Iran*

(Received 11 June, revised 30 August, accepted 6 October 2020)

Abstract: Due to the importance of amino acids (AAs) as the basic bricks of proteins and their application in the drug and food industries, there is great interest in their separation and identification using simple and inexpensive approaches. Application of predictive models for the determination of the behavior of AAs can reduce trial-and-error experiments. Herein, the retardation factor (*RF*) of 21 protein AAs were studied using the quantitative structure-retardation factor (QSRR) model. The *RF* values of the AAs in ethanol–sodium azide solution as the mobile phase of reversed phase thin layer chromatography (RP-TLC) were correlated with the structural properties of the AAs. The suggested QSRR indicated excellent fitting and prediction ability (R2train = 0.95 and R2test = 0.94). Furthermore, other statistical tests, such as *y*-scrambling, cross validation and the Williams plot confirmed the stability, absence of chance and the suitable applicability domain, respectively. It was shown that the sum of geometrical distances between oxygen and nitrogen atoms in an AA molecule is an important factor for the *RF* values of the AAs in the ethanol––sodium azide.

Keywords: natural amino acids; descriptors; structural property; thin layer chromatography; QSRR.

INTRODUCTION

Finding correlation and relationship between chromatographic retention time or retardation indices and structural parameters of the desired analysts is an interesting subject because it is a way to obtain basic information on the impact of the structural features on the retention/retardation indices and to give an insight into possible mechanisms for separation forces and elution process.[1,2]

* Corresponding author. E-mail: yousefisa@sums.ac.ir
https://doi.org/10.2298/JSC200611065T

The ideal objective of models of quantitative structure-retention relationships (QSRR), as a subfield in quantitative structure-retention relationships (QSPR), is its application to predict the retention behavior of newly identified molecules and similar synthesized derivatives or to estimate the involved mechanisms during various interactions, such as solute–solute, solute–stationary phase and solute–mobile phase.[3,4] The prediction of retention/retardation of compounds in chromatographic systems using QSRR can reduce trial-and-error experiments, which is important in some series of species such as polychlorinated biphenyls (PCBs), polybrominated, diphenyl ethers (PBDEs), polychlorinated dibenzofurans (PCDFs), *etc.* This could be significant in such compounds due to their toxicity or scarce information about some of their derivatives.[5,6]

Different QSRR studies have been conducted on various chromatography methods, such as reverse phase- and normal phase-high performance chromatography (RP-HPLC and NP-HPLC), micellar HPLC, gas chromatography, high performance affinity chromatography, immobilized artificial membranes, and planar chromatography, which are reviewed in different articles.[5,7,8]

RP-TLC is one of the most popular techniques and its retention mechanism is based on partitioning of the compounds between hydrophilic mobile phase and hydrophobic stationary phase. Due to the nature and mechanism of RP-TLC, the lipophilicity of the analytes has an effect on their retention with a strict correlation.[9]

Analysis and identification of amino acids (AAs) is of high importance because AAs are the basic units of biomolecules, enzymes, peptides, and protein and have impacts in the food and drug industries. Separation and identification of AAs (protein or non-protein) have been intensively performed with column chromatography and their separation using simple methods, such as thin layer chromatography (TLC), have been considered in many studies.[10,11] In a previous study, a QSRR model was reported for separation of AAs in Normal Phase TLC (NP-TLC) by considering both the properties of the mobile phase and the structures of AAs.[12] To show the ability of QSRR in modeling the behavior of AAs in RP-TLC, a QSRR modeling was recently designed in two different mobile phases and the potential of structure-chromatography was confirmed in this case.[13] However, because the recent work was performed by considering only the structure of the AAs, more studies are required to show the capability of the QSRR approach in the separation of AAs in RP-TLC in various mobile phases. Thus, in the current study, a QSRR model was developed for the retardation factor (R_F) of 21 protein AAs in RP-TLC using an ethanol–sodium azide solution as a well-known mobile phase to identify the significant features in this elution process.

MATERIALS AND METHODS

The retardation factor (R_F) for the studied AAs using RP-TLC in ethanol–sodium azide were adopted from literature[10] and are given in Table I.

TABLE I. Experimental and predicted R_F of 21 AAs in ethanol–sodium azide and related residual values

Code	Name	R_F (Exp)	R_F (Pred)	Residual
AA 1	Glycine	0.82	0.84	0.02
AA 2	Alanine	0.82	0.78	–0.04
AA 3	Aspartic acid	0.25	0.35	0.10
AA 4	Arginine	0.13	0.14	0.01
AA 5	Proline	0.78	0.65	–0.13
AA 6	Hydroxyproline	0.84	0.88	0.04
AA 7	Lysine	0.02	0.02	0.00
AA 8	Glutamic acid	0.86	0.74	–0.12
AA 9[a]	Serine	0.8	0.74	–0.06
AA 10	Tryptophan	0.83	0.87	0.04
AA 11	Valine	0.83	0.89	0.06
AA 12	Phenyl alanine	0.83	0.90	0.07
AA 13	Isoleucine	0.88	0.84	–0.04
AA 14[a]	Leucine	0.88	0.97	0.09
AA 15	Asparagine	0.62	0.60	–0.02
AA 16	Methionine	0.83	0.84	0.01
AA 17	Cysteine	0.84	0.88	0.04
AA 18[a]	Histidine	0.33	0.35	0.02
AA 19	Threonine	0.83	0.80	–0.03
AA 20[a]	Tyrosine	0.83	0.83	0.00
AA 21[a]	Glutamine	0.77	0.72	–0.05

[a]AA samples used as the test set

The structural properties were produced from 22 categories of descriptors, *i.e.*, topological, constitutional, topological charge indices, geometrical, connectivity, RDF, 3D MoRSE, WHIM, GETAWAY, functional group counts, and some other groups were extracted.[14] The extracted descriptors were from a variety of kinds of features to cover the structural details of natural AAs. The structural descriptors were arranged in a matrix (D) of size of 21×c where c denotes the number of totally utilized descriptors. Then, constant and near constant columns from this matrix was deleted to remove redundant information. Collinear columns in D were also removed after calculating the correlation of the descriptors with the R_F vector and with other descriptors. Finally, among a detected pair of collinear columns, the one with the lowest correlation with the R_F vector was eliminated from the D matrix. After these refining process, 404 descriptors were retained in D (size = 21×404) for further process and variable selection. In the current study, the structures of natural AAs were drawn using Hyperchem software (version 7, Hypercube Inc., http://www.hyper.com, USA) and the AM1 semi-empirical method were applied during optimization. Different categories of the structural features were extracted using DRAGON (http://michem.disat.unimib.it/chm/; Milano Chemometrics and QSAR research group) for all AAs.

In the next step, the constructed data matrix (D) was divided into test and training subsets and the training set was targeted by variable selection and further model development. Stepwise multiple linear regression (SMLR) was applied as the variable selection method and the squared correlation coefficient of training set (R^2_{train}) and cross validation (Q^2_{CV}) were the criteria for choosing the final model.[15-17] In addition to cross validation, different statistical approaches, such as *y*-scrambling and prediction of a small portion of AAs, as the external test set, were utilized to evaluate the prediction ability and stability of the suggested QSRR model in RP-TLC.[18,19]

All statistical and calculations tasks were carried out *via* MATLAB software (version 7.7, R2008b, Math work, Inc., http://mathworks.com, USA). A personal computer under the Windows 7 operating system was used to run all software.

RESULTS AND DISCUSSION

After splitting the data into training and test sets of samples using random selection from PCA space (Fig. 1a) and variable selection using stepwise MLR, different models were constructed based on 1 to 8 descriptors of the AAs and the results of fitting and cross validation is represented in Fig. 1b. As can be observed in Fig. 1b, a QSRR containing 5 descriptors was utilized as the optimum one, after auto scaling the X-matrix (descriptors) and *y*-vector (RTLC retardation factor):

$$R_{F(\text{ethanol-sodium azide})} = -2.34\ (\pm 0.584) - 0.19\ (\pm 0.003)\ G_{(N..O)} - \\ -1.594\ (\pm 0.211)\ \text{Mor24u+}\ 6.661\ (\pm 1.080)\ \text{PW2} + \\ 1.018\ (\pm 0.200)\ \text{Mor28u} - 0.619\ (\pm 0.158)\ \text{SEige} \quad (1)$$

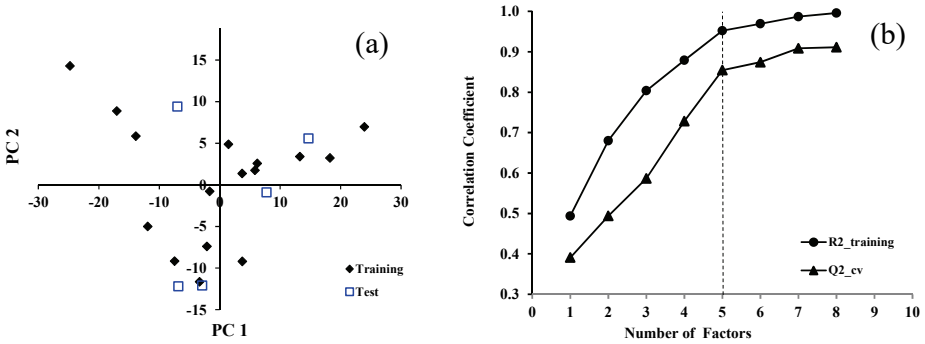

Fig. 1. Two dimensional-PCA plot of the space of the total descriptors in AA chromatographic samples (a) and correlation coefficient of the training set (R^2_{train}) and cross-validation (Q^2) *vs.* the number of descriptors to select the optimum number of factors (b) for the suggested RP-TLC model in ethanol–sodium azide solution.

In the above suggested QSRR in ethanol–sodium azide solution $G_{(N..O)}$ denotes the sum of geometrical distances between the nitrogen and oxygen atoms in the AA structure. Mor24u is the unweighted three dimensional molecular representation of structures based on electronic diffraction (3D-MoRSE) descriptors of signal 24, PW2 denotes the path/walk 2-Ranic shape index, Mor28u corres-

ponds to the unweighted 3D-MoRSE information of signal 28 and SEige is the sum of the Eigenvalue from the electronegativity weighted distance matrix.[14] The definitions and categories of the utilized descriptors are also summarized in Table II.

TABLE II. Class and definition of descriptors used in model 1 and 2

No.	Name	Class	Definition
1	$G_{(N\cdot\cdot O)}$	3D Atom pairs	Sum of geometrical distances between N··O
2	Mor24u	3D-MoRSE descriptors	3D-MoRSE descriptors signal 24 / unweighted
3	PW2	Topological indices	Path/walk 2 - Randic shape index
4	Mor28u	3D-MoRSE descriptors	3D-MoRSE descriptors signal 28 / unweighted
5	SEige	Eigenvalue-based indices	Sum of the eigenvalue from the electronegativity weighted distance matrix

To obtain a better prediction of the R_F values, all five included descriptors and experimental vector of R_F were targeted by mean-centering and scaling (autoscaled).[12,20] After these pre-treatments, the linear model was re-computed based on these prepared data and Eqs. (2) containing standardized MLR-coefficients were obtained:

$$R_{F(\text{ethanol-sodium azide})} = -0.72\ (\pm 0.098)\ G_{(N..O)} - 0.540\ (\pm 0.072)\ \text{Mor24u} + \\ + 0.461\ (\pm 0.075)\ \text{PW2} + 0.457\ (\pm 0.090)\ \text{Mor28u} - \\ - 0.410\ (\pm 0.105)\ \text{SEige} \qquad (2)$$

$$R^2_{\text{train}} = 0.95,\ F = 39.85,\ RMSE_{\text{train}} = 0.22,\ F_{\text{crit}(95\ \%)} = 3.33$$

As shown in the above results, the significantly higher value of F-statistic in comparison to F_{crit} confirms the significance of the above QSRR developed in ethanol–sodium azide solution. In addition to R^2_{train} of model 2, which was equal to 0.95, Q^2_{LOO} of cross validation was equal to 0.85 that shows suitable fitness and sufficient stability of model 2.[21] In Eqs. (1) and (2), the standard 3of the five descriptors are included because they have a very low value compared to the calculated coefficients. Magnitude of the coefficient of each descriptor of AAs can be used to conclude about the effect of that descriptor on R_F of natural AAs in the studied mobile phase (ethanol–sodium azide solution).

Details and explanation of all structural descriptors in the suggested models will be presented in the next sections. The numerical values of $G_{(N\cdot\cdot O)}$, Mor24u, PW2, Mor28u and SEige are given in the Supplementary material to this paper (Table S-I).

In this model, the $RMSE_{test}$ and R^2_{test} values were 0.26 and 0.94, respectively. Thus, the results showed good agreement between predicted and experimental R_F values for the 21 AAs in the training and test samples. Y-scrambling was applied and the Q^2_{MP} value of this test was 0.25, which confirms that a chance QSRR model in ethanol–sodium azide was not constructed. The predicted values of retardation factor of the 21 free amino acids using the model are pre-

sented in Table I and the statistical parameters of this QSRR model are given in Table III. As was shown in the Fig. 2a, a suitable correlation between experimental and predicted R_F values of the amino acids was obtained. In addition to the denoted statistics, some other criteria suggested by Golbraikh and Tropsha were calculated for the developed QSRR model.[21,22] Some of the important and well-known metrics were calculated for the suggested model are denoted in the following and their threshold values for a valid model are also mentioned in Eqs. (3)–(5):

$$|R_0^2 - R'_0{}^2| = 0.00597 \text{ (Threshold value} < 0.3\text{, Passed!)} \quad (3)$$

$$k = 1.00073 \text{ and } (|R_0^2 - R'_0{}^2|/R^2) = 0.00094$$

$$\text{(Threshold value: } [0.85<k<1.15 \text{ and } |R_0^2 - R'_0{}^2| / R^2 <0.1]\text{, Passed!)} \quad (4)$$

$$k' = 0.99132 \text{ and } (|R'_0{}^2 - R_0^2|/R^2) = 0.00766$$

$$\text{(Threshold value: } [0.85< k' <1.15 \text{ and } |R'_0{}^2 - R_0^2|/R^2 < 0.1]\text{, Passed!)} \quad (5)$$

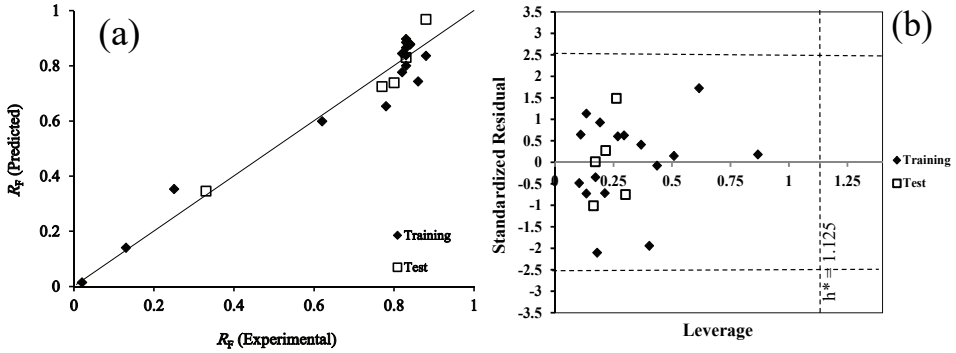

Fig. 2. Plot of predicted R_F *vs*. experimental values for the 21 investigated AA samples using the five parametric RP-TLC model in ethanol –sodium azide (a). The applicability domain of the set of AAs shown by the Williams plot (b). The cut off values of the standardized residual (±2.5 times the standards deviation) and the leverage (h^*) are illustrated by horizontal and vertical dashed lines, respectively. All samples are located within the applicability domain.

Details of the calculation of these parameters can be found in the original references[21] but, as can be seen, the constructed QSRR passed these validation criteria. Other criteria were also suggested by Roy *et al.* to show the prediction ability known as the average r^2_m or r^2_m and delta r^2_m or Δr^2_m.[22] r^2_m should be higher than 0.5 and Δr^2_m must be lower than 0.2 in a valid method.[23] For the suggested QSRR shown in Eq. (2), r^2_m and Δr^2_m of test set were 0.845 and 0.0402, respectively, which indicate the validity of the agreement between the predicted and actual solubility in the test set. However, it is noteworthy that the small number of AAs in test set is a limitation but this was because of the limited amount of experimental data.

TABLE III. Statistical performance of the proposed QSRR of the RP-TLC samples of amino acids (in ethanol–sodium azide) using three different random-divided test and training sets

Training-test set	N_{train}[a]	N_{test}[b]	R^2_{train}[c]	$RMSE_{train}$[d]	Q^2_{LOO}[e]	$RMSE_{cv}$[f]	R^2_{test}[g]	$RMSE_P$[h]	Q^2_{MP}[i]
1[j]	16	5	0.95	0.22	0.85	0.35	0.94	0.26	0.25
2[k]	16	5	0.94	0.23	0.84	0.40	0.91	0.35	0.31
3[l]	16	5	0.95	0.23	0.84	0.41	0.91	0.33	0.16

[a]Number of RP-TLC runs in the training set; [b]number of RP-TLC runs in test set; [cc]orrelation coefficient of the training RP-TLC runs; [d]root mean square error of the training RP-TLC runs (Calibration); [e]correlation coefficient of leave-one-out cross-validation; [f]root-mean-square errors of leave-one-out cross-validation; [g]correlation coefficient of the test RP-TLC runs; [h]root-mean-square errors of the test RP-TLC runs; [i]maximum cross--validation correlation coefficient for 30 Y-randomization tests; [j]number of solvents in the test set as indicated in Table I: AA9, AA14, AA18, AA20, AA21; [k]number of solvents in the test set: AA2, AA10, AA12, AA18, AA20; [l]number of solvents in the test set: AA1, AA2, AA12, AA16, AA18

Another important point should be considered in the evaluation of the QSRR is its independency from the AAs that were used as the training set or reserved as the test set. To ensure about this independency, two other subsets of TLC runs were randomly chosen from the RP-TLC samples as the training sets and two rest subsets (containing 5 AAs) as the test sets, which is shown in the results as train--test 2 and train-test 3. As presented in Table III, changing the AAs in the training or test set had no effect on the goodness-of-fit or prediction of the QSRR model for the RP-TLC using ethanol–sodium azide.

Applicability domain and pair/multi correlation

As a well-known recommendation, the suggested QSRR model must exclude any linear dependency between the AAs descriptors. This necessity is because this seriously limits the accuracy in models with collinearity and cannot be useful to justify the chromatographic behavior of analytes in RP-TLC during elution with ethanol–sodium azide. Moreover, the presentation of collinear descriptors led to wrong signs being obtained for the coefficients of the QSRR.[16,24] The correlation between each pair of descriptors in the five utilized AAs descriptors was done and the matrix of pair correlation for the present QSRR model is given in Table IV, which indicates no high correlation in this model.

TABLE IV. Pair correlation matrix for descriptors in the developed QSRR model for ethanol–sodium azide and the related VIF values as an index of multi-collinearity

	$G_{(N\cdot\cdot O)}$	Mor24u	PW2	Mor28u	SEige	*VIF*
$G_{(N\cdot\cdot O)}$	1.00					2.03
Mor24u	0.00	1.00				1.07
PW2	0.00	0.05	1.00			1.17
Mor28u	0.35	0.00	0.00	1.00		1.68
SEige	0.45	0.00	0.03	0.42	1.00	2.30

Not only the existence of pair-correlation, but also multi-collinearity (*i.e.*, collinearity of one with all others) in QSRRs is also a risk for model accuracy and the variance inflation factor (*VIF*) is a good metrics to evaluate such collinearity.[25] The high multi-collinearity can hide some of structural information because of overlapping in independent variables.[25] As could be observed in Table IV, the calculated *VIF* of all utilized descriptors ($G_{(N..O)}$, Mor24u, PW2, Mor28u and SEige) are lower than critical value of 5.0,[25] which shows that the present QSRR does not suffer from risk of multi-collinearity. Thus, the sign of coefficient and their magnitude in suggested QSRR could be trusted to justify the effect of the selected structural properties of the AAs on their R_F value.

After the different statistical evaluations of the QSRR, the leverage and standardized residual for the AAs samples were calculated to represent the applicability domain (AD).[26] Considering AD can clarify the limitations and potential of the developed QSRR for these AAs, it might be useful for RP-TLC of similar structures derived from AAs.[19] AA samples with a leverage below the cut-off value and with standardized a residual within the logical range can be considered to be in the normal AD. A standardized residual higher than -3σ or lower than $+3\sigma$ is a suitable value.[27,28] In addition, the cut-off value of the leverage is $h^* = = 3(d+1)/n_{train}$,[27] where d denotes number of descriptors in the QSRR model (here equal to 5) and n_{train} shows the number of AAs in the training subset (here equal to 16). Accordingly, the h^* of the present QSRR was calculated equal to be 1.125.

According to Fig. 2b that is the Williams plot for the representation of both standardized residual and leverage, all the studied chromatographic samples were within the AD of model suggested for RP-TLC using ethanol–sodium azide.

Interpretation of model

In this model, $G_{(N..O)}$ was the first descriptor with a negative effect on the R_F of AAs in ethanol–sodium azide, which confirmed the importance of "sum of geometrical distances between N and O" ($G_{(N..O)}$). It should be emphasized that the effect of $G_{(N..O)}$ was also illustrated in previous research,[12] which was significant in the separation of amino acids in normal phase TLC (NP-TLC) with a negative effect on the R_F of amino acids.

Two unweighted 3D-MoRSE descriptors, named Mor24u and Mor28u (signals 26 and 24),[14] are imported in the model with negative and positive sign of the coefficients. The presence of 3D-MoRSE indices in this model and previous work on this subject show the potential of this category of descriptors in prediction of the retardation factors of amino acids in RP-TLC.[13] On the other hand, different signs of these two 3D-MoRSE descriptors indicate their complex contribution in the retardation of samples using ethanol–sodium azide. The other descriptor in model is *PW*2, which is categorized in topological indices and shows

path/walk 2 – Randic shape index of the amino acids.[14] The positive contribution of *PW*2 in the model illustrates the direct relationship of *PW*2 and R_F of amino acids during separation with RP-TLC using ethanol–sodium azide. SEige is the last parameter in model, which is an eigenvalue-based index with a negative sign. SEige denotes the eigenvalue sum from electronegativity weighted distance matrix[14] and thus, increasing this index in amino acids could enhance their retardation factor in the ethanol–sodium azide system.

CONCLUSIONS

QSRR as a basic field in chromatography is a tool for showing the effect of the molecular structure of analytes on their chromatographic behavior. On the other hand, because of the effect of other parameters such as stationary and mobile phase in separation, this work was focused on modeling the R_F of protein AAs in RP-TLC during elution with ethanol–sodium azide.

One of findings in this study was the impact of the sum of the geometrical distances between N and O on R_F value of AAs in RP-TLC using ethanol––sodium azide. It was found that decreasing the sum of this distance could increase the remaining AAs on the TLC plate and their R_F value in ethanol–sodium azide. This fact was in accordance with previous report on the normal phase TLC of AAs. Eigenvalue sum from electronegativity weighted distance matrix and two 3D-MoRSE properties from AAs also had an important effect on the R_F value in the investigated system.

Moreover, different statistical evaluation on training, cross validation, prediction, *y*-randomization and applicability domain confirmed the stability and accuracy of the suggested QSRR. However, the small number of compounds in training and test sets could be considered a limitation of this work but it is noteworthy that the goal of the current modeling was not only external prediction but also was the chemical/structural description of the chromatographic behavior of AAs. This work could give more information for explaining the separation of AAs, in continuation of previous studies on other mobile phases and could be completed with more studies in future.

SUPPLEMENTARY MATERIAL

Numerical vales of original descriptor used in model Eq. (1) are available electronically at the pages of journal website: https://www.shd-pub.org.rs/index.php/JSCS/index, or from the corresponding author on request.

Acknowledgment. Support of Shiraz University of Medical Sciences (Grant No. 99-01--04-23865) is gratefully acknowledged.

И З В О Д

ПРЕТСКАЗИВАЊЕ ФАКТОРА ЗАДРЖАВАЊА ПРОТЕИНСКИХ АМИНО КИСЕЛИНА У РЕВЕРСНО-ФАЗНОЈ ТАНКОСЛОЈНОЈ ХРОМАТОГРАФИЈИ СА ЕТАНОЛ–НАТРИЈУМ--АЗИДОМ КАО МОБИЛНОМ ФАЗОМ КОРИШЋЕЊЕМ КВАНТИТАТИВНЕ РЕЛАЦИЈЕ СТРУКТУРЕ И ЗАОСТАЈАЊА (QSRR)

SUSAN TORABI[1], FATEMEH HONARASA[2] и SAEED YOUSEFINEJAD3

[1]Deputy of Food and Drug Control, Shiraz University of Medical Sciences, Shiraz, Iran, [2]Department of Chemistry, Shiraz Branch, Islamic Azad University, Shiraz, Iran и [3]Research Center for Health Sciences, Institute of Health, Department of Occupational Health Engineering, School of Health, Shiraz University of Medical Sciences, Shiraz, Iran

Због значаја аминокиселина као основних јединица протеина и њихове примене у индустрији лекова и хране, постоји велико занимање за њихово раздвајање и идентификацију коришћењем простих и јефтиних приступа. Примена предиктивних модела за одређивање понашања АК може скратити експерименте покушаја-и-грешке. Овде су фактори заостајања (R_F) 21 протеинске амино киселине проучавани користећи квантитативни структура-фактор заостајања (QSRR) модел. R_F аминокиселина у раствору етанола–натријум-азида као мобилне фазе танкослојне реверсно-фазне хроматографије (RP-TLC) су корелисани са структурним особинама аминокиселина. Сугерисани QSRR указује на изврсно фитовање и способност предвиђања ($R_{2train} = 0{,}95$ и $R_{2test} = 0{,}94$). Надаље, остали статистички тестови као што су „*y*-scrambling“, унакрсна валидација, Williams график, потврђују стабилност, одсуство случајности, односно погодан домен применљивости. Показано је да је збир геометријских удаљености атома кисеоника и азота у аминокиселинама значајан фактор за RF вредности аминокиселина у етанол––натријум-азиду.

(Примљено 11. јуна, ревидирано 30. августа, прихваћено 6. октобра 2020)

REFERENCES

1. S. H. Park, M. De Pra, P. R. Haddad, S. Grosse, C. A. Pohl, F. Steiner, *J. Chromatogr., A* **1609** (2020) 460508 (https://dx.doi.org/10.1016/j.chroma.2019.460508)
2. A. M. Ramezani, S. Yousefinejad, A. Shahsavar, A. Mohajeri, G. Absalan, *J. Chromatogr., A* **1599** (2019) 46 (https://dx.doi.org/10.1016/j.chroma.2019.03.063)
3. J. M. Sutter, T. A. Peterson, P. C. Jurs, *Anal. Chim. Acta* **342** (1997) 113 (https://dx.doi.org/10.1016/S0003-2670(96)00578-8)
4. Y. Marrero-Ponce, S. J. Barigye, M. E. Jorge-Rodríguez, T. Tran-Thi-Thu, *Chem. Pap.* **72** (2018) 57 (https://dx.doi.org/10.1007/s11696-017-0257-x)
5. C. Giaginis, A. Tsantili-Kakoulidou, *Chromatographia* **76** (2013) 211 (https://dx.doi.org/10.1007/s10337-012-2374-6)
6. J. Dai, L. Jin, S. Yao, L. Wang, *Chemosphere* **42** (2001) 899 (https://dx.doi.org/10.1016/S0045-6535(00)00181-8)
7. K. Héberger, *J. Chromatogr., A* **1158** (2007) 273 (https://dx.doi.org/10.1016/J.CHROMA.2007.03.108)
8. R. Kaliszan, *Chem. Rev.* **107** (2007) 3212 (https://dx.doi.org/10.1021/cr068412z)
9. R. Kaliszan, *J. Chromatogr., A* **220** (1981) 71 (https://dx.doi.org/10.1016/S0021-9673(00)98504-2)
10. D. Kaźmierczak, W. Ciesielski, R. Zakrzewski, *JPC - J. Planar Chromatogr. - Mod. TLC* **18** (2005) 427 (https://dx.doi.org/10.1556/JPC.18.2005.6.5)
11. T. Hudaib, S. Brown, D. Wilson, P. E. Eady, *JPC - J. Planar Chromatogr. - Mod. TLC* **29** (2016) 145 (https://dx.doi.org/10.1556/1006.2016.29.2.9)

12. S. Yousefinejad, F. Honarasa, N. Saeed, *J. Sep. Sci.* **38** (2015) 1771 (https://dx.doi.org/10.1002/jssc.201401427)
13. S. Yousefinejad, F. Honarasa, S. Akbari, M. Nekoeinia, *J. Liq. Chromatogr. Relat. Technol.* **43** (2020) 580 (https://dx.doi.org/10.1080/10826076.2020.1774388)
14. R. Todeschini, V. Consonni, *Molecular Descriptors for Chemoinformatics*, 2nd ed., Wiley-VCH, Weinheim, 2009 (ISBN: 9783527318520)
15. P. Gramatica, *Mol. Inform.* **33** (2014) 311 (https://dx.doi.org/10.1002/minf.201400030)
16. S. Yousefinejad, B. Hemmateenejad, *Chemom. Intell. Lab. Syst.* **149** (2015) 177 (https://dx.doi.org/10.1016/j.chemolab.2015.06.016)
17. S. Yousefinejad, F. Honarasa, A. Solhjoo, *J. Chem. Eng. Data* **61** (2016) 614 (https://dx.doi.org/10.1021/acs.jced.5b00768)
18. J. U. N. Shao, *J. Am. Stat. Assoc.* **88** (1993) 486 (https://dx.doi.org/10.2307/2290328)
19. P. Gemperline, *Practical Guide to Chemometrics*, 2nd ed., Taylor & Francis Group, Boca Raton, USA, 2006 (ISBN: 1574447831)
20. F. Honarasa, S. Yousefinejad, S. Nasr, M. Nekoeina, *J. Mol. Liq.* **212** (2015) 52 (https://dx.doi.org/10.1016/j.molliq.2015.08.055)
21. A. Golbraikh, A. Tropsha, *Mol. Divers.* **5** (2000) 231 (https://dx.doi.org/10.1023/A:1021372108686)
22. K. Roy, R. N. Das, P. Ambure, R. B. Aher, *Chemom. Intell. Lab. Syst.* **152** (2016) 18 (https://dx.doi.org/10.1016/j.chemolab.2016.01.008)
23. K. Roy, P. Chakraborty, I. Mitra, P. K. Ojha, S. Kar, R. N. Das, *J. Comput. Chem.* **34** (2013) 1071 (https://dx.doi.org/10.1002/jcc.23231)
24. L. Eriksson, J. Jaworska, A. P. Worth, M. T. D. Cronin, R. M. McDowell, P. Gramatica, *Environ. Health Perspect.* **111** (2003) 1361 (https://dx.doi.org/10.1289/ehp.5758)
25. T. A. Craney, J. G. Surles, *Qual. Eng.* **14** (2002) 391 (https://dx.doi.org/10.1081/QEN-120001878)
26. R. Todeschini, V. Consonni, P. Gramatica, in *Comprehensive Chemometrics: Chemical and Biochemical Data Analysis*, R. Tauler, B. Walczak, S. D. Brown (Eds.), Elsevier B.V., Amsterdam, 2009, pp. 129–172 (ISBN: 9780444641663)
27. T. I. Netzeva, A. P. Worth, T. Aldenberg, R. Benigni, M. T. D. Cronin, P. Gramatica, J. S. Jaworska, S. Kahn, G. Klopman, C. A. Marchant, G. Myatt, N. Nikolova-Jeliazkova, G. Y. Patlewicz, R. Perkins, D. W. Roberts, T. W. Schultz, D. T. Stanton, J. J. M. van de Sandt, W. Tong, G. Veith, C. Yang, *Altern. to Lab. Anim.* **33** (2005) 155 (https://dx.doi.org/10.1177/026119290503300209)
28. S. Yousefinejad, R. Eftekhari, F. Honarasa, Z. Zamanian, F. Sedaghati, *J. Mol. Liq.* **241** (2017) 861 (https://dx.doi.org/10.1016/j.molliq.2017.06.081).

Journal of the Serbian Chemical Society
JSCS-info@shd.org.rs • www.shd.org.rs/JSCS
J. Serb. Chem. Soc. 86 (4) S89 (2021)
Supplementary material

SUPPLEMENTARY MATERIAL TO

Prediction of retardation factor of protein amino acids in reversed phase TLC with ethanol–sodium azide solution as the mobile phase using QSRR

SUSAN TORABI[1], FATEMEH HONARASA[2] and SAEED YOUSEFINEJAD[3]*

[1]*Deputy of Food and Drug Control, Shiraz University of Medical Sciences, Shiraz, Iran,* [2]*Department of Chemistry, Shiraz Branch, Islamic Azad University, Shiraz, Iran and* [3]*Research Center for Health Sciences, Institute of Health, Department of Occupational Health Engineering, School of Health, Shiraz University of Medical Sciences, Shiraz, Iran*

J. Serb. Chem. Soc. 86 (4) (2021) 381–391

TABLE S-I. Numerical values of the original descriptor used in Eq. (1) (before auto scaling)

Code	Name	$G_{(N\cdot\cdot O)}$	Mor24u	PW2	Mor28u	SEige
AA 1	Glycine-III	6.5	–0.105	0.517	0.092	0.637
AA 2	Alanine-III	6.52	0.06	0.578	–0.115	0.637
AA 3	Aspartic acid-III	15.5	0.095	0.572	0.03	1.134
AA 4	Arginine-III	48.96	–0.125	0.557	0.142	1.058
AA 5	Proline-III	6.43	0.034	0.563	–0.18	0.637
AA 6	Hydroxyproline-III	10.15	–0.172	0.581	–0.181	0.886
AA 7	Lysine-III	20.33	0.09	0.533	–0.183	0.778
AA 8	Glutamic acid-III	17.94	–0.135	0.568	0.124	1.134
AA 9	Serine-III	10.26	–0.135	0.557	–0.017	0.886
AA 10	Tryptophan-III	16.85	–0.024	0.582	0.09	0.778
AA 11	Valine-III	6.47	–0.032	0.588	–0.219	0.637
AA 12	Phenyl alanine-III	6.53	–0.056	0.564	–0.086	0.637
AA 13	Isoleucine-III	6.47	–0.013	0.571	–0.126	0.637
AA 14	Leucine-III	6.56	–0.142	0.572	–0.228	0.637
AA 15	Asparagine-III	20.62	–0.111	0.572	–0.023	1.026
AA 16	Methionine-III	6.48	–0.253	0.537	–0.233	0.709
AA 17	Cysteine-III	6.57	–0.092	0.557	–0.071	0.709
AA 18	Histidine-III	25.23	0.038	0.57	0.028	0.918
AA 19	Threonine-III	14.31	–0.052	0.579	0.021	0.886
AA 20	Tyrosine-III	10.26	0.018	0.588	–0.002	0.886
AA 21	Glutamine-III	4.22	0.018	0.568	–0.282	0.637

* Corresponding author. E-mail: yousefisa@sums.ac.ir

Journal of the Serbian Chemical Society
JSCS-info@shd.org.rs • www.shd.org.rs/JSCS
J. Serb. Chem. Soc. *86* (4) 393–406 (2021)
JSCS–5429
Original scientific paper

Structural study of Pt(II) and Pd(II) complexes with quinoline-2-carboxaldehyde thiosemicarbazone

PREDRAG G. RISTIĆ[1], MARKO V. RODIĆ[2#], NENAD R. FILIPOVIĆ[3#], DRAGANA M. MITIĆ[4#], KATARINA K. ANĐELKOVIĆ[1#] and TAMARA R. TODOROVIĆ[1]*

[1]University of Belgrade – Faculty of Chemistry, Studentski trg 12–16, 11000 Belgrade, Serbia, [2]Faculty of Sciences, University of Novi Sad, Trg Dositeja Obradovića 3, 21000 Novi Sad, Serbia, [3]University of Belgrade – Faculty of Agriculture, Nemanjina 6, 11000 Belgrade, Serbia and [4]Innovation Centre of Faculty of Chemistry, University of Belgrade, Studentski trg 12–16, 11000 Belgrade, Serbia

(Received 26 November, revised 1 December, accepted 2 December 2020)

Abstract: Two square–planar complexes, [PtLCl] (**1**) and [PdLCl] (**2**), were synthesized with quinoline-2-carboxaldehyde thiosemicarbazone ligand (HL), and characterized by IR and NMR spectroscopy and single crystal X-ray diffraction analysis. In both complexes, L^- is coordinated tridentately *via* the same donor atom set, while the fourth coordination site is occupied by a chloride ion. However, the complexes are not isostructural due to different types of non-covalent intermolecular interactions. These interactions were analyzed using Hirshfeld surfaces and two-dimensional fingerprint plots.

Keywords: single crystal X-ray diffraction; non-covalent interactions; *N*-heteroaromatic Schiff base; chelate complexes.

INTRODUCTION

During the last decades, thiosemicarbazones have been developed as organic compounds with very diverse pharmacological applications. They show a broad range of biological activity, such as antituberculosis, antiviral, antimalarial and anticancer.[1,2] It is assumed that the strong metal-chelating/-interacting properties of thiosemicarbazones and their interference with the cellular iron and copper homeostasis play an important role in their biological activity.[1]

Thiosemicarbazones are well known ligands that coordinate to various metal ions in different modes. In general, a bidentate binding mode *via* N,S donor atom set is the most common one.[3,4] However, the chelating capacity of thiosemicarbazones can be enhanced when additional suitable donor atoms are present in the

* Corresponding author. E-mail: tamarat@chem.bg.ac.rs
# Serbian Chemical Society member.
https://doi.org/10.2298/JSC201126079R

molecule, as in the case of *α*-*N*-heterocyclic thiosemicarbazones.[3,4] As thiosemicarbazones exist as thione–thiol tautomers, they can bind to a metal center in the neutral or anionic forms. An overview on the observed bonding modes for this class of ligands is given in several reviews in literature covering this field.[3–5]

Thiosemicarbazone complexes have shown potent biological activity, such as anticancer, antibacterial, antifungal, and antiviral, owing to their property to diffuse through the semi permeable membrane of cell lines.[2,4–6] The enhanced effect of the complexes in comparison to free ligands may be attributed to their increased lipophilicity. Namely, upon coordination to the metal ion, the ligand orient with the lipophilic and aromatic parts outwards, exposing the hydrophobic part to the exterior.[3] This allows the complex to enter the cell and could explain the reason why complexes are more active than the parent ligands.

One line of previous research was focused on the synthesis, characterization and biological activity evaluation of d-metal complexes with *α*-*N*-heterocyclic chalcogensemicarbazones, predominantly derivatives of 2-formylpyridine and quinoline-2-carboxaldehyde.[7–14] Taking into account that many properties of chemical systems are defined not only by the molecular structure but also by weak intermolecular interactions,[15,16] herein the synthesis and characterization of Pd(II) and Pt(II) complexes with quinoline-2-carboxaldehyde thiosemicarbazone, with the main focus on the solid state structures and main interactions that govern the crystal packing, are reported. Both chosen ions have a d^8 electronic configuration and almost the same ionic radii; thus, their complexes with the same ligand systems are often isostructural. However, the higher basicity of the 5d Pt(II) ion and its extended electronic density in comparison to the 4d Pd(II) ion can often result in stronger M···H−X (X = C, N, O, S) interactions for Pt(II).[17] These effects can lead to a difference in the molecular structure and especially packing features of the complexes.[18]

EXPERIMENTAL

Materials and methods

Thiosemicarbazide (97 %), and quinolone-2-carboxaldehyde (97 %) were obtained from Acros Organics (BVBA, Geel, Belgium), while potassium tetrachloroplatinate(II) (98 %), and potassium tetrachloropalladate(II) (98 %) were obtained from Aldrich (Sigma–Aldrich). All solvents (reagent grade) were obtained from commercial suppliers and used without further purification.

Elemental analyses (C, H, N, S) were performed by the standard micromethods using an Elementar Vario ELIII C,H,N,S/O analyzer, and the results were found to be in good agreement (±0.4 %) with the calculated values. The IR spectra were recorded on a Thermo Scientific Nicolet 6700 FT-IR spectrophotometer by the attenuated total reflection (ATR) technique in the region 4000–400 cm^{-1}. Abbreviations used for IR spectra: *vs*, very strong; *s*, strong; *m*, medium; *w*, weak; *vw*, very weak. Molar conductivities were measured at room temperature (298 K) on the Crison multimeter MM41. The NMR spectra were obtained on a Bruker Avance 500 instrument equipped with a broadband direct probe. All spectra were measured at

298 K in DMSO-d_6. Chemical shifts are given on the δ scale (ppm) relative to tetramethylsilane (TMS) as the internal standard for ^{1}H and ^{13}C.

Synthesis of quinoline-2-carboxaldehyde thiosemicarbazone (HL)

The ligand was synthesized, as described previously[19] in the condensation reaction of quinoline-2-carboxaldehyde (0.862 g, 5.5 mmol) and thiosemisemicarbazide (0.500 g, 5.5 mmol) in ethanol (EtOH, 50 mL). The purity of the ligand was checked by elemental analysis and NMR spectroscopy.

Synthesis of quinoline-2-carboxaldehyde thiosemicarbazonato-N,N,S-*chloridoplatinum(II), [PtLCl] (**1**)*

Into a suspension of HL (0.100 g, 0.44 mmol) in EtOH (10 mL), a solution of $K_2[PtCl_4]$ (0.180 g, 0.43 mmol) in 1 mL of water was added. The reaction mixture was refluxed for 1 h. After cooling to room temperature, the obtained dark red microcrystals were separated by filtration and washed with cold EtOH. Single crystals of **1** suitable for X-ray diffraction analysis were obtained by slow diffusion of EtOH vapor into DMSO solution of microcrystals. Single crystals of **1** were separated by filtration and washed with cold EtOH.

Synthesis of quinoline-2-carboxaldehyde thiosemicarbazonato-N,N,S-*chloridopalladium(II), [PdLCl] (**2**)*

Into a suspension of HL (0.050 g, 0.22 mmol) in EtOH (10 mL), a solution of $K_2[PdCl_4]$ (0.068 g, 0.21 mmol) in 1 mL of water was added. The reaction mixture was refluxed for 1 h. After cooling to room temperature, the obtained orange microcrystals were separated by filtration and washed with cold EtOH. Single crystals of **2** suitable for X-ray diffraction analysis were obtained by slow diffusion of EtOH vapor into a DMSO solution of microcrystals. Single crystals of **2** were separated by filtration and washed with cold EtOH.

IR and NMR spectral data and spectra of HL, **1** and **2** are given in Figs. S-1–S-9 of the Supplementary material to this paper.

X-Ray crystallography

Diffraction data were collected on a Gemini S diffractometer (Oxford Diffraction), equipped with a Mo$K\alpha$ radiation source (λ = 0.71073 Å) and a Sapphire CCD detector. Data collection strategy calculation and data reduction were performed with CrysAlisPro.[20] Structure was solved by SHELXT,[21] and refined with the SHELXL-2014.[22] The SHELXLE[23] was used as a graphical user interface for the refinement procedures. All non-hydrogen atoms were refined anisotropically. The hydrogen atoms attached to C atoms were placed at the geometrically idealized positions with C–H distances fixed to 0.93 and 0.96 Å for sp^2 and sp^3 C atoms, respectively. Their isotropic displacement parameters were set equal to 1.2 and 1.5 Ueq of the parent sp^2 and sp^3 C atoms, respectively. The hydrogen atoms attached to N atoms were located in a difference Fourier map and refined isotopically. The structures were validated with Platon[24] together with extensive use of Mercury CSD 2020.2.0[25,26] and the Cambridge Crystallographic Database (CSD).[27]

A summary of the crystallographic data for the crystal structures is given in Table I.

Hirshfeld surfaces and two-dimensional (2D) fingerprint plots

For visualization of the Hirshfeld surfaces, CIF files were used. Hirshfeld surface visualization, presentation of results as d_{norm}, shape index, and curvedness, and calculation of 2D fingerprint plots with d_e and d_i distances were generated using Crystal Explorer v.17.5.[28,29] The distance from the surface to the nearest nucleus of the atom on the outside of the surface is denoted as d_e, while the distance from the surface to the closest nucleus of the atom on the

inside of the surface is denoted as d_i. The surfaces are mapped over a standard color scale, and 2D fingerprint plots are calculated using d_e and d_i values in the range 0.4−2.8 Å.

TABLE I. Crystallographic data and refinement parameters for **1** and **2**

Compound	**1**	**2**
Chemical formula	$C_{11}H_9ClN_4PtS$	$C_{11}H_9ClN_4PdS$
M_r	459.82	371.13
Crystal system	Monoclinic	Triclinic
Space group	$P2_1/n$	$P\bar{1}$
a /Å	11.1555(3)	8.6723(8)
b / Å	7.1925(2)	8.7320(8)
c / Å	16.2149(5)	9.5468(9)
V / Å^3	1250.61	612.90
Z	4	2
D_x / Mg m^{-3}	2.442	2.011
Radiation type	Mo$K\alpha$ (λ = 0.71073 Å)	Mo$K\alpha$ (λ = 0.71073 Å)
μ / mm^{-1}	11.585	1.886
Crystal size, mm	0.75×0.11×0.06	0.42×0.16×0.05
	Data collection	
Absorption correction	Analytical	Analytical
T_{min}, T_{max}	0.059, 0.529	0.859, 0.969
Reflections collected	11576	4636
Independent reflections	2970	2749
Observed reflections [$I > 2\sigma(I)$]	2631	2463
R_{int}	0.065	0.022
Range of h, k, l	h=−14→15, k=−8→9, l=−22→18	h=−11→11, k=−11→11, l=−12→11
θ values, °	θ_{max} = 29.0, θ_{min} = 2.6	θ_{max} = 28.7, θ_{min} = 2.5
	Refinement	
$R[F^2 > 2\sigma(F^2)]$, wR	0.021, 0.043	0.028, 0.055
R[all data], wR	0.027, 0.045	0.034, 0.059
Goodness-of-fit (S)	1.078	1.064
No. of reflections	2970	2749
No. of parameters	171	171
No. of restraints	0	2
$\Delta\rho_{max}$, $\Delta\rho_{min}$ / e Å^{-3}	0.63, −0.97	0.40, −0.65
CCDC No.	2044686	2044685

RESULTS AND DISCUSSION

Synthesis and spectroscopic characterization

By direct reaction of $K_2[PtCl_4]$ or $K_2[PdCl_4]$ with the ligand HL in an equimolar ratio (1:1), the corresponding Pt(II) (**1**) and Pd(II) (**2**) complexes were obtained (Scheme 1). The mole ratio of the reacting species did not influence the composition of the products. The same products were also obtained by a template reaction of metal salts with quinoline-2-carboxaldehyde and thiosemicarbazide in an equimolar ratio (1:1:1). Both complexes are soluble at room temperature in

DMSO and DMF, but sparingly soluble at elevated temperature in EtOH. The synthesized complexes are non-electrolytes, as determined by molar conductivity measurements. Elemental analysis showed that the molecules of Pt(II) and Pd(II) complexes contain one deprotonated ligand molecule and a chloride ion. In the ^{1}H-NMR spectra of both complexes, the H–N3 proton signal (at 11.77 ppm in the ligand) is missing, indicating coordination of the ligand in the deprotonated form. The IR spectrum of the free ligand HL exhibits bands at 3393, 3265 and 3146 cm^{-1} arising from asymmetric and symmetric NH_2 stretching vibrations.[30] Coordination of azomethine nitrogen to the metal ions in both complexes is suggested by the shift of the ν(C=N) towards higher frequencies (1605 cm^{-1} in HL, 1632 cm^{-1} in **1**, 1638 cm^{-1} in **2**). As a consequence of the coordination of sulfur atom, the ν(C–S) band in the IR spectra of the complexes is shifted to lower frequencies (816 cm^{-1} in **1** and 817 cm^{-1} in **2**) with respect to the metal free ligand (840 cm^{-1}). In both complexes, coordination *via* the quinoline nitrogen atom can be assumed as ring stretching (1527, 1501 and 1451 cm^{-1}) and the in-plane (750 cm^{-1}) modes of the heterocyclic ring are shifted to higher frequencies.[30] The solid state structure of the complexes was elucidated by single crystal X-ray analysis (*vide infra*).

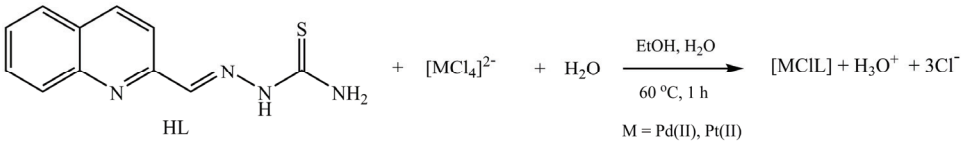

Scheme 1. Synthesis of Pt(II) and Pd(II) complexes.

*Molecular structures of **1** and **2***

Complexes **1** and **2** crystallize in the monoclinic $P2_1/n$ and triclinic $P\bar{1}$ space groups, respectively. The asymmetric unit of **1** and **2** contains the M(II) ion and one deprotonated ligand coordinated *via* sulfur atom, quinoline and imine nitrogen atoms (Fig. 1). The fourth coordination site is occupied by a chloride ligand. The overlay of the structures shows differences in the value of angles between the donor atoms of the ligand (Fig. 1). The coordination geometry around the metal centers is slightly distorted square–planar with geometric index of distortion $\tau = 0.10$ for **1** and $\tau = 0.13$ for **2**.[31] Due to the similar ionic radii of the metal ions, the lengths of coordination bonds (M–N1, M–N2, M–Cl and M–S) and corresponding bond angles are similar in both complexes (Table II).

As previously noticed for related thiosemicabazone complexes,[3–5] in **1** and **2** the C1–S1 bond is a much longer than a double bond while the adjacent C1–N3 bond is shorter than a single bond, indicating a prevalent thiolate resonance form of the coordinated ligand.

Although **1** and **2** have the same geometry, their crystal packings are different. With the exception of the nitrogen atoms, there are no classical proton donors, thus crystal packing in both complexes are based mainly on weak non-conventional interactions. An obvious limitation in the analysis of non-conventional contacts using the tools available in the CSD Mercury[25,26] is the application of distance criteria to determine the presence of a contact since interactions can extend beyond sums of van der Waals radii.[32,33] To gain further insights into the way molecules of **1** and **2** pack in their crystals, Hirshfeld surface analysis and noncovalent interaction plots (*vide infra*) were employed.

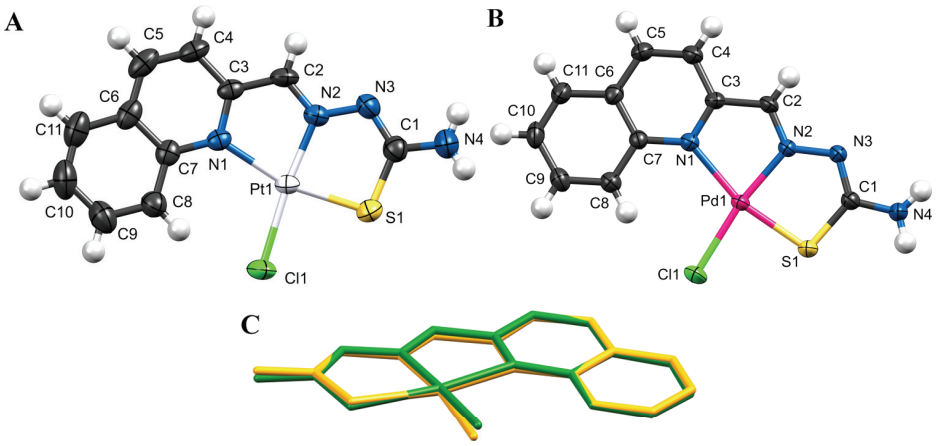

Fig. 1. Perspective view and labeling of molecular structure of **1** (A) and **2** (B). Thermal ellipsoids are shown at the 50 % probability level. Hydrogen atoms are shown as spheres of arbitrary radius. The overlay of the molecular structures of **1** (green) and **2** (yellow) (C).

TABLE II. Selected bond lengths and angles for **1** and **2**

Bond	Bond length, Å	Angle	Angle, °
Pt1–Cl1	2.3092(10)	N2–Pt1–N1	79.88(12)
Pt1–N1	2.125(3)	N2–Pt1–S1	84.93(10)
Pt1–N2	1.946(3)	N1–Pt1–Cl1	106.18(8)
Pt1–S1	2.2453(10)	S1–Pt1–Cl1	89.16(4)
Pd1–Cl1	2.3236(8)	N2–Pd1–N1	80.07(9)
Pd1–N1	2.149(2)	N2–Pd1–S1	84.18(7)
Pd1–N2	1.964(2)	N1–Pd1–Cl1	108.73(6)
Pd1–S1	2.2237(8)	S1–Pd1–Cl1	87.04(3)

Hirshfeld surface and 2D fingerprint plot analysis

The Hirshfeld surface and 2D fingerprint plot analysis represent important tools in exploring, understanding and describing crystal packing.[28,34] The Hirshfeld surfaces mapped over d_{norm} utilize the function of normalized distances d_i and d_e, where d_i and d_e are the distances from a given point on the surface to the

nearest atom inside and outside the surface, respectively. The long interatomic contacts, the contact at van der Waals separations and short interatomic contacts can be seen on the d_{norm}-mapped Hirshfeld surfaces as the blue, white and red color regions, respectively. Further chemical insight into the molecular packing can be obtained using curvedness and shape-index. Interactions can be observed in the shape-index plot as red and blue regions, as well as in the curvature plot as a flat zone in the same position of the surface as in the shape-index plot. On the shape index, red-colored regions correspond to an acceptor, while blue-colored regions belong to the donor of an intermolecular interaction.

2D Fingerprint plots, derived form a Hirshfeld surface, are a useful method to summarize complex information about intermolecular interactions in a crystal.[34] The color of each point on the plot, corresponding to the relative area of a (d_e, d_i) pair, is recognized as the contribution from different interatomic contacts: blue, green and red correspond to small, moderate and greatest contributions, respectively. An uncolored region indicates no contribution to the Hirshfeld surface.

The Hirshfeld surfaces of the complexes are depicted in Fig. 2, while the pseudosymmetric 2D fingerprint plots are depicted in Fig. 3.

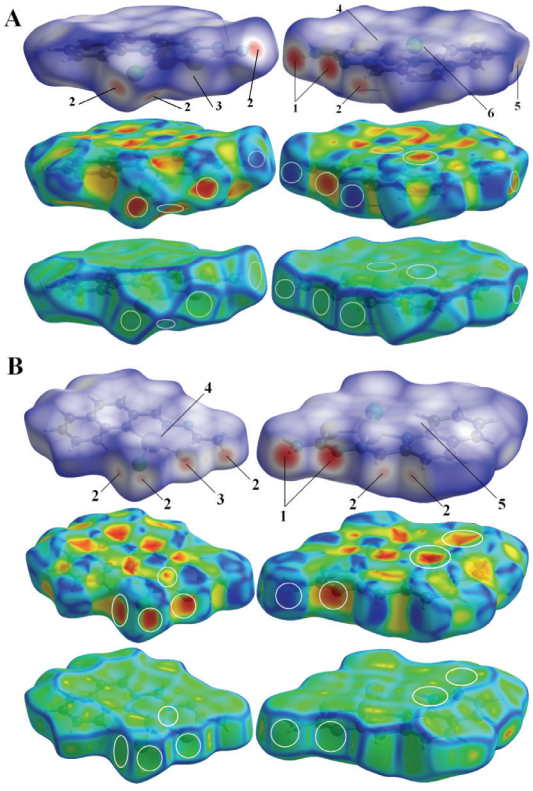

Fig. 2. Two views of the Hirshfeld surface mapped with d_{norm} (top), shape-index (middle) and curvedness (bottom), for **1** (A) and **2** (B). The numbers indicate points of contact derived from intermolecular interactions (see Table III).

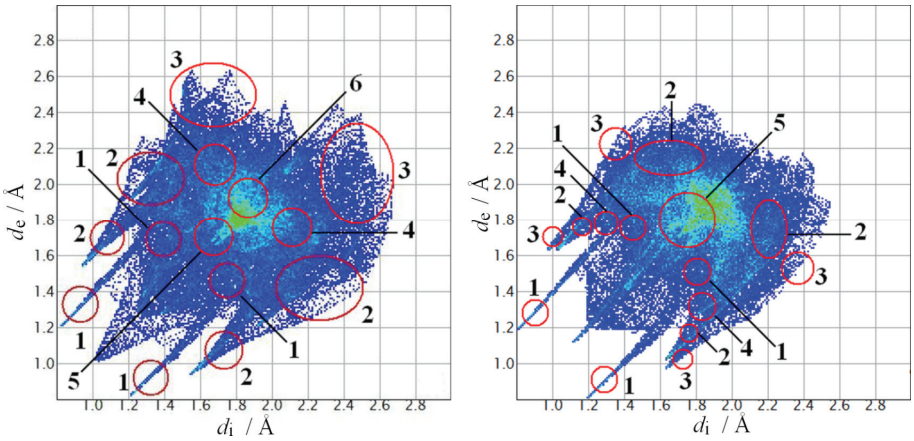

Fig. 3. Full 2D fingerprint plots for **1** (left) and **2** (right). For the interaction types see Table III.

TABLE III. Relative contributions and (d_i + d_e) of different interaction types in the crystal structures of **1** and **2**; M = Pt in **1**; M = Pd in **2**

No.	Interaction type	**1**		No.	**2**	
		Relative contribution %	(d_i +d_e) Å		Relative contribution %	(d_i +d_e) Å
1	N···H	8.6	2.0	1	9.8	2.0
2	Cl···H	16.5	2.6	2	16.8	2.7
3	S···H	11	3.1	3	8.7	2.6
4	M···H[a]	2.1	3.4	4	1.5	3.4
5	C···H	8.4	4.1	/	/	/
6	Cg···Cg	6.2	3.6	5	5.3	3.8

In the crystal structure of **1**, each molecule of the complex achieves six types of non-covalent intermolecular interactions/contacts, resulting in a three dimensional (3D) supramolecular structure. On the other hand, each molecule of **2** forms five types of intermolecular interactions. The relative percentage contributions of close contacts to the overall Hirshfeld surfaces in both crystal structures are presented in Table III.

The brightness of the red spots on the Hirshfeld surfaces mapped over d_{norm} can be qualitatively correlated with the strength of intermolecular contact, *i.e.*, as potential hydrogen bonds (bright spots), weak interactions (diminutive spots) or short (faint spots) interatomic contacts.[35] The bright-red spots indicated with '1' on the Hirshfeld surfaces mapped over d_{norm} (Fig. 2) indicate to donors and acceptors of classical hydrogen interactions involving N4 nitrogen atoms as donors and N3 nitrogen atoms as acceptors. The bright-red spots indicated with '2' on the same surfaces indicate the chlorine atom Cl1 as a double acceptor in both crystal structures. However, the corresponding donors are different. In **1**, the donors are N4 and C2 atoms, while in **2**, the donors are C2 and C4. The sulfur

atom S1 in **1** is involved in probable short interatomic contact with the C11 carbon atom, as can be seen from the faint spot indicated with '3'. In contrast, the sulfur atom S1 in **2** is an acceptor in the probable weak non-classical hydrogen bonding with the N4 nitrogen atom as donor, since the spot indicated with '3' is bright red. To examine π–π stacking in the molecular packing, an analysis of the Hirshfeld surface mapped over the shape-index and curvedness properties can be used (Fig. 2). The π–π stacking between the quinoline rings is indicated by the appearance of small blue regions surrounding bright-red spots within the rings (Fig. S-10 of the Supplementary material). The presence of these interactions is also evident as the flat regions around the rings on the Hirshfeld surface mapped over curvedness for both complexes.

The relative contributions of different types of intermolecular interactions in the crystal structures of **1** and **2** are different (Table III). This is a consequence of different symmetries of the space groups in which the complexes crystallize. The common feature for both complexes is that non-classical Cl···H interactions are most represented, probably because the chlorine atom is a double hydrogen bond acceptor. Finally, 2D fingerprint plots indicate the presence of M···H non-classical hydrogen interactions in both crystal structures (Fig. S-11 of the Supplementary material).

Analysis of crystal packing

The packing of molecules in the crystal structure of **1** is depicted in Fig. 4A. Each molecule of **1** forms a centrosymmetric dimer with a neighboring molecule *via* N4–H4B···N3^{i} (*i* = –*x*, 1–*y*, 1–*z*) hydrogen interaction (*D*···*A* = 3.039 Å, <N–H···N = 175.8°). A centrosymmetric dimer is also formed by C5–H5···Pt1^{ii} (*ii* = –1+*x*, –1+*y*, *z*) weak non-classical hydrogen interaction (*D*···*A* = 3.542 Å, <C–H···Pt = 89.9°). These two interactions are responsible for the formation of 1-D infinite chains parallel to the [110] direction (Fig. 4B). The coordinated Cl1 atom is a double acceptor involved in two non-classical hydrogen interactions, N4–H4A···Cl1^{iii} (*iii* = ½*x*, –1/2+*y*, 1.5–*z*; D···A = 3.385 Å, <N–H···Cl = 141.6°) and C2–H2···Cl1^{iv} (*iv* = –1/2+*x*, 1.5–*y*, –1/2+*z*; *D*···*A* = 3.527 Å, <C–H···Cl = 161.6°), as depicted in Fig. 4C. Sulfur atom S1 is involved in weak intermolecular contact C11–H11···S1^{v} (*v* = 1/2+*x*, 1.5–*y*, –1/2+*z*; *D*···*A* = 4.156 Å, <C–H···S = 159.7°; Fig. 4D). Finally, in the crystal packing of **1** there are π–π stacking interactions responsible for the formation of dimers (Fig. 4E) with a Cg···Cg^{vi} distance of 3.60 Å (*vi* = 1–*x*, 2–*y*, 1–*z*; Cg is the centre of gravity of the pyridine part of the ring).

The packing of molecules in the crystal structure of **2** is depicted in Fig. 5A. The same N4–H4B···N3^{i} (*i* = –*x*, 1–*y*, –*z*; *D*···*A* = 3.009 Å, N–H···N = 175.7°) interactions are responsible for the formation of centrosymmetric dimers. Each dimer unit is connected to a neighboring complex molecule by weak hydrogen

interactions involving the metal center (C11–H11···Pd1^{ii}, *ii* = 1–*x*, –*y*, 1–*z*; D···A = 3.369 Å, <C–H···Pd = 84.0°), thus forming a chain parallel to the [1–1 1] direction (Fig. 5B).

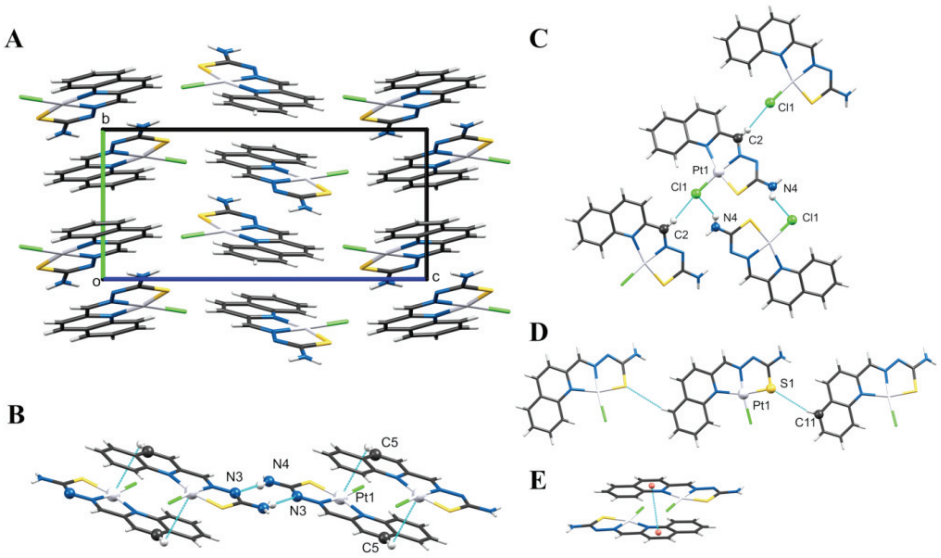

Fig. 4. Non-covalent interactions in the crystal packing of **1**. A) The packing of molecules in the crystal structure; B) a chain parallel to the [110] direction formed by C–H···Pt interactions; C) C–H···Cl and N–H···Cl interactions in the crystal structure of **1**; D) C–H···S contacts in the crystal structure of **1**; (E) π–π stacking interactions.

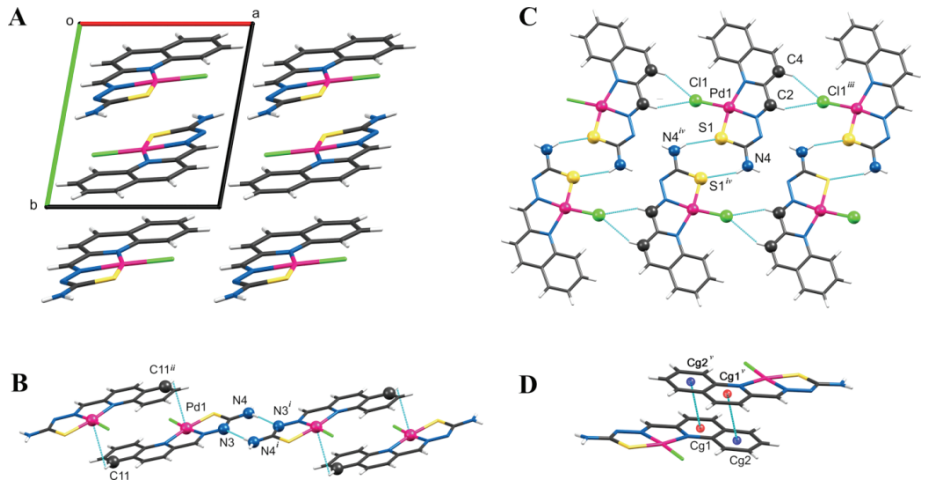

Fig. 5. Non-covalent interactions in the crystal packing of **2**. A) The packing of molecules in the crystal structure; B) a chain parallel to the [1–1 1] direction formed by C–H···Pd interactions; C) 2D plane, parallel to (021), formed by C–H···Cl and N–H···S interactions in the crystal structure of **2**; D) π–π stacking interactions.

Although the Cl1 atom is also a double acceptor in weak hydrogen interactions, as in **1**, these interactions involve carbon atoms C2 and C4 (C2–H2···Cl1^{iii}, *iii* = –1 + *x*, *y*, *z*; *D*···*A* = 3.636 Å, <C–H···Cl = 150.4° and C4–H4···Cl1^{iii}, D···A = = 3.653 Å, <C–H···Cl = 153.3°), thus a 1D infinite chain parallel to *a*-axis is formed. This chain is further connected by weak interactions involving the S1 atom from an adjacent complex molecule (N4–HA···S^{iv}, *iv* = 1–*x*, 1–*y*, –*z*; D···A = 3.542 Å, <N–H···S = 156.2°) thus a 2D plane parallel to (021) is formed (Fig. 5C). There are also π–π stacking interactions responsible for the formation of dimers (Fig. 5D) with a Cg1···Cg2^{v} distance of 3.76 Å (*v* = 1–*x*, –*y*, 1–*z*; Cg1 and Cg2 are the centre of gravity of the pyridine part and benzene part of the quinoline ring, respectively).

CONCLUSION

Herein, the synthesis, spectroscopic characterization and single crystal X-ray diffraction analysis of novel square–planar Pt(II) and Pd(II) complexes with quinoline-2-carboxaldehyde thiosemicarbazone are presented. In both complexes, the ligand is tridentately coordinated in the anionic form *via* the sulfur, quinoline and imine nitrogen donor atoms. The fourth coordination site is occupied by a chlorido ligand. Despite the similar ionic radii of the metal ions and respective coordination bond lengths, crystal packing of the complexes is different. Detailed analysis of non-covalent interactions revealed that non-classical Cl···H interactions are the most represented in both crystal structures. The coordinated chlorine atom is involved in bifurcated non-classical hydrogen interactions. In both crystal structures, one interaction involves the imine carbon atom as a donor. However, in the second interaction, the thioamide nitrogen atom is a donor in the case of **1**, while in the crystal packing of **2**, the interaction involves the *meta* carbon atom of the pyridine part of the aromatic ring. This might contribute to the difference in crystal packings of the synthesized complexes.

SUPPLEMENTARY MATERIAL

Additional data are available electronically at the pages of journal website: https://www.shd-pub.org.rs/index.php/JSCS/index, or from the corresponding author on request.

Additional crystallographic data for the structures reported in this paper have been deposited at the Cambridge Crystallographic Data Centre with quotation numbers CCDC 2044685 and 2044686. They are available free of charge on request *via* www.ccdc.cam.ac.uk/data_request/cif

Acknowledgement. This work was financially supported by the Ministry of Education, Science and Technological Development of the Republic of Serbia (Contract No: 451-03-68/2020-14/200168).

И З В О Д

СТРУКТУРНА СТУДИЈА КОМПЛЕКСА Pt(II) И Pd(II) СА ХИНОЛИН-2-КАРБОКСАЛЕДЕХИД ТИОСЕМИКАРБАЗОНОМ

ПРЕДРАГ Г. РИСТИЋ[1], МАРКО В. РОДИЋ[2], НЕНАД Р. ФИЛИПОВИЋ[3], ДРАГАНА М. МИТИЋ[4], КАТАРИНА К. АНЂЕЛКОВИЋ[1] и ТАМАРА Р. ТОДОРОВИЋ[1]

[1]Универзитет у Београду – Хемијски факултет, Студентски трг 12–16, 11000 Београд, [2]Природно–математички факултет, Универзитет у Новом Саду, Трг Доситеја Обрадовића 4, 21000 Нови Сад, [3]Универзитет у Београду – Пољопривредни факултет, Немањина 6, 11000 Београд и [4]Иновациони центар Хемијског факултета, Универзитет у Београду, Студентски трг 12–16, 11000 Београд

Синтетисана су два квадратно–планарна комплекса, [PtLCl] (**1**) и [PdLCl] (**2**), са хинолин-2-карбоксалдехид тиосемикарбазонским лигандом (HL), који су окарактерисани IR и NMR спектроскопијом и дифракцијом X-зрака са монокристала. У оба комплекса L^- се координовао тридентатно преко истог сета донорских атома, док је четврто координационо место заузео хлоридни јон. Међутим, комплекси нису изостуктурни због различитих врста нековалентних интермолекуларних интеракција. Ове интеракције су анализиране помоћу Хиршфилдових површина и дводимензионалних графикона отисака прстију.

(Примљено 26. новембра, ревидирано 1. децембра, прихваћено 2. децембра 2020)

REFERENCES

1. P. Heffeter, V. F. S. Pape, É. A. Enyedy, B. K. Keppler, G. Szakacs, C. R. Kowol, *Antioxidants Redox Signal.* **30** (2019) 1062 (http://dx.doi.org/10.1089/ars.2017.7487)
2. J. Shim, N. R. Jyothi, N. A. M. Farook, *Asian J. Chem.* **25** (2013) 5838 (http://dx.doi.org/10.14233/ajchem.2013.oh105)
3. G. Pelosi, *Open Crystallogr. J.* **3** (2010) 16 (http://dx.doi.org/10.2174/1874846501003020016)
4. N. P. Prajapati, H. D. Patel, *Synth. Commun.* **49** (2019) 2767 (http://dx.doi.org/10.1080/00397911.2019.1649432)
5. T. S. Lobana, R. Sharma, G. Bawa, S. Khanna, *Coord. Chem. Rev.* **253** (2009) 977 (http://dx.doi.org/10.1016/j.ccr.2008.07.004)
6. E. J. Siddiqui, I. Azad, A R. Khan, T. Khan, *J. Drug Deliv. Therapeut.* **9** (2019) 689 (http://jddtonline.info/index.php/jddt/article/view/2888/2135)
7. T. R. Todorović, A. Bacchi, N. O. Juranić, D. M. Sladić, G. Pelizzi, T. T. Božić, N. R. Filipović, K. K. Andelković, *Polyhedron* **26** (2007) 3428 (http://dx.doi.org/10.1016/j.poly.2007.03.023)
8. N. Gligorijević, T. Todorović, S. Radulović, D. Sladić, N. Filipović, D. Gođevac, D. Jeremić, K. Anđelković, *Eur. J. Med. Chem.* **44** (2009) 1623 (http://dx.doi.org/10.1016/j.ejmech.2008.07.033)
9. T. R. Todorović, A. Bacchi, D. M. Sladić, N. M. Todorović, T. T. Božić, D. D. Radanović, N. R. Filipović, G. Pelizzi, K. K. Andelković, *Inorg. Chim. Acta* **362** (2009) 3813 (http://dx.doi.org/10.1016/j.ica.2009.04.047)
10. S. Bjelogrlic, T. Todorovic, A. Bacchi, M. Zec, D. Sladic, T. Srdic-Rajic, D. Radanovic, S. Radulovic, G. Pelizzi, K. Andelkovic, *J. Inorg. Biochem.* **104** (2010) 673 (http://dx.doi.org/10.1016/j.jinorgbio.2010.02.009)
11. T. Srdić-Rajić, M. Zec, T. Todorović, K. Anelković, S. Radulović, *Eur. J. Med. Chem.* **46** (2011) 3734 (http://dx.doi.org/10.1016/j.ejmech.2011.05.039)

12. N. Filipović, N. Polović, B. Rašković, S. Misirlić-Denčić, M. Dulović, M. Savić, M. Nikšić, D. Mitić, K. Anđelković, T. Todorović, *Monatsheft. Chem.***145** (2014) 1089 (http://dx.doi.org/10.1007/s00706-014-1197-6)
13. N. R. Filipović, S. Bjelogrlić, A. Marinković, T. Ž. Verbić, I. N. Cvijetić, M. Senćanski, M. Rodić, M. Vujčić, D. Sladić, Z. Striković, T. R. Todorović, C. D. Muller, *RSC Adv.* **5** (2015) 95191 (http://dx.doi.org/10.1039/C5RA19849F)
14. I. S. Djordjevic, J. Vukasinovic, T. R. Todorovic, N. R. Filipovic, M. V. Rodic, A. Lolic, G. Portalone, M. Zlatovic, S. Grubisic, *J. Serb. Chem. Soc.* **82** (2017) 825 (http://dx.doi.org/10.2298/JSC170412062D)
15. S. Poirier, H. Lynn, C. Reber, E. Tailleur, M. Marchivie, P. Guionneau, M. R. Probert, *Inorg. Chem.* **57** (2018) 7713 (http://dx.doi.org/10.1021/acs.inorgchem.8b00724)
16. L. M. Epstein, E. S. Shubina, *Coord. Chem. Rev.* **231** (2002) 165 (http://dx.doi.org/10.1016/S0010-8545(02)00118-2)
17. J. Kozelka, in *Noncovalent Forces*, S. Scheiner, Ed., Springer International Publishing, Cham, 2015, pp. 129 (http://dx.doi.org/10.1007/978-3-319-14163-3_6)
18. P. Ristić, V. Blagojević, G. Janjić, M. Rodić, P. Vulić, M. Donnard, M. Gulea, A. Chylewska, M. Makowski, T. Todorović, T. Todorović, N. Filipović, *Cryst. Growth Des.* **20** (2020) 3018 (http://dx.doi.org/10.1021/acs.cgd.9b01661)
19. P. N. Bourosh, M. D. Revenko, M. Gdaniec, E. F. Stratulat, Y. A. Simonov, *J. Struct. Chem.* **50** (2009) 510 (http://dx.doi.org/10.1007/s10947-009-0078-z)
20. *CrysAlisPro Software system*, Agilent Technologies UK Ltd., Cheadle
21. G. M. Sheldrick, *Acta Crystallogr. Sect. A Found. Adv.* **71** (2015) 3 (http://dx.doi.org/10.1107/S2053273314026370)
22. G. M. Sheldrick, *Acta Crystallogr., C* **71** (2015) 3 (http://dx.doi.org/10.1107/S2053229614024218)
23. C. B. Hübschle, G. M. Sheldrick, B. Dittrich, *J. Appl. Crystallogr.* **44** (2011) 1281 (http://dx.doi.org/10.1107/S0021889811043202)
24. A. L. Spek, *Acta Crystallogr., D* **65** (2009) 148 (http://dx.doi.org/10.1107/S090744490804362X)
25. C. F. Macrae, I. J. Bruno, J. A. Chisholm, P. R. Edgington, P. McCabe, E. Pidcock, L. Rodriguez-Monge, R. Taylor, J. van de Streek, P. A. Wood, *J. Appl. Crystallogr.* **41** (2008) 466 (http://dx.doi.org/10.1107/s0021889807067908)
26. C. F. MacRae, I. Sovago, S. J. Cottrell, P. T. A. Galek, P. McCabe, E. Pidcock, M. Platings, G. P. Shields, J. S. Stevens, M. Towler, P. A. Wood, *J. Appl. Crystallogr.* **53** (2020) 226 (http://dx.doi.org/10.1107/S1600576719014092)
27. C. R. Groom, I. J. Bruno, M. P. Lightfoot, S. C. Ward, *Acta Crystallogr., B* **72** (2016) 171 (http://dx.doi.org/10.1107/S2052520616003954)
28. J. J. McKinnon, D. Jayatilaka, M. A. Spackman, *Chem. Commun.* (2007) 3814 (http://dx.doi.org/10.1039/b704980c)
29. J. J. McKinnon, M. A. Spackman, A. S. Mitchell, *Acta Crystallogr., B* **60** (2004) 627 (http://dx.doi.org/10.1107/S0108768104020300)
30. M. Mohan, M. Manmohan, *Synth. React. Inorg. Met. Chem.* **12** (1982) 761 (http://dx.doi.org/10.1080/00945718208082693)
31. L. Yang, D. R. Powell, R. P. Houser, *Dalton Trans.* (2007) 955 (http://dx.doi.org/10.1039/b617136b)
32. R. Boese, M. T. Kirchner, J. D. Dunitz, G. Filippini, A. Gavezzotti, *Helv. Chim. Acta* **84** (2001) 1561 (http://dx.doi.org/10.1002/1522-2675(20010613)84:6<1561::AID-HLCA1561>3.0.CO;2-M)

33. I. Dance, *New J. Chem.* **27** (2003) 22 (http://dx.doi.org/10.1039/b206867b)
34. M. A. Spackman, J. J. McKinnon, *CrystEngComm* **4** (2002) 378 (http://dx.doi.org/10.1039/b203191b)
35. S. L. Tan, M. M. Jotani, E. R. T. Tiekink, *Acta Crystallogr., E* **75** (2019) 308 (http://dx.doi.org/10.1107/S2056989019001129).

Journal of the Serbian Chemical Society
JSCS-info@shd.org.rs • www.shd.org.rs/JSCS
J. Serb. Chem. Soc. *86* (4) S90–S96 (2021) *Supplementary material*

SUPPLEMENTARY MATERIAL TO

Structural study of Pt(II) and Pd(II) complexes with quinoline-2-carboxaldehyde thiosemicarbazone

PREDRAG G. RISTIĆ[1], MARKO V. RODIĆ[2], NENAD R. FILIPOVIĆ[3], DRAGANA M. MITIĆ[4], KATARINA K. ANĐELKOVIĆ[1] and TAMARA R. TODOROVIĆ[1]*

[1]University of Belgrade – Faculty of Chemistry, Studentski trg 12–16, 11000 Belgrade, Serbia, [2]Faculty of Sciences, University of Novi Sad, Trg Dositeja Obradovića 3, 21000 Novi Sad, Serbia, [3]University of Belgrade – Faculty of Agriculture, Nemanjina 6, 11000 Belgrade, Serbia and [4]Innovation Centre of Faculty of Chemistry, University of Belgrade, Studentski trg 12–16, 11000 Belgrade, Serbia

J. Serb. Chem. Soc. *86* (4) (2021) 391–406

*Quinoline-2-carboxaldehyde thiosemicarbazone (**HL**)*

Yield: 0.647 g (51 %); IR (ATR, cm^{-1}): 3393*s*, 3265*m*, 3146*s*, 3062*m*, 3004*m*, 2979*m*, 1605*s*, 1527*vs*, 1501*s*, 1451*s*, 1359*w*, 1321*s*; 1281*s*, 1208*w*, 1111*s*, 1060*m*, 948*vw*, 925*w*, 901*vw*, 867*vw*, 840*m*, 773*w*, 750*m*; ^{1}H-NMR (500 MHz, DMSO-d_6, δ / ppm): 7.58 (1H, *m*), 7.72 (1H, *m*), 7.95 (2H, *m*), 8.20 (1H, *s*), 8.31 (2H, *m*), 8.41(1H, *s*), 8.43 (1H, *s*), 11.77 (1H, *s*). ^{13}C-NMR (126 MHz, DMSO-d_6, δ / ppm): 118.54, 127.55, 128.25, 128.33, 129.20, 130.33, 136.69, 142.96, 147.75, 154.33, 178.91.

* Corresponding author. E-mail: tamarat@chem.bg.ac.rs

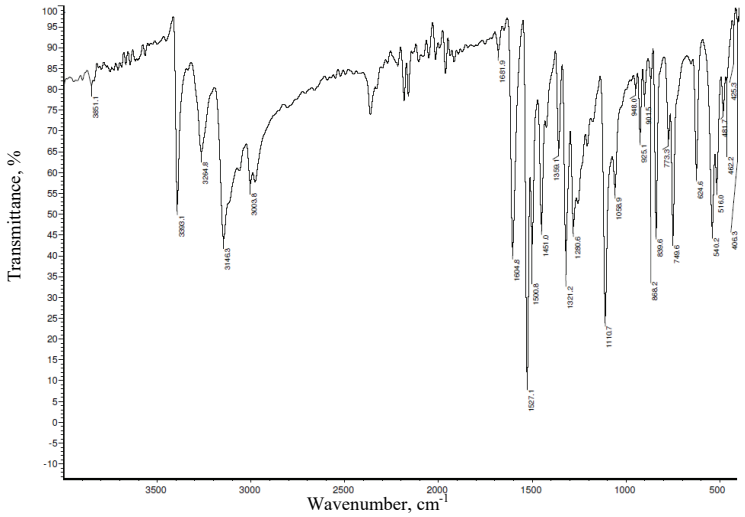

Fig. S-1. IR spectrum of **HL**.

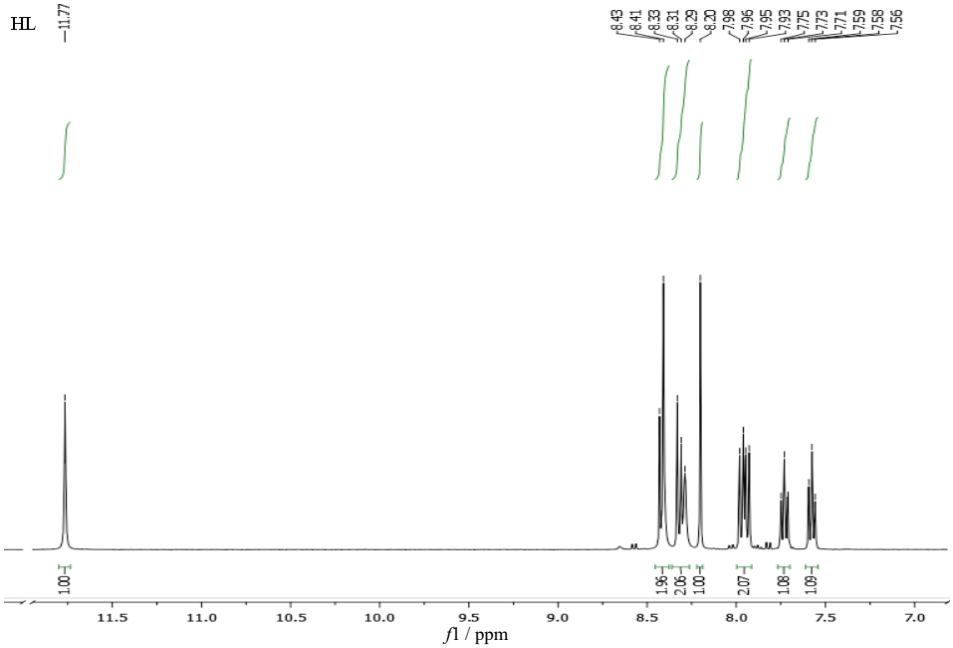

Fig. S-2. ^{1}H-NMR spectrum of **HL**.

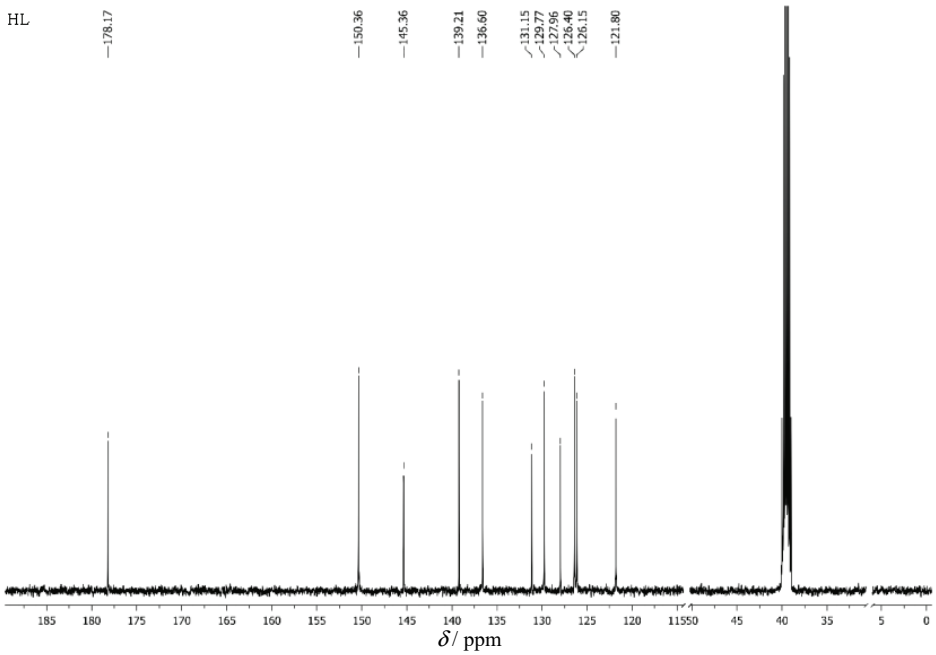

Fig. S-3. ^{13}C-NMR spectrum of **HL**.

Quinoline-2-carboxaldehyde thiosemicarbazonato-N,N,S-*chloridoplatinum(II), [PtLCl] (**1**)*

Yield: 0.04 g (42 %); Anal. calcd. for $C_{11}H_9ClN_4PtS$ (*FW*: 459.82): C, 28.73; H, 1.97; N, 12.18; S, 6.97 %. Found: C, 28.39; H, 1.59; N, 11.89; S, 7.23 %; IR (ATR, cm^{-1}): 3395*m*, 3287*m*, 3224*w*, 3104*m*, 1632*s*, 1576*m*, 1544*m*, 1516*w*, 1471*vs*, 1442*vs*, 1399*s*, 1317*m*, 1290*m*, 1237*w*, 1206*vw*, 1143*m*, 986*w*, 944*vw*, 868*w*, 816*w*, 774*vw*, 745*vw*, 707*w*; ^{1}H-NMR (500 MHz, DMSO-d_6, δ / ppm): 7.70 (1H, *t*), 7.84 (1H, *d*), 7.86 (1H, *m*), 8.05 (1H, *d*), 8.25 (2H, *s*), 8.61 (1H, *s*), 8.74 (1H, *d*), 9.69 (1H, *d*); ^{13}C-NMR (126 MHz, DMSO-d_6, δ / ppm): 121.24, 126.36, 128.08, 128.69, 129.61, 132.54, 141.73, 147.86, 148.24, 161.82, 185.09; Λ_M (1×10^{-3} M, DMSO, Ω^{-1} cm^2 mol^{-1}): 2.76.

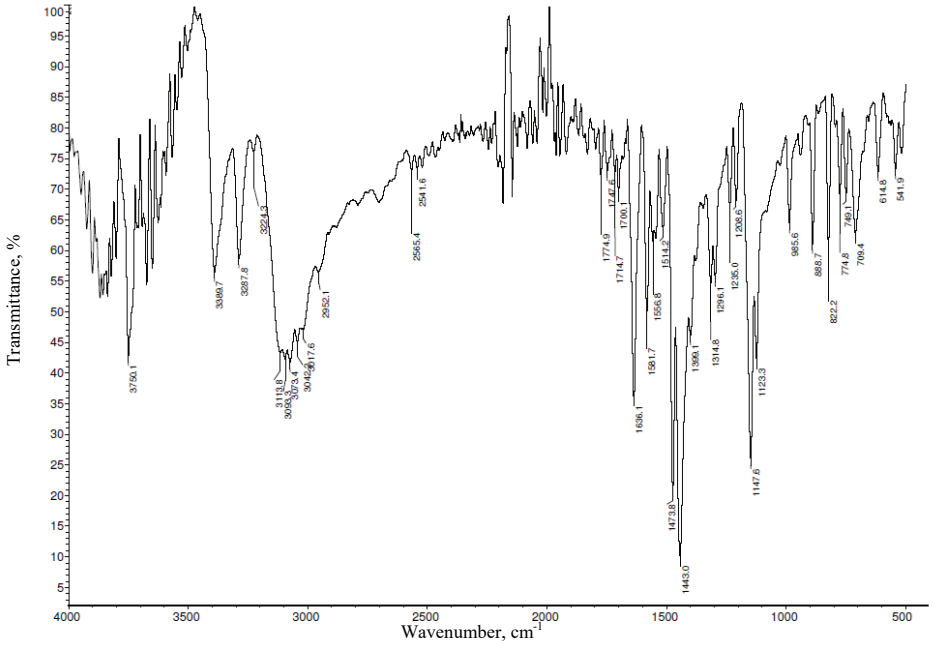

Fig. S-4. IR spectrum of **1**.

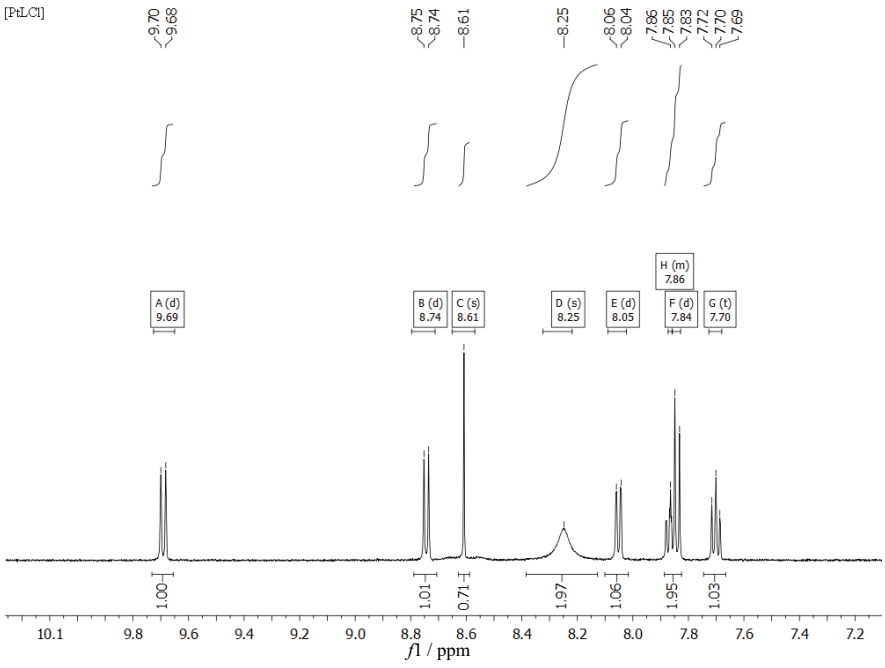

Fig. S-5. ^{1}H-NMR spectrum of **1**.

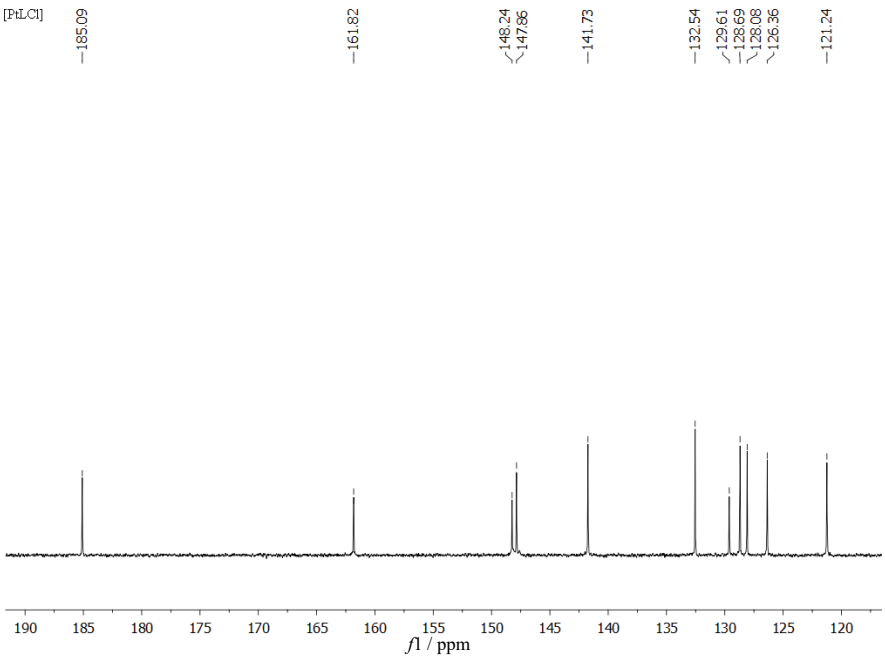

Fig. S-6. ^{13}C-NMR spectrum of **1**.

Quinoline-2-carboxaldehyde thiosemicarbazonato-N,N,S-*chloridopalladium(II), [PdLCl] (**2**)*

Yield: 0.03 g (39 %); Anal. calcd. for $C_{11}H_9ClN_4PdS$ (*FW*: 371.13): C, 35.60; H, 2.44; N, 15.10; S, 8.64 %. Found: C, 35.28; H, 2.52; N, 14.93; S, 8.35 %; IR (ATR, cm^{-1}): 3422*s*, 3362*s*, 3294*s*, 3127*s*, 3041*m*, 2959*m*, 1638*s*, 1598*w*, 1578*w*, 1475*vs*, 1449*vs*, 1398*m*, 1320*w*, 1293*w*, 1233*w*, 1158*s*, 991*w*, 852*w*, 817*w*, 776*w*, 747*w*; ^{1}H-NMR (500 MHz, DMSO-d_6, δ / ppm): 7.69 (1H, *t*), 7.83 (2H, *m*), 8.04 (1H, *d*), 8.06 (1H, *s*), 8.11 (1H, *s*), 8.70 (1H, *d*), 9.48 (1H, *d*); ^{13}C-NMR (126 MHz, DMSO-d_6, δ / ppm): 121.59, 126.9, 128.43, 128.65, 132.27, 141.28, 147.42, 147.55, 159.17, 182.77; Λ_M (1 × 10^{-3} M, DMSO, Ω^{-1} cm^2 mol^{-1}): 1.98.

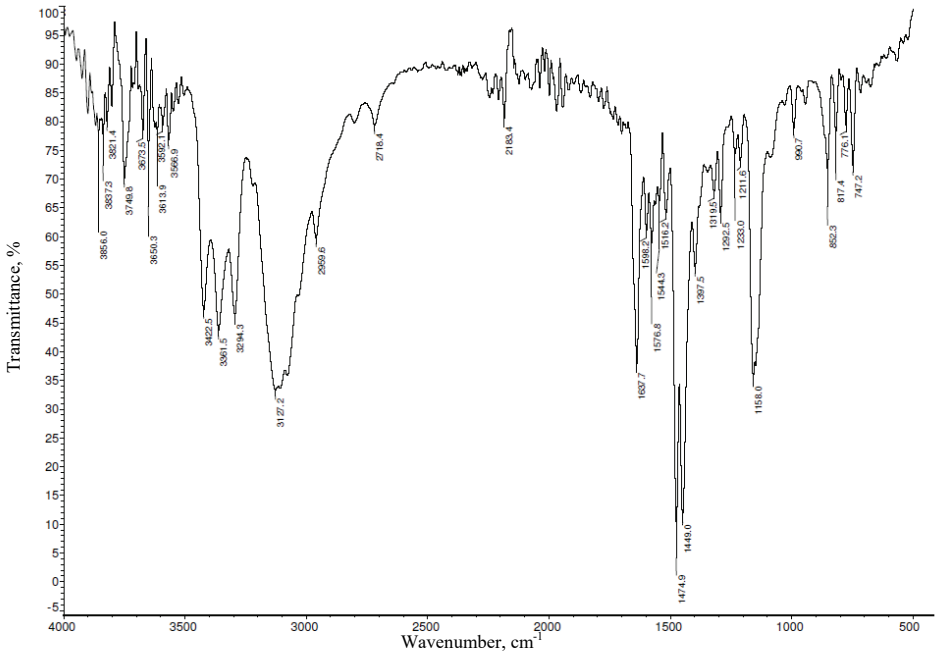

Fig. S-7. IR spectrum of **2**.

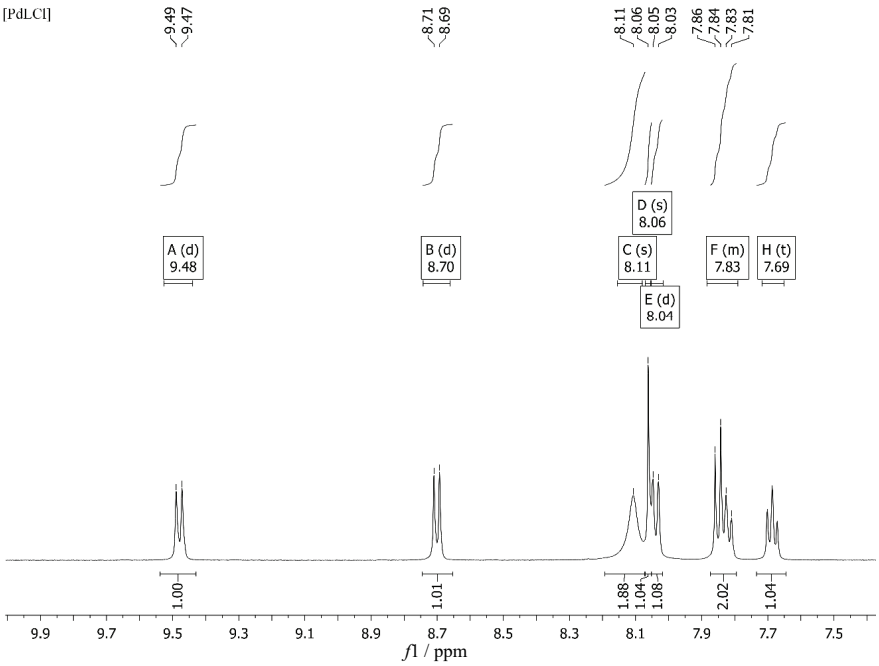

Fig. S-8. ^{1}H-NMR spectrum of **2**.

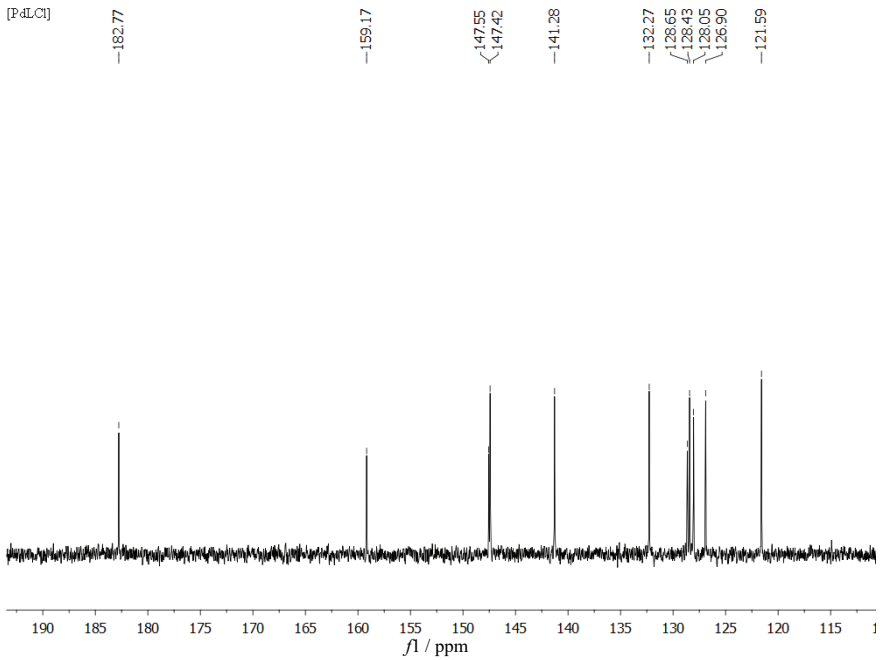

Fig. S-9. ^{13}C-NMR spectrum of **2**.

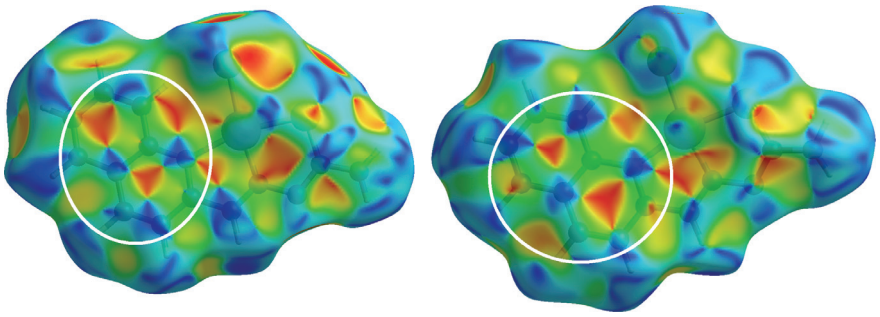

Fig. S-10. Views of the Hirshfeld surface for **1** (left) and **2** (right) mapped over the shape-index property highlighting blue regions about bright-red spots within the quinoline rings, which are highlighted by the white circles.

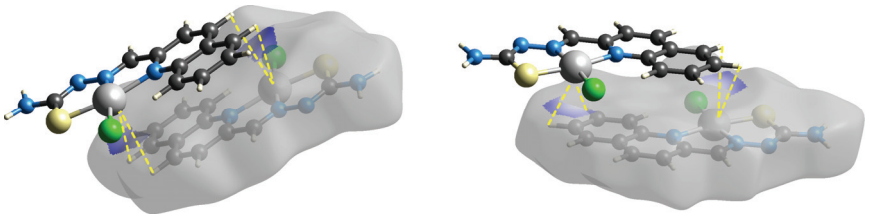

Fig. S-11. Blue patches on the Hirshfeld surfaces for **1** (left) and **2** (right) with highlighted corresponding M···H interactions.

Journal of the Serbian Chemical Society
JSCS-info@shd.org.rs • www.shd.org.rs/JSCS
J. Serb. Chem. Soc. *86* (4) 407–413 (2021)
JSCS–5430
Extended abstract

EXTENDED ABSTRACT

Microstructure, roughness, and corrosion resistance of X5CrNi18-10 austenite stainless steel welded joint•

BOJANA M. RADOJKOVIĆ*#, BORE V. JEGDIĆ#, JOVANKA N. KOVAČINA#, SANJA I. STEVANOVIĆ# and DUNJA D. MARUNKIĆ#

University of Belgrade, Institute of Chemistry, Technology and Metallurgy, Department of Electrochemistry, Njegoševa 12, Belgrade, Serbia

(Received 3 December 2020, accepted 3 February 2021)

Abstract: The influence of the microstructure of X5CrNi18-10 stainless steel welded joint on its resistance to general, pitting, and intergranular corrosion was analyzed. The structure of weld metal, heat affected zone (HAZ) and base metal before and after electrochemical testing was analyzed using SEM/EDS. The influence of the roughness level of the welded joint on its resistance to the mentioned types of corrosion was also examined. Although the degree of sensitization of HAZ was significantly lower than the limit value, HAZ showed a noticeably greater tendency to general and pitting corrosion than weld metal and base metal. Polishing has been shown to improve significantly the corrosion resistance of HAZ than in other parts of a welded joint.

Keywords: test methods; electrochemistry; SEM/EDS; AFM.

INTRODUCTION

Welded joints of X5CrNi18-10 stainless steel, under certain conditions, have a tendency towards various types of localized corrosion, such as pitting corrosion, intergranular corrosion, stress corrosion cracking, *etc*. This poses a major problem in the application of these steels in various industries.

Localized corrosion of stainless steel occurs especially in the presence of chloride ions.[1] Intergranular corrosion occurs along chromium-depleted zones that are formed, for example, in the heat affected zone (HAZ) during welding.[2] The places where pitting corrosion occurs are MnS inclusions, chromium-depleted zones in the HAZ, as well as austenite/ferrite boundaries in the weld metal.[3–7]

* Corresponding author. E-mail: bojana.radojkovic@ihtm.bg.ac.rs
• The lecture held at the meeting of the Electrochemical Division of the Serbian Chemical Society in Belgrade on October 26th, 2020.
Serbian Chemical Society member.
https://doi.org/10.2298/JSC201203007R

There is great disagreement regarding the influence of surface roughness levels on corrosion resistance of stainless steels and other alloys.[8–10] While some deny this effect, others show that there is a direct effect of roughness on corrosion resistance.

In this abstract, the influence of the microstructure of welded joint and surface roughness on resistance to general and pitting corrosion, as well as on the stability of passive film was investigated.

EXPERIMENTAL

Welding of the X5CrNi18-10 stainless steel was performed by the TIG process using constant welding parameters (welding rate 5 cm min^{-1}, current level 150 A, heat input 14.6 kJ cm^{-1}), using argon as shielding gas. The microstructure of individual parts of the welded joint before and after electrochemical testing was analyzed using an SEM/EDS microscope. Having in mind the small dimensions of the welded joint zones, a small electrochemical cell was constructed that enables such tests.

In order to determine the resistance to general and pitting corrosion, polarization measurements were performed in an NaCl solution. Testing of intergranular corrosion was performed by the electrochemical potentiokinetic reactivation method with a double loop (DL EPR). Electrochemical tests were also performed on welded joint specimens with different roughness. The morphology and degree of roughness were analyzed using atomic force microscopy (AFM).

RESULTS AND DISCUSSION

The characteristic parts of a welded joint are shown in Fig. 1. These parts differ in microstructure and show different corrosion resistance.

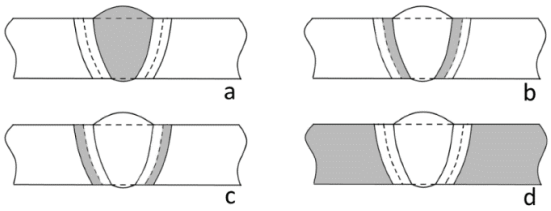

Fig. 1. Parts of the welded joint: a) weld metal, b) HAZ with coarse grain, c) HAZ and d) base metal.

In the weld metal (Fig. 1a) during solidification, a dendritic austenite/ferrite microstructure is formed.[2] Directly to the weld metal, a narrow zone is formed in which, due to the large heat input during welding, a significant grain growth occurred (Fig. 1b). The grain size in this zone ranged from 46 to 69 μm.

In the HAZ (Fig. 1c) during welding, chromium carbides are precipitated at the grain boundary, resulting in the formation of the chromium-depleted zones.[2] Particularly sensitive to pit formation are the places where MnS inclusions intersect these zones. In the HAZ, the grain size was the same as for the base metal (from 18 to 20 μm). In the base metal, there are no microstructural changes.

AFM 3D plots of grinded and polished specimens are shown Fig. 2. Unlike the ground specimen, no grooves were seen on the polished specimen. The RMS value in the ground specimen was 54.0 nm, while in the polished one it was 3.6 nm.

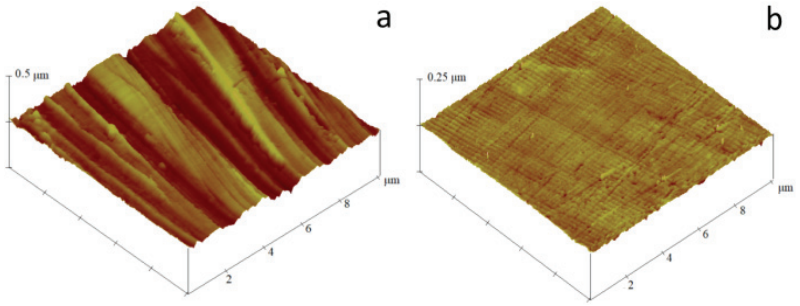

Fig. 2. AFM plots in a 3D perspective: a) ground and b) polished surface of stainless steel.

The intergranular corrosion was tested using the DL EPR method. The ratio of the reactivation current I_r and the passivation current I_p, taking into account the grain size G (G ≈9), is a measure of the resistance of stainless steel to intergranular corrosion:

$$\left(\frac{I_r}{I_p}\right)_{GBA} = \frac{I_r}{I_p\left(10^{-3}\sqrt{2^{G+5}}\right)} \quad (1)$$

The ratio $(I_r/I_p)_{GBA}$ for HAZ was about 3.5 times below the limit value defined by the ISO standard, while in the base metal, this ratio was even lower (Fig. 3). The relatively low value of $(I_r/I_p)_{GBA}$ is a consequence of the low carbon content in the stainless steel.

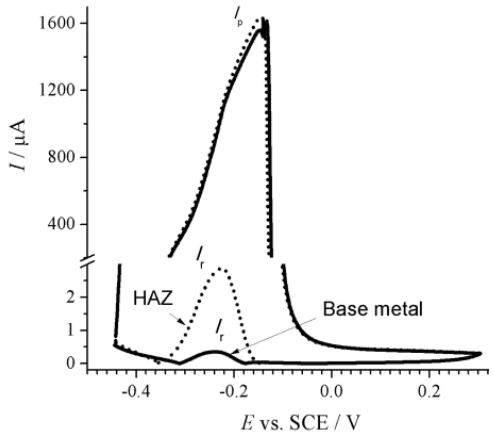

Fig. 3. DL EPR diagram.

The results presented in Fig. 4 show that the HAZ resistance to general corrosion is reduced and the susceptibility to pitting corrosion (compared to the base metal) is increased. This could only be a consequence of the formation of chromium-depleted zones along the grain boundaries in the HAZ.

At potentials lower than E_{pit} (Fig. 4), current peaks are visible, which indicate the formation of metastable pits. At potentials above E_{pit}, the pits grow steadily. The weld metal had the highest resistance to general and pitting corrosion due to its higher content of chromium and nickel than in the base metal. The results of electrochemical tests are summarized in Table I.

TABLE I. Results of electrochemical testing of ground and polished welded joint

Sample		I_{corr} / nA	I_{pass} / nA	E_{mpit} / mV	E_{pit} / mV
Base metal	Grinded	5.5	28	336	387
	Polished	1.5	2.0	387	387
Weld metal	Grinded	6.0	25	326	430
	Polished	1.4	2.2	427	427
HAZ	Grinded	14	40	278	346
	Polished	2.4	3.3	378	378

The polarization curves obtained for polished specimens (Fig. 5) do not contain the characteristic passivation peak, which is visible in the polarization curves in Fig. 4. Besides, metastable pits are not formed. A single pit is probably formed, which continues to grow.

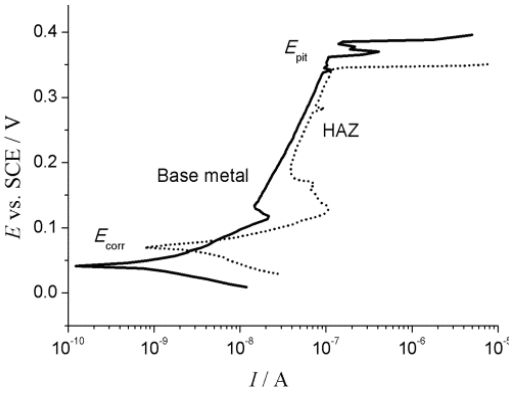

Fig. 4. Polarization diagrams for the base metal and HAZ.

The roughness noticeably affects a change in the corrosion resistance in HAZ. The E_{pit} value for the ground surface was ≈350 mV while for the polished HAZ surface it was ≈380 mV. This is very important because HAZ has a critical place for a welded joint for various types of corrosion. In addition, the polished specimen shows higher resistance to general corrosion, and a more stable passive film (Fig. 5). The real surface of the ground specimen is larger than that of the polished one. A passive film is less stable at the peaks of the grinded surface.

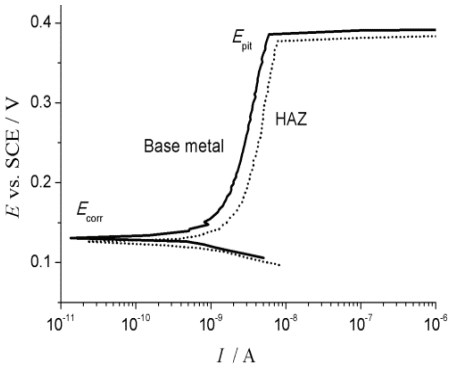

Fig. 5. Polarization diagrams for polished surfaces of the base metal and HAZ.

During pit formation (Fig. 6), first Mn and S dissolve from the inclusions and their dimensions are reduced. At the boundary of the inclusion with the matrix, a channel is created where metastable pits are formed first, as well as stable pits that continue to grow.[3] That the pit was formed in trenches around the central part of the inclusion is shown in Fig. 6b.

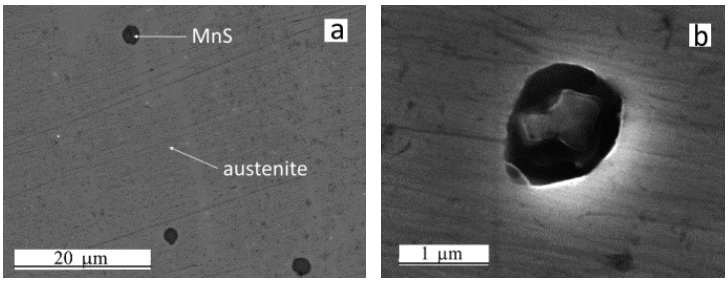

Fig. 6. SEM microphotographs of pit formation stages at MnS inclusions in HAZ.

In the weld metal, pits are most often formed at the austenitic/ferrite boundary (Fig. 7). EDS analysis showed that the chromium content in δ-ferrite is higher than in the austenitic matrix. However, several pits were also formed at a certain distance from *δ*-ferrite in the austenitic matrix.

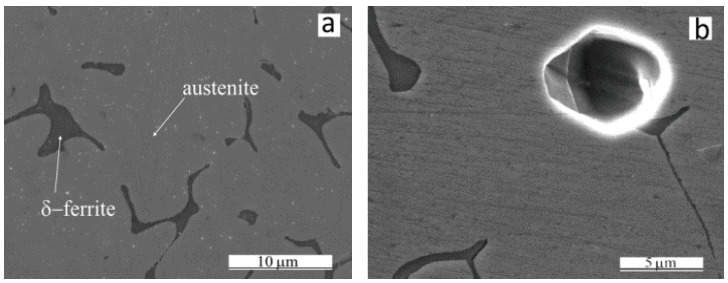

Fig. 7. SEM microphotographs of weld metal: a) before and b) after polarization measurements.

CONCLUSIONS

This paper analyzes the influence of microstructure and roughness levels of the welded joint of X5CrNi18-10 stainless steel on its resistance to general, pitting, and intergranular corrosion.

The polished specimen had greater resistance to general corrosion than the grinded specimen, in all three parts of the welded joint (weld metal, HAZ and base metal). This difference is especially noticeable in the HAZ. Moreover, a passive film on the polished surface is more stably related to the ground surface. In HAZ, the values of the pitting potential E_{pit} and the potential of metastable pitting E_{mpit} for the polished surface are significantly higher than are those for the ground surface. This is very important because HAZ is a critical place for a welded joint for various types of corrosion.

Acknowledgment. This work was financially supported by the Ministry of Education, Science and Technological Development of the Republic of Serbia (Grant No. 451-03-68/2020-14/200026).

И З В О Д

Х МИКРОСТРУКТУРА, ХРАПАВОСТ И ОТПОРНОСТ НА КОРОЗИЈУ ЗАВАРЕНОГ СПОЈА АУСТЕНИТНОГ НЕРЂАЈУЋЕГ ЧЕЛИКА Х5CrNi18-10

БОЈАНА М. РАДОЈКОВИЋ, БОРЕ В. ЈЕГДИЋ, ЈОВАНКА Н. КОВАЧИНА, САЊА И. СТЕВАНОВИЋ и ДУЊА Д. МАРУНКИЋ

Универзитет у Београду, Институт за хемију, технологију и металургију, Центар за електрохемију, Његошева 12, 11000 Београд

Анализиран је утицај микроструктуре завареног споја нерђајућег челика Х5CrNi18--10 на његову отпорност према општој, питинг и интеркристалној корозији. Структура метала шава, зоне утицаја топлоте (HAZ) и основног метала, пре и после електрохемијских испитивања, анализирана је применом SEM/EDS. Такође испитан је утицај нивоа храпавости завареног споја на његову отпорност према наведеним видовима корозије. Иако је степен сензибилизације HAZ био знатно нижи од граничне вредности, ЗУТ је показао значајно већу склоност према општој и питинг корозији него метал шава и основни метал. Показано је да полирање знатно побољшава отпорност ЗУТ према корозији него што је то случај са осталим деловима завареног споја.

(Примљено 3. децембра 2020, прихваћено 3. фебруара 2021)

REFERENCES

1. H. Bohni, *Localized Corrosion of Passive Metals*, in *Uhlig`s Corrosion Handbook*, R. W. Revie, Ed., John Wiley & Sons, Inc, Hoboken, NJ, 2011, p. 157 (https://doi.org/10.1002/9780470872864)
2. J. R. Davis, *Corrosion of Weldments*, ASM International, Materials Park, OH, 2006, p. 43 (https://doi.org/10.1361/corw2006p001)
3. A. Chiba, I. Muto, Y. Sugawara, N. Hara, *J. Electrochem. Soc.* **160** (2013) C511 (https://doi.org/10.1149/2.081310jes)
4. N. Ida, I. Muto, Y. Sugawara, N. Hara, *J. Electrochem. Soc.* **164** (2017) C779 (https://doi.org/10.1149/2.1011713jes)

5. B. T. Lu, Z. K. Chen, J. L. Luo, B. M. Patchett, Z. H. Xu, *Electrochim. Acta* **50** (2005) 1391 (http://dx.doi.org/10.1016/j.electacta.2004.08.036)
6. B. Jegdić, B. Bobić, B. Radojković, B. Alić, Lj. Radovanović, *J. Mater. Process. Technol*. **266** (2019) 579 (https://doi.org/10.1016/j.jmatprotec.2018.11.029)
7. B. Radojković, J. Kovačina, B. Jegdić, B. Bobić, B. Alić, D. Marunkić, A. Simović, *Mater. Corros.* (2020) 1, accepted (https://doi.org/10.1002/maco.202012039)
8. H. Ezuber, A. Alshater, S. O. Nisar, A. Gonsalvez, S. Aslam, *Surf. Eng. Appl. Electrochem.* **54** (2018) 73 (https://doi.org/10.3103/S1068375518010039)
9. M. J. Seo, H.-S. Shim, K. M. Kim, S.-I. Hong, D. H. Hur, *Nucl. Eng. Des.* **280** (2014) 62 (http://dx.doi.org/10.1016/j.nucengdes.2014.08.023)
10. S. Reinemann, P. Rosemann, M. Babutzka, J. Lehmann, A. Burkert, *Mater. Corros*. **70** (2019) 1776 (https://doi.org/10.1002/maco.201910874).

Journal of the Serbian Chemical Society
JSCS-info@shd.org.rs • www.shd.org.rs/JSCS
J. Serb. Chem. Soc. 86 (4) 415–427 (2021)
JSCS–5431
Original scientific paper

Synthesis of $BaTi_5O_{11}$ by an aqueous co-precipitation method *via* a stable organic titanate precursor

PELIN SÖZEN AKTAŞ*

Manisa Celal Bayar University, Faculty of Arts & Sciences, Department of Chemistry, Şehit Prof. Dr. İlhan Varank Campus 45140 Muradiye-Manisa, Turkey

(Received 6 July 2020, revised 10 February, accepted 17 February 2021)

Abstract: $BaTi_5O_{11}$ has been widely researched due to its unique microwave properties. Conventionally, it is challenging to obtain this compound as a single phase. The $BaTi_5O_{11}$ was synthesized *via* a co-precipitation technique using an aqueous solution of titanium(IV)(triethanolaminato) isopropoxide, barium nitrate and ammonia as precursors, which are stable in aqueous media. The phase evolution, purity, and structure were identified by X-ray diffraction (XRD), scanning electron microscopy (SEM) and energy dispersive X-ray (EDX) spectroscopy analysis. The desired $BaTi_5O_{11}$ structure was obtained by calcination at 900 °C. Furthermore, the structure was characterized by TGA, FT-IR and Raman studies. The study showed that the particles were between 80 and 120 nm in size and the average crystallite size was determined from the Scherrer formula as 68.1 nm at 900 °C.

Keywords: barium titanium oxide system; organic titanate; co-precipitation; X-ray diffraction.

INTRODUCTION

Electronic components and other ceramic substrates have been investigated intensively due to the rapid growth of high-frequency wireless communication technology.[1] Low-temperature co-firing ceramic (LTCC) technology is of great interest today to manufacture miniaturized multilayer devices with diverse functions.[2] By utilizing this technology, multi-chip packages have been successfully synthesized using a single sheet to construct and integrate the appropriate electronic components and devices in a compact multi-layered ceramic architecture. After laminating, the sintering temperature should be chosen to be below 1000 °C to use low resistance conductors, such as gold and silver. In this way, rapid signal transmission between modules with high conductivity and energy loss is minimized. LTCC materials are generally preferred for applications such as dual-

* E-mail: pelin.sozen@cbu.edu.tr
https://doi.org/10.2298/JSC200706014A

band baluns, bandpass filters, power distribution networks, point-to-point transceivers (passive elements) and voltage-controlled oscillators, dielectric resonator oscillators, amplifiers and singly balanced mixers.[3] To date, many LTCC materials have been developed and intensively applied, including $BiNbO_4$, $MTiO_3$ (M = Mg, Zn, Ca), $BaO–TiO_2$, $ZnNb_2O_6$, $BaO–R_2O_3TiO_2$ (R = Nd, Sm) and $Li_{1+x-y}Nb_{1-x-3y}Ti_{x+4y}O_3$, *etc*.[2] Among these, compounds in the binary system of $BaO–TiO_2$ have been accurately reported to undoubtedly possess excellent microwave properties. $BaTi_5O_{11}$ has been researched for use in microwave applications considering its superior properties.[4–7] Zhou and co-workers reported that $BaTi_5O_{11}$ synthesized at 1100 °C with CuO addition showed excellent microwave dielectric properties. $BaTi_5O_{11}$ exhibited a dielectric constant (ε_r) of 41.2, a Qf of 47430 GHz (Q is the quality factor and f is the resonant frequency) and a temperature coefficient (τ_f) of 36 ppm $°C^{-1}$.[8] Sintering of $BaTi_5O_{11}$ ceramic with 4 wt. % Ba–ZnO and B_2O_3 (BZB glass) at 900 °C was also reported, and these ceramics demonstrated excellent dielectric properties, that is ε_r = 35.36 and Qf = = 28095 GHz.[9] As wireless communication systems require an LTCC that has been sintered at temperatures below 1000 °C, $BaTi_5O_{11}$ could be enthusiastically recommended as a suitable material candidate for application in microwave ceramic components.

$BaTi_5O_{11}$ was first synthesized by Tillmanns, but the preparation method was not a single-phase process.[10] Afterwards, $BaTi_5O_{11}$ was obtained by a solid-state reaction in the 1970s as an intermediate.[11] A single-phase $BaTi_5O_{11}$ structure could be prepared by chemical processes, such as co-precipitation, sol–gel, hydrothermal, and alkoxide-derived powder sintering.[6,12–15] $BaTi_5O_{11}$ was synthesized at calcination temperatures between 700 and 1100 °C by using alkoxide and sol–gel methods.[6,16,17] On the other hand, single-phase synthesis studies in powder form are currently under investigation using different ways. High-quality powder of $BaTi_5O_{11}$ was obtained by co-precipitation using $BaCl_2$ and $TiCl_4$ as the starting materials.[18] In most cases, these kinds of Ti precursors are moisture sensitive and must be protected from rapid hydrolysis.

In the present study, $BaTi_5O_{11}$ powder was synthesized in an aqueous solution by co-precipitation processing. The starting materials are stable in an aqueous environment and could be efficiently prepared on an industrial scale. It also offers the possibility to work with low temperatures (at 900 °C) and commercially available inexpensive starting materials.

EXPERIMENTAL

Materials and method

Barium nitrate (>99 % purity, Sigma Aldrich), titanium (triethanolaminato) isopropoxide solution (80 wt. % in isopropanol, Sigma Aldrich), nitric acid (HNO_3, 65 wt. % and NH_3, 25 wt. %, Isolab) were used as the starting materials. The obtained calcined powders were characterized by X-ray diffraction (XRD) on a PANalytical Empyrean diffractometer with Cu

Kα radiation (λ = 1.5406 Å) with a scan speed of 0.05° s^{-1}, in the 2θ range from 10 to 80°. Match! version 3 crystal impact was used for phase identification and composition.[19] The X-ray pattern of the sample calcined at 900 °C was analyzed by the Rietveld refinement program FULLPROF using the data obtained at 1° min^{-1} scan rate in the 20–70° 2θ range.[20] The crystal structure was pictured by the VESTA program.[21] FTIR spectra of the samples were recorded on Spectrum BX Perkin Elmer FT-IR spectrometer using KBr pellets. Spectragryph Software for optical spectroscopy Version 1.2.13 was used to create multi-spectrum plots.[22] For Raman analysis, Renishaw Invia Raman System equipped with a Leica model confocal microscope and an Argon-ion laser light source (532 nm) and 50× objective was used. Thermogravimetric analysis was performed on a SII 7300 Perkin Elmer thermal analyzer under flowing N_2 at 2.5 mL min^{-1} from 25 to 1200 °C at a heating rate of 5 °C min^{-1}. Scanning electron microscopy (SEM) was used to analyze the morphology of the synthesized $BaTi_5O_{11}$ structure. SEM images were taken by a Zeiss Gemini 500 microscope. The average particle diameters were measured from each SEM image. Energy-dispersive X-ray spectroscopy (EDX) was used to ascertain the chemical composition of the material.

Preparation of $BaTi_5O_{11}$

The $BaTi_5O_{11}$ powders were prepared by a simple co-precipitation process. A barium nitrate solution was prepared by dissolving $Ba(NO_3)_2$ (4 mmol, 0.1054 g) in 20 mL ultrapure water. This solution was then added to an organic titanate mixture (20 mmol, 6.328 g, titanium (triethanolaminato) isopropoxide solution) in 80 mL of 1M HNO_3 aqueous solution. The concentrations of Ba^{2+} and Ti^{4+} in the solution were 0.04 and 0.2 M, respectively. The mixture was stirred at room temperature for 1 h to obtain a pellucid solution (pH 1). The pH of the solution was adjusted to 9 by adding an aqueous 1 M ammonia solution. After precipitation was complete, the suspension was further stirred at 50 ºC for 2 h. The suspension was first cooled to room temperature then kept in a deep-freezer (about –20 °C) for 1 h. The precipitate was filtered and washed with a small amount of cold ultrapure water and dried at 80 °C in a vacuum oven. The resultant material was first calcined for 4 h at different temperatures ranging from 700 to 1000 °C at a heating rate of 5 °C min^{-1} in an alumina crucible. The synthesis route of the co-precipitation method is given in Fig. 1.

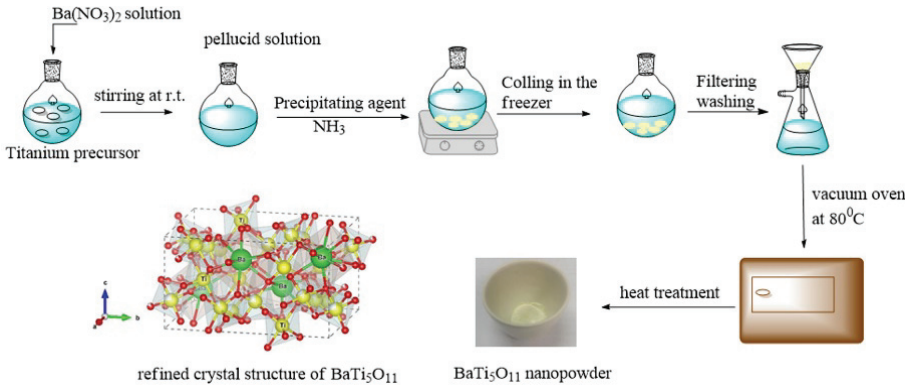

Fig. 1. Representation of the key steps of $BaTi_5O_{11}$ synthesis *via* the proposed co-precipitation method.

RESULTS AND DISCUSSION

Synthesis of $BaTi_5O_{11}$

Preparation of large amounts of barium titanium oxide systems requires economic, air-stable starting precursors, high yields, aqueous media, and excellent reproducibility. The $BaTi_5O_{11}$ system is challenging to prepare and is often synthesized as an intermediate product.[11] For this purpose, to obtain $BaTi_5O_{11}$, a simple synthetic route has been developed in an aqueous medium. The proposed reaction mechanism for the preparation of $BaTi_5O_{11}$ by the co-precipitation method is shown in Eqs. (1)–(7):

$$C_9H_{19}NO_4Ti + 4HNO_{3(aq)} \rightarrow Ti(NO_3)_{4(aq)} + C_3H_7OH + C_6H_{15}NO_3 \quad (1)$$

$$Ba(NO_3)_{2(s)} \xrightarrow{H_2O} Ba^{2+}_{(aq)} + 2NO^-_{3(aq)} \quad (2)$$

$$Ba^{2+}_{(aq)} + 2NO^-_{3(aq)} + 5Ti^{4+}_{(aq)} + 20NO^-_{3(aq)} + 22NH^+_{4(aq)} + 22OH^-_{(aq)} \quad (3)$$

$$\downarrow \text{co-precipitation}$$

$$Ba(OH)_{2(s)} + 5Ti(OH)_{4(s)} + 22NO^-_{3(aq)} + 22NH^+_{4(aq)} \quad (4)$$

$$\downarrow \text{filtration}$$

$$Ba(OH)_{2(s)} + 5Ti(OH)_{4(s)} \quad (5)$$

$$\downarrow \text{heat-treatment}$$

$$BaO_{(s)} + 11H_2O_{(g)} + 5TiO_{2(s)} \quad (6)$$

$$\downarrow$$

$$BaTiO_{3(s)} + 4TiO_{2(s)} + BaTi_5O_{11(s)} \quad (7)$$

The mechanism for the co-precipitation reaction has been proposed considering similar studies using organic titanate.[14,23] Under acidic conditions, it may be regarded as that 2-propanol and triethanolamine are formed by the addition of 1 M HNO_3 to the titanium (triethanolaminato) isopropoxide solution in the first step (Eq. (1)). In the second step, precipitation was realized by addition of ammonia to the barium nitrate and acidic titanate solution. Ammonia (1 M) was added until pH 9 for complete precipitation as represented in Eq. (3). In the solution, the concentration of Ba^{2+} was 0.04 M while that of Ti^{4+} was 0.2 M before ammonia addition. The first species precipitated in the solution is a water-insoluble titanium hydroxide. Barium hydroxide is strongly basic and soluble in water. Using the cooling process for precipitation allowed the formation of barium hydroxide. Similar observations were detected in the precipitation reaction with 1 M NaOH using barium acetate and dihydroxybis(ammoniumlactato) titanium.[14]

After filtering, washing, and drying processes, the precipitate was calcined to different temperatures. The proposed mechanism is based on the XRD analysis of samples obtained from the calcination process and represented in Eq. (5)–(7).

XRD profile at 800 °C indicates that trace amounts of $BaTiO_3$ and TiO_2 formation. TiO_2 synthesis from titanium (triethanolaminato) isopropoxide solution in acidic media was reported by Kong *et al.*[23] At temperatures below 800 °C, it could be assumed that BaO and TiO_2, as well as $BaTiO_3$, are formed. In the next step, the $BaTi_5O_{11}$ structure was obtained from $BaTiO_3$ and TiO_2 at 900 °C.

XRD analysis and rietveld refinement

The XRD powder patterns of the $BaTi_5O_{11}$ precursors calcined at different temperatures are presented in Fig. 2. The XRD profiles show that the $BaTi_5O_{11}$ structure started to form at 800 °C. In the sample calcined at 700 °C, the organic residues were not separated, and the structure of the barium titanium oxide system was not formed (Supplementary material to this paper, Fig. S-1). In the sample calcined at 800 °C, a three-phase mixture of $BaTi_5O_{11}$ (64.6 wt. %, JCPDS No. 35-0805), TiO_2 (18.0 wt. %, JCPDS No. 21-1272) and $BaTiO_3$ (17.4 wt. %, JCPDS No. 79-2263) was observed. At 900 °C, $BaTi_5O_{11}$ as a single-phase was formed. Song and co-workers reported similar observations. In the study, $BaTi_5O_{11}$ was prepared from the precursors $BaTiO_3$ and TiO_2.[25] The powder XRD pattern of the dried sample calcined at 1000 °C indicated partial decomposition of $BaTi_5O_{11}$ giving a mixture of $BaTi_5O_{11}$ (65.7 wt. %), $BaTi_4O_9$ (8.1 wt. %, JCPDS No. 34-0070) and $Ba_4Ti_{13}O_{30}$ (26.2 wt. %, JCPDS No. 35-0750). In studies related to $BaTi_5O_{11}$ synthesis, it was observed that the structure began to deteriorate, and second or third phases emerged. Javadpour *et al.*[24] reported the decomposition of $BaTi_5O_{11}$ into $Ba_2Ti_9O_{20}$ and TiO_2. Additionally, Tangjuank *et al.*[6] and Song *et al.*[25] reported second and third phase formation.

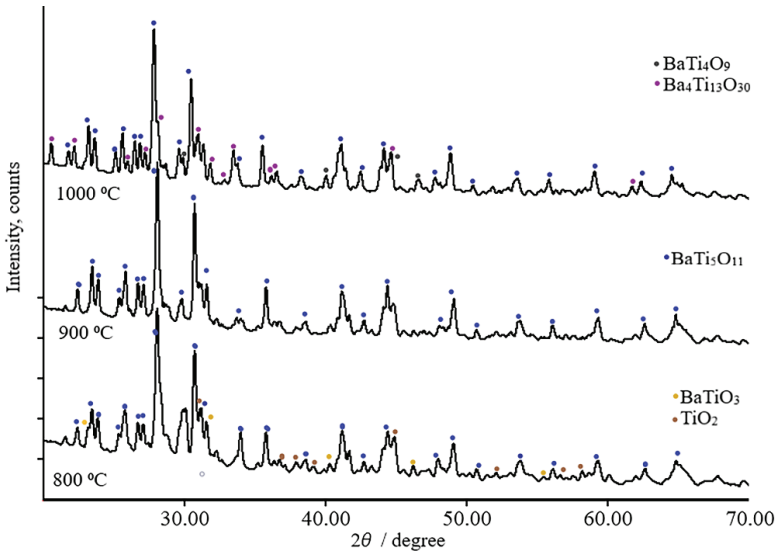

Fig. 2. Powder XRD patterns of dried samples calcined for 4 h at different temperatures.

Song and co-workers reported that in the temperature range below 900 °C, both $BaTi_5O_{11}$ and $BaTi_4O_9$ increased with calcination temperature and above 900 °C, the $BaTi_5O_{11}$ content started to decrease, and the $BaTi_4O_9$ content increased.[25]

The XRD results also showed well-defined diffraction peaks, and the major peaks were identified a monoclinic phase, indicating that $BaTi_5O_{11}$ powders can be prepared by a simple co-precipitation method and heat treatment at 900 °C.

Since the single-phase $BaTi_5O_{11}$ was obtained by calcination at 900 °C, this sample was chosen for Rietveld refinement (Fig. 3). The refinement parameters and the unit cell parameters are very compatible with data obtained by Tillmans *et al.*[10] The model provides a good fit between the observed and calculated X-ray diffraction profiles. A summary of the refinement and unit cell parameters for the $BaTi_5O_{11}$ powder is interpreted in Table I, while atomic positions are given in Table II. The *R* factors show a reliable structural model. In the Rietveld refinement, the pseudo-Voigt function was used with standard Debye–Scherrer geometry to describe the peak shape. Since site occupancies obtained from the Rietveld refinement of $BaTi_5O_{11}$ give $Ba_{1.17}Ti_{4.785}O_{17.973}$ as the composition, it could wrongly be concluded that the oxygen content is increased by almost 70 %. This is actually a consequence of the great difference between the X-ray scattering powers of Ba and O atoms and hence this increase should not be considered as a real one.

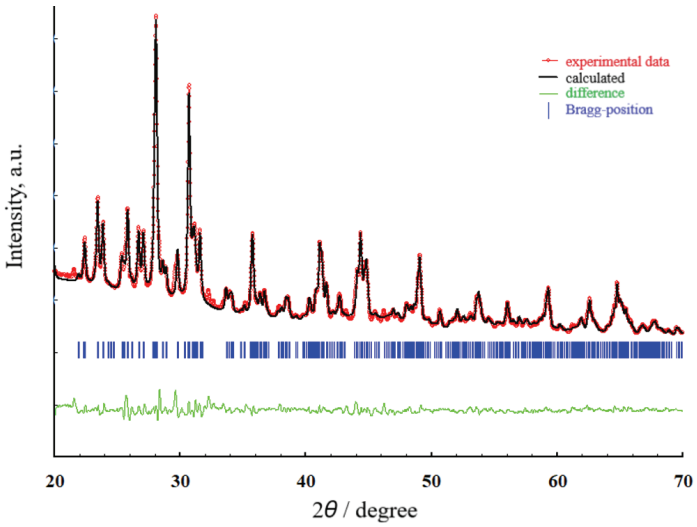

Fig. 3. Rietveld refinement of $BaTi_5O_{11}$.

The refined crystal structure of $BaTi_5O_{11}$ is shown in Fig. 4. The unit cell contains four twelve-fold coordinated barium ions. Their bonding to the Ti octahedrons is realized through shared oxygen atoms. Twenty Ti^{4+} are ideally placed in the center of the octahedron formed by oxygen ions. The average crystallite

size estimated by the Scherrer formula was 68.1 nm at 900 °C, using the (140) diffraction peak.

TABLE I. Structure refinement parameters and crystal data for $BaTi_5O_{11}$

Formula: $BaTi_5O_{11}$
Formula weight: 552.66 g/mol
T = 298 K
λ = 1.54060 Å
Monoclinic crystal system, Space group – P 1 $2_1/n$ 1 (#14)
Unit cell parameters: a = 7.6670(3) Å; b = 14.0410(3) Å; c = 7.5325(3) Å; β = 98.3710(2)°
Volume = 802.25 (1) Å^3
Z = 4
Calculated Density = 4.588 g cm^{-3}
2θ range = 10.0078–79.9922°; 2θ step = 0.0131°
χ^2 = 2.60 %; R_F = 5.59 %; R_{Bragg} = 5.72 %
R_p = 12.7 %; R_{wp} = 13.9 %; R_{exp} = 8.59 %

TABLE II. Atomic positions for $BaTi_5O_{11}$ calcined at 900 °C for 4 h

Atom	Wyckoff position	x	y	z	Occupancy
Ba	4*e*	0.220 (3)	0.086 (3)	0.204 (3)	1.171 (3)
O1	4*e*	0.989 (3)	0.265 (3)	0.005 (3)	1.189 (2)
O2	4*e*	0.120 (3)	0.410 (3)	0.797 (3)	2.129 (2)
O3	4*e*	0.375 (3)	0.246 (3)	0.132 (3)	1.076 (2)
O4	4*e*	0.241 (3)	0.232 (3)	0.713 (3)	3.098 (2)
O5	4*e*	0.421 (3)	0.399 (3)	0.953 (3)	1.033 (2)
O6	4*e*	0.783 (3)	0.429 (3)	0.061 (3)	2.039 (2)
O7	4*e*	0.157 (3)	0.402 (3)	0.194 (3)	1.487 (2)
O8	4*e*	0.075 (3)	0.249 (3)	0.385 (3)	1.119 (2)
O9	4*e*	0.343 (3)	0.431 (3)	0.539 (3)	1.168 (2)
O10	4*e*	0.516 (3)	0.412 (4)	0.273 (3)	0.789 (2)
O11	4*e*	0.92 (3)	0.429 (3)	0.388 (3)	2.846 (1)
Ti1	4*e*	0.193 (3)	0.320 (4)	0.959 (3)	1.269 (2)
Ti2	4*e*	0.223 (3)	1.000 (3)	0.760 (3)	0.737 (2)
Ti3	4*e*	0.348 (3)	0.337 (4)	0.377 (3)	1.139 (2)
Ti4	4*e*	0.565 (3)	0.331 (4)	0.089 (3)	0.787 (2)
Ti5	4*e*	0.97 (3)	0.334 (4)	0.255 (3)	0.853 (2)

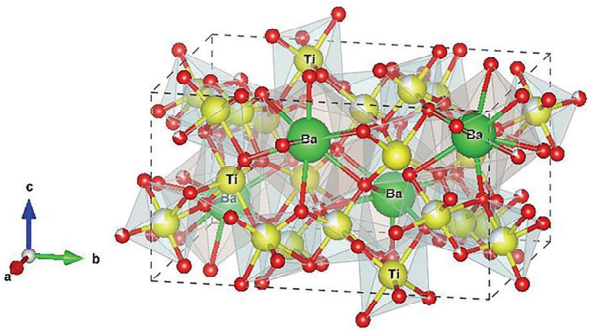

Fig. 4. Refined crystal structure of monoclinic $BaTi_5O_{11}$.

TGA–DTG Analysis

The presented curves corresponding to the TGA and DTG analyses are given in Fig. 5. The first weight loss between 50 to 200 °C was attributed to the desorption of adsorbed water and light volatiles, such as 2-propanol, with a total loss of about 15 wt. %. The second weight loss up to 410 °C was due to dehydration and destruction of small organic residuals, which were also observed in the FT-IR spectrum of powder dried at 80 °C. The mass is almost stable above 410 °C. Finally, between 900 and 1000 °C, the powder weight remained at about 78 wt. % of the sample.

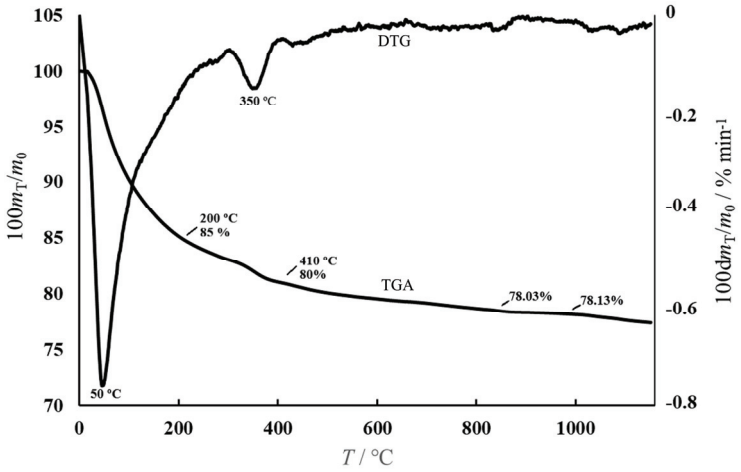

Fig. 5. TGA and DTG curves of the as-prepared $BaTi_5O_{11}$ powders dried at 80 °C.

FT-IR and Raman analysis

The phase identification of $BaTi_5O_{11}$ powders synthesized by the homogenous precipitation technique was further analyzed by FT-IR and Raman spectroscopy. The obtained FT-IR data was found to be consistent with the literature.[6] The IR spectra of the as-prepared and dried $BaTi_5O_{11}$ powder calcined at different temperatures are shown in Fig. 6. The absorption peaks at 3819 (O–H stretching), 3443 (N–H asymmetric stretching), 1959 (C–H bending), 1628 (N–H bending), 1349 (NO_3^- asymmetric stretching) and 1093 cm^{-1} (NO_3^- symmetric stretching) for the as-prepared sample at 80 °C correspond to the vibration modes of the functional groups of the starting precursors. After calcination of the dried powder, these characteristic peaks disappeared. At 800 °C, the peaks appear at 663, 556, 472 and 442 cm^{-1}. These new bands below 800 cm^{-1} support the formation of the $BaTi_5O_{11}$ structure. The FTIR spectra of the $BaTi_5O_{11}$ system have characteristic absorption peaks between 800–400 cm^{-1}, and these are used to identify the phase formation.[6,18]

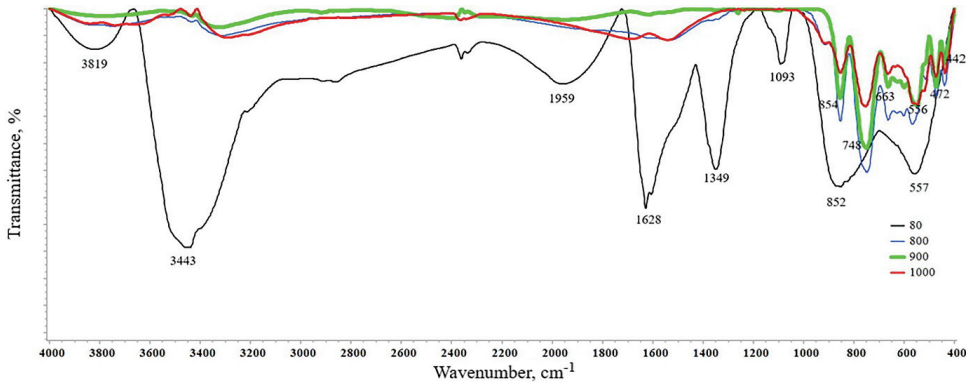

Fig. 6. FT-IR spectra of $BaTi_5O_{11}$ calcined at different temperatures of as prepared precipitate dried at: 1) 80, 2) 800, 3) 900 and 4) 1000 °C.

The room temperature Raman spectrum of $BaTi_5O_{11}$ obtained at 900 °C is showm in Fig. 7. The $BaTi_5O_{11}$ sample prepared at 900 °C for 4 h showed characteristic peaks at 140, 194, 219, 243, 262, 294, 310, 343, 415, 487, 541, 590, 673, 747 and 835 cm^{-1}, which confirmed that the material was pure. The analysis also indicated that the results agreed with those of Lu *et al.*[16], Javadpour *et al.*[24] and Alvarez–Docio *et al.*[4] The Raman characterization for the thermally treated sample at 900 °C confirmed the formation of the $BaTi_5O_{11}$ phase.

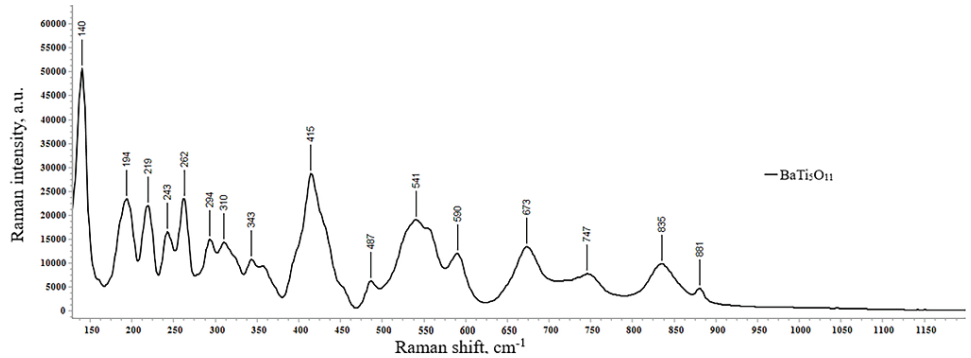

Fig. 7. Raman spectrum of the $BaTi_5O_{11}$ synthesized by co-precipitation at 900 °C.

SEM and EDX analysis

The morphologies of the $BaTi_5O_{11}$ nanoparticles were studied by scanning electron microscopy. SEM micrographs of particles at 900 °C are shown in Fig. 8.

As seen in the SEM images, the synthesized $BaTi_5O_{11}$ grains were in almost round shape and agglomerated. The particle sizes determined from the SEM images were between 80–120 nm. EDX analysis of particles calcined at 900 °C is given in Fig. 9 and confirmed the accuracy of the elemental composition. These

results demonstrate that the simple co-precipitation method is relatively useful for producing fine particles.

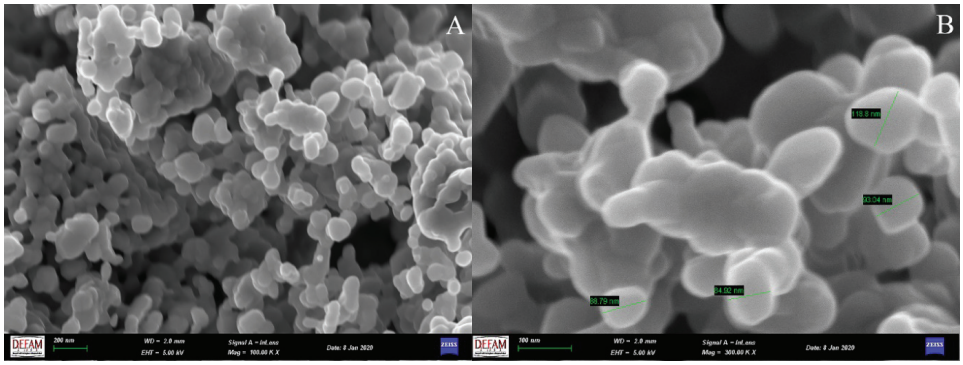

Fig. 8. SEM micrographs of $BaTi_5O_{11}$ particles at 900 °C (A, B). Detected grain sizes from selected points (B: 84.92, 88.79, 93.04, 118.8 nm).

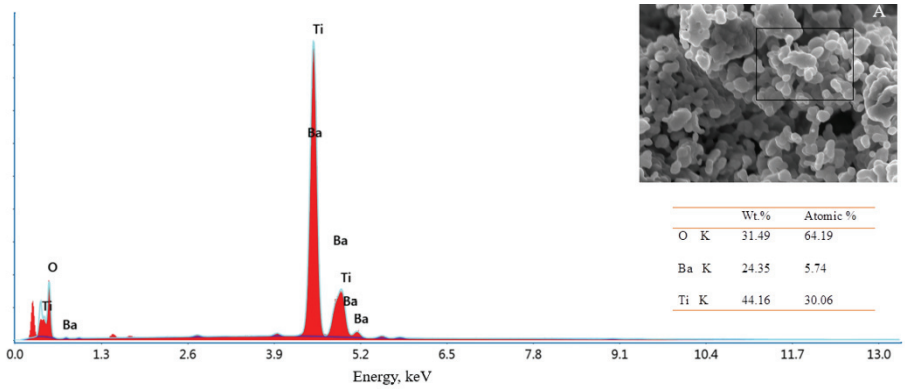

Fig. 9. EDX analysis of particles calcined at 900 °C.

Comparison of results with literature data

The synthesis processes of $BaTi_5O_{11}$ are summarized in Table III (also corresponding literature are included for comparison).

In the present study, $BaTi_5O_{11}$ of 80–120 nm particle size was synthesized from $Ba(NO_3)_2$ and an organic titanate precursor. By comparing with other methods, this synthesis process demonstrated many advantageous properties such as low calcination temperature, lack of a minor second phase, and using economically inexpensive air-sensitive precursors. It could be considered for possible applications in LTCC systems due to its co-fired properties under 1000 °C by using electrodes such as Ag, Cu without high process temperatures, leading to energy consumption.

TABLE III. Experimental conditions for $BaTi_5O_{11}$ prepared by various methods

Method	Precursors	Conditions	Morphology	Reference
Co-precipitation	$Ba(NO_3)_2$ organic titanate	4 h, 900 °C	80–120 nm (particle size)	In the present study
Co-precipitation	$BaCl_2$; $TiCl_4$	4 h, 1100 °C	600 nm (particle size)	Tangjuank *et al.* [18]
Hydrothermal	$Ba(CH_3COO)_2$ $C_6H_{18}N_2O_8Ti$	20 h, 280 ºC	20–65 nm (particle size)	Liu *et al.*[14]
Alkoxide	Ba and Ti-isopropoxide	48 h, 1120 °C	1 μm (grain size)	Fukui *et al.*[12]
Solid-state[a]	$BaCO_3$ $TiOCl_2$	10 days r.t. aging 1 min, 1000 °C	40–200 nm (grain size)	Álvarez–Docio *et al.*[4]
Citrate Route	$Ba(NO_3)_2$ $TiCl_4$	4 h, 1100 °C	30–50 nm (particle size)	Choy *et al.*[26]

[a]Formation of $BaTiO_3$, $BaTi_4O_9$ intermediates

CONCLUSIONS

In the present study, $BaTi_5O_{11}$ nano powders were successfully synthesized by the co-precipitation method using commercially available, low-cost, and stable organic titanate complex of triethanolamine. This is also an advantageous feature when compared with other preferred synthesis methods. The reaction process is an effective method to synthesize the $BaTi_5O_{11}$ structure for applications on low-temperature co-fired ceramics.

By using this newly developed secure method, a simple aqueous synthesis pathway was improved, and single-phase $BaTi_5O_{11}$ powder was produced at 900 °C. TGA-DTG, FT-IR, and XRD analyses also confirmed that the nano powders were obtained at 900 °C. The average crystallite particle size was 68 nm, as determined by XRD. SEM analyses showed that these particles were agglomerated, almost round in shape, and with a size of 80–120 nm.

SUPPLEMENTARY MATERIAL

Additional data are available electronically at the pages of journal website: https://www.shd-pub.org.rs/index.php/JSCS/index, or from the corresponding author on request.

Acknowledgements. This work was supported by the Scientific Research Project Office of Manisa Celal Bayar University, Project No: 2019-056. This paper's analyses were partially performed at Manisa Celal Bayar University (Turkey) – Applied Science and Research Center (DEFAM).

И З В О Д

СИНТЕЗА $BaTi_5O_{11}$ КОПРЕЦИПИТАЦИЈОМ ПОМОЋУ СТАБИЛНОГ ОРГАНСКОГ ТИТАНАТНОГ ПРЕКУРСОРА

PELIN SÖZEN AKTAŞ

Manisa Celal Bayar University, Faculty of Arts & Sciences, Department of Chemistry, Şehit Prof. Dr. İlhan Varank Campus 45140 Muradiye-Manisa, Turkey

$BaTi_5O_{11}$ се доста испитује захваљујући диелектричним својствима и примени у микроталасним уређајима. Међутим, конвенционалним поступцима се тешко може

добити једнофазни $BaTi_5O_{11}$. У овом раду је $BaTi_5O_{11}$ синтетисан методом копреципитације коришћењем водених раствора титан(IV)(триетаноламинато)-изопропоксида, баријум-нитрата и амонијака као прекурсора који су стабилни у воденој средини. Фазне трансформације током жарења на различитим температурама, фазни састав добијених прахова и структура су испитивани рендгенском дифракционом анализом (XRD), скенирајућом електронском микроскопијом (SEM) енергетском дисперзивном спектроскопијом (EDX). Жељена $BaTi_5O_{11}$ структура једобијена калцинацијом на 900 °C. Такође, за карактеризацију су коришћене и термогравиметријска анализа (TGA), инфрацрвена спектроскопија са Фуријеовом трансформацијом (FT-IR) и Раманска спектроскопија. Утврђено је да су честице праха добијеног калцинацијом на 900 °C између 80 и 120 nm и да је просечна величина кристалита добијена коришћењем Шерерове формуле 68,1 nm.

(Примљено 6. јула 2020, ревидирано 10. фебруара, прихваћено 17. фебруара 2021)

REFERENCES

1. J. Guo, D. Zhou, H. Wang, X. Yao, *J. Alloys Compd.* **509** (2011) 5863 (https://dx.doi.org/10.1016/j.jallcom.2011.02.155)
2. Y. Z. Hao, H. Yang, G. H. Chen, Q. L. Zhang, *J. Alloys Compd.* **552** (2013) 173 (https://doi.org/10.1016/j.jallcom.2012.10.110)
3. L. Ren, X. Luo, H. Zhou, *J. Am. Ceram. Soc.* **101** (2018) 3874 (https://dx.doi.org/10.1111/jace.15694)
4. C. M. Álvarez-Docio, J. J. Reinosa, G. Canu, M. T. Buscaglia, V. Buscaglia, J. F. Fernández, *Inorg. Chem.* **58** (2019) 8120 (https://dx.doi.org/10.1021/acs.inorgchem.9b00865)
5. Y. Higuchi, H. Tamura, *J. Eur. Ceram. Soc.* **23** (2003) 2683 (https://dx.doi.org/10.1016/S0955-2219(03)00193-6)
6. S. Tangjuank, T. Tunkasiri, *Mater. Sci. Eng., B* **108** (2004) 223 (https://dx.doi.org/10.1016/j.mseb.2003.11.022)
7. C. H. Hsu, W. S. Chen, H. H. Tung, P. C. Yang, J. Sen Lin, *Adv. Mater. Res.* **677** (2013) 153 (https://dx.doi.org/10.4028/www.scientific.net/AMR.677.153)
8. H. Zhou, H. Wang, Y. Chen, K. Li, X. Yao, *J. Am. Ceram. Soc.* **91** (2008) 3444 (https://dx.doi.org/10.1111/j.1551-2916.2008.02623.x)
9. Y. Chen, E. Li, S. Duan, S. Zhang, *ACS Sustain. Chem. Eng.* **5** (2017) 10606 (https://dx.doi.org/10.1021/acssuschemeng.7b02589)
10. V. E. Tillmanns, *Acta Cryst. B***25** (1969) 1444 (https://dx.doi.org/10.1107/s0567740869004195)
11. H. M. O'Bryan, JR., J. Thomson, JR, *J. Am. Ceram. Soc.* **58** (1974) 454 (https://dx.doi.org/10.1111/j.1151-2916.1975.tb19022.x)
12. T. Fukui, C. Sakurai, M. Okuyama, *J. Mater. Res.* **7** (1992) 192 (https://link.springer.com/article/10.1557/JMR.1992.0192#citeas)
13. S. Li, X. Li, K. Zou, Z. Huang, L. Zhang, X. Zhou, D. Guo, Y. Ju, *Mater. Lett.* **245** (2019) 215 (https://dx.doi.org/10.1016/j.matlet.2019.02.122)
14. L. Liu, X. Li, K. Zou, Z. Huang, C. Wang, L. Zhang, D. Guo, Y. Ju, *J. Mater. Sci. Mater. Electron.* **31** (2020) 6883 (https://dx.doi.org/10.1007/s10854-020-03250-9)
15. K. Zou, L. Liu, X. Li, S. Li, Z. Huang, L. Zhang, D. Guo, Y. Ju, *Mater. Lett.* **255** (2019) 126584 (https://dx.doi.org/10.1016/j.matlet.2019.126584)
16. H. Lu, L. E. Burkhart, G. L. Schrader, *J. Am. Ceram. Soc.* **74** (1991) 968 (https://dx.doi.org/10.1111/j.1151-2916.1991.tb04329.x)

17. J. J. Ritter, R. S. Roth, J. E. Blendell, *J. Am. Ceram. Soc.* **62** (1986) 155 (https://doi.org/10.1111/j.1151-2916.1986.tb04721.x)
18. S. Tangjuank, L. D. Yu, T. Tunkasiri, *Smart Mater. Struct.* **12** (2003) 656 (https://doi.org/10.1088/0964-1726/12/4/317)
19. *Match! - Phase Identification from Powder Diffraction, Crystal Impact - Dr. H. Putz & Dr. K. Brandenburg GbR*, Bonn, Germany, http://www.crystalimpact.com/match
20. J. Rodríguez-Carvajal, *Phys., B* **192** (1993) 55 (https://dx.doi.org/10.1016/0921-4526(93)90108-I)
21. K. Momma, F. Izumi, *J. Appl. Crystallogr.* **41** (2008) 653 (https://dx.doi.org/10.1107/S0021889808012016)
22. F. Menges, *Spectragryph - optical spectroscopy software, version 1.2.13*, 2019 (http://www.effemm2.de/spectragryph)
23. L. Kong, I. Karatchevtseva, M. Blackford, I. Chironi, G. Triani, *J. Am. Ceram. Soc.* **95** (2012) 816 (https://dx.doi.org/10.1111/j.1551-2916.2011.05002.x)
24. J. Javadpour, N. G. Eror, *J. Am. Ceram. Soc.* **71** (1988) 206 (https://dx.doi.org/10.1111/j.1151-2916.1988.tb05849.x)
25. Y. Song, F. Wang, Z. Jiang, Y. Zhou, *J. Mater. Sci. Lett.* **18** (1999) 177 (https://dx.doi.org/10.1023/A:1006699409996)
26. J. Choy, Y. Han, J. Kim, Y. Kim, J. Mater. Chem. **5** (1995) 57 (https://dx.doi.org/10.1039/JM9950500057).

Journal of the Serbian Chemical Society
JSCS-info@shd.org.rs • www.shd.org.rs/JSCS
J. Serb. Chem. Soc. 86 (4) S97 (2021)
Supplementary material

SUPPLEMENTARY MATERIAL TO

Synthesis of $BaTi_5O_{11}$ by an aqueous co-precipitation method *via* a stable organic titanate precursor

PELIN SÖZEN AKTAŞ*

Manisa Celal Bayar University, Faculty of Arts & Sciences, Department of Chemistry, Şehit Prof. Dr. İlhan Varank Campus 45140 Muradiye-Manisa, Turkey

J. Serb. Chem. Soc. 86 (4) (2021) 415–427

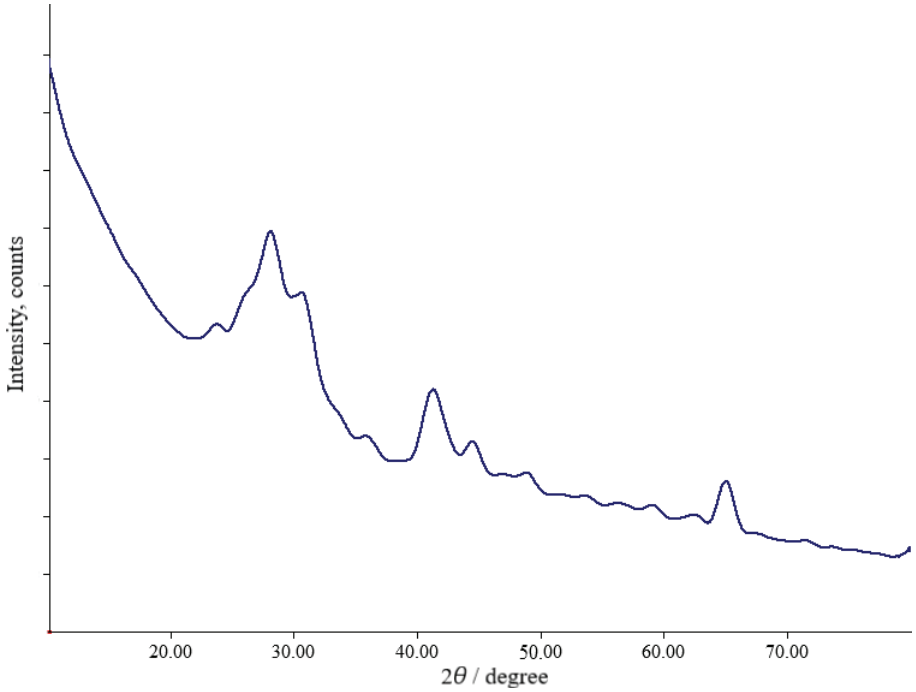

Fig. S-1. Powder XRD pattern of dried sample calcined at 700 °C.

* E-mail: pelin.sozen@cbu.edu.tr

Journal of the Serbian Chemical Society
JSCS-info@shd.org.rs • www.shd.org.rs/JSCS
J. Serb. Chem. Soc. 86 (4) 429–444 (2021)
JSCS–5432
Original scientific paper

Activated carbon from mustard stalk biomass: Synthesis, characterization and application in wastewater treatment

KALPANA PATIDAR and MANISH VASHISHTHA*

Department of Chemical Engineering, Malaviya National Institute of Technology, Jaipur 302017, Rajasthan India

(Received 3 November 2020, revised 27 January, accepted 30 January 2021)

Abstract: Present work is focused on the preparation of mustard stalk activated carbon (MSAC) using chemical activation with H_3PO_4 and exploring its properties for its use in dye removal from wastewater. Adsorption variable (dosage, contact time, and solution pH), pore structure, morphology, surface functional groups, equilibrium kinetics and isotherm study for the removal of methylene blue (MB) using MSAC were investigated. The present study showed that an adsorption dosage of 0.2 g L^{-1} and pH 8 can be considered as optimum for the MB removal. SEM result showed that pore of MSAC was larger than the pore of the mustard stalk (MS). BET surface area and total pore volume of MSAC were found as 510 m^2 g^{-1} and 0.33 cm^3 g^{-1}, respectively. Equilibrium adsorption data were examined by Langmuir and Freundlich isotherm models. Better correspondence to the Langmuir model with a maximum adsorption capacity of 212.76 mg g^{-1} (MB onto MSAC) was obtained. Dimensionless factor, R_L revealed favourable nature of the sorption in the MSAC–MB system. Adsorption rates were found to follow the pseudo-second-order kinetics with good correlation. These results show that the MSAC could be used as a renewable and economical alternative to commercial activated carbon in the removal of MB dye from wastewater.

Keywords: adsorption; isotherm; methylene blue; kinetics.

INTRODUCTION

Effluent from various process industries leads to significant pollution due to the transportation of aqueous dye solution into the water bodies and soil. Majority of dyes used in industries are of synthetic origin and are toxic in nature, among the synthetic dyes used in various industries. Methylene blue (MB) is a commonly used cationic dye (chemical name tetraethylthionine chloride, $C_{16}H_{18}ClN_3S$ and molecular weight is 319.85 g mol^{-1}) which finds application in the textile industry to color leather, wool, cotton, and also in paper coating.[1]

* Corresponding author: mvashishtha.chem@mnit.ac.in
https://doi.org/10.2298/JSC201103010P

Toxicity of MB manifests itself in form of teratogenicity, mutagenicity, neurotoxicity, nucleic acid damage, *etc*. Chronic exposure to MB dye leads to adverse health problems like vomiting, change in mental state or confusion, high pulse rate, jaundice, shock, burns injury of the eye, tissue necrosis, cyanosis, and limb paralysis, making it imperative to invent some efficient dye removal techniques from wastewater.[2] Also, MB and other dye laden wastewater adversely impact the aquatic ecosystem along with deteriorating the visual appeal of any water body by making it coloured and sometimes also leads to an obnoxious smell. Some important techniques used to treat dye-containing industrial wastewater (values in bracket indicate removal efficiency) includes biological (86 %), oxidation (90 %), ozonation (94.5 %), photochemical (99 %), adsorption (99 %), ion exchange (86.8 %), coagulation and flocculation (93.6 %), electrochemical (88.8 %), membrane technology (97.1 %) *etc*.[3,4] Some of these methods have disadvantages like the formation of large quantities of hazardous by-products, often high energy-intensive, and high operating costs.[5] Among the above-listed methods adsorption process using activated carbon is far more effective for dye removal from effluent keeping the environmental perspective in view.

Activated carbon (AC) as the name suggests is a carbon-based material in form of solid black powder resembling powdered or granular charcoal. Its peculiar characteristics like its highly porous nature leading to the availability of large internal surface area coupled with its sufficiently high mechanical strength make it suitable for use as an effective adsorbent with widespread industrial applications such as in gas purification, wastewater treatment (domestic and industrial), and as catalyst or catalyst supports.[6] Many textile industries widely use comercial AC for the treatment of wastewater carrying dyes in aqueous solution owing to its ability to treat dye laden wastewater in more concentrated forms.[7] The high cost of AC presents difficulty in its use on a large scale and consequently, the development of low-cost alternative adsorbents is needed as soon as possible and a lot of research is going on in this direction.

Coal and agricultural residues, rich in lignocellulosic content, are two major sources of the commercial-grade AC. Out of these sources, the agricultural wastes proved to be an economical bet for making AC due to two reasons: firstly, it helps in the saving of depleting fossil fuel (coal/coke) and secondly, it helps in the sustainable waste management by enormous agro residues generated. Some of the agricultural residues finding applications in making adsorbent include sawdust[8], mustard husk[9,10], peanut shell[11], tobacco residues,[12] *etc*.

The physicochemical properties of AC are mainly governed by the technique of activation, activating agent, and the nature of precursor. Two available modes for the production of AC are physical and chemical activation. Chemical activation is preferred over the physical method because of its less time consuming, requires low heating temperature, provides high specific surface area along with

well-controlled porosity.[13] Despite the various available chemical activation agents (like KOH, K_2CO_3, NaOH and Na_2CO_3), H_3PO_4 was found as a suitable reagent due to its low-cost and an environment-friendly dehydrating catalyst, which helps in the decomposition of the component present in MS at relatively low activation temperatures along with causing less corrosion to the activation equipment.[14]

The present work is focused on the development of an alternative, efficient, low-cost AC using mustard crop residue (MCR). The presence of glucosinolate content in MCR which is hazardous to animal health renders it unfit for consumption as fodder also thus making it imperative to convert it into other value-added product.[15] Mustard is one of the major oilseed crops grown globally in China, India, EU, and Canada as prominent producers, and its global annual production for 2019–20 is about 68.19 million metric tons per year.[16] India as a major mustard producer (annual production of 7.7 million metric tons per year) contributes 11.29 % to global production. Processing one ton of the mustard seed yields 1.85 tons of residue in form of mustard straw and husk.[17]

Not much research is reported on the utilization of mustard stalk (MS) as a renewable and economical source of the upgraded product as AC.[9,10] Thus to enhance the existing knowledge the present work is carried out by the adsorption of MB on MSAC from MS studied at different in adsorbent dosage, contact time, dye concentration, and pH. The obtained AC was characterized by proximate and ultimate analysis, BET surface area, SEM-EDX, TG and FTIR to explore its possibility of being used as a low-cost adsorbent for the removal of MB. Also, the isotherm and the kinetic models were applied to find out a better understanding of the adsorption process of MB on MSAC.

EXPERIMENTAL

Materials

MS for the preparation of AC was obtained from a village located close to the institute near Jaipur which is situated in Rajasthan, India (Variety, PM-21). For the experiment, analytical grade reagents used were: MB as adsorbate, H_3PO_4 as activation agent (99.99 wt.% purity), and HCl for washing (99.99 wt.% purity). All these solutions and reagents were purchased from Sigma–Aldrich. Double distilled water was used in the dilution and washing of samples.

Activated carbon preparation

The chemical activation method was followed by the preparation of AC using raw MS and H_3PO_4 as activating agent. The methodology for AC production used in the present work is depicted in Fig. 1.

The above methodology starts from MS being first washed with hot distilled water to remove the attached impurities (dust, *etc*.) and then dried in a hot air oven at 105 °C for 24 h followed by crushing, grinding, and sieving to obtain particles of 60 mesh sizes. Powdered MS is then subjected to carbonization by putting it in a furnace for 1 h, maintained at 550 °C under an inert atmosphere to obtain MS char. 30 g of this char was impregnated at 80 °C for 6

h with 250 cm^3 solutions containing the activating agent (H_3PO_4). The mixture was dehydrated overnight in an oven at 105±1 °C for 24 h. The dried samples were further thermally treated at a temperature of 768 °C in a muffle furnace, in the oxygen-deficient atmosphere for 60 min, in order to obtain MSAC. The optimum conditions for activation were reported in our previous work.[18] MSAC sample obtained was thoroughly washed using hot and cold distilled water to remove any excess H_3PO_4 until neutral pH was obtained. After thorough washing, the samples were dried overnight in a hot air oven at 105 °C, and thereafter weighed and packed for future characterization.

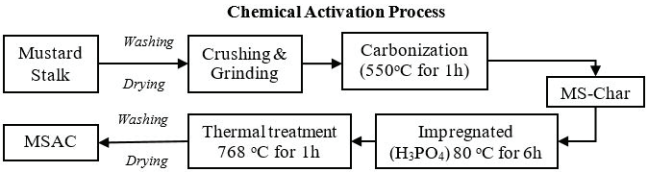

Fig. 1. MSAC production methodology.

Characterization of adsorbent

The surface morphology and the elemental analysis of MS and MSAC were done using scanning electron microscopy (SEM) with energy dispersive X-ray analysis (EDX, Nova Nano FE-SEM 450, FE). The functional groups present in the sample were characterized by Fourier transform infrared (FTIR, FT-IR Spectrum 2, Perkin Elmer) with a working range of 4000 to 500 cm^{-1}. Thermogravimetric (TG, SII 6300 EXSTAR, India) analysis was carried out by heating a 10 mg MS sample in a purge of nitrogen (flow rate 200 ml min^{-1}), and a temperature range from ambient to 727 °C at 20 °C min^{-1} heating rate. The ASTM D3174-73 standard was adopted for the ash content determination and the nitrogen adsorption/desorption experiments were conducted by Quantachrome Autosorb analyzer (using N_2 at 77 K). The total pore volume was performed by nitrogen adsorption at $p/p_o = 0.98$.

Equilibrium and isotherm studies

The experiments for adsorption of MB on MSAC were studied at different adsorbent dosage, contact time, dye concentration, and pH. Changes in any of these parameters will affect the rate of adsorption. To achieve the desired rate of removal, the optimum adsorption conditions should be determined. The study of adsorption isotherm and the adsorption kinetics is done. The runs and conditions at which the adsorption experiments were conducted are presented in Table I.

The fixed amount of adsorbent (0.2 g L^{-1}) MSAC in our case was mixed with MB dye solutions of different initial concentrations, ranging from 10-50 mg L^{-1} in 250 mL conical flasks, for obtaining the adsorption equilibrium. The mixture was mixed at 160 rpm for 180 min. Once the agitation is completed, the dye solution was subjected to centrifugation for 15 min at a speed of 2800 rpm, due to which the char particles settled at the bottom of the tube. UV-Vis spectrophotometer (Evolution 220, Thermo Fisher Scientific, USA) at a wavelength of 664 nm was employed to determine the concentration of MB solution. The removal percentage (R) of the dye (MB) by the MSAC (adsorbents), the adsorption capacity of MB at equilibrium, q_e / mg g^{-1}, and the amount of adsorption at time t, min, q_t / mg g^{-1}, was calculated using Eqs. (1)–(3) respectively:

$$R = 100\frac{C_o - C_e}{C_o} \quad (1)$$

$$q_e = \frac{(C_o - C_e)}{W} V \quad (2)$$

$$q_t = \frac{(C_o - C_t)}{W} V \quad (3)$$

here, C_o (initial state), C_t (any time), and C_e (equilibrium state) represents the MB concentrations of dye solution in mg L^{-1} respectively; V / L is the dye solution volume of the dye and W / g is the mass of dry AC (adsorbent) used.

TABLE I. Runs and conditions of adsorption experiment

Experimental item	MSAC content, g L^{-1}	Concentrations of dyes, mg L^{-1}	Sampling time, min	Temperature °C	Vibration rate, rpm
Effect of dosage	0.05 to 0.3 (0.05, 0.1, 0.15, 0.2, 0.25, 0.3)	30	180	30	160
Effect of concentration with time	0.2	10 to 50 (10, 20, 30, 40, 50)	30 to 180 (30, 60, 90, 120, 180)	30	160
Effect of pH	0.2	30	180	30	160
Adsorption isotherms	0.2	10 to 50 (10, 20, 30, 40, 50)	180	30	160
Adsorption kinetics	0.2	10 to 50 (10, 20, 30, 40, 50)	30 to 180 (30, 60, 90, 120, 180)	30	160

RESULTS AND DISCUSSION

Characterization of sample

TG analysis. TG analysis (Fig. 2) was done to study the general decomposition behaviour of MS before the activation. The TGA profiles depict the trend of mass loss occurring in the sample with time when heated in the temperature range of 30-200 °C, this weight loss is due to the dehydration of the MS sample.[19] The loss of unbound moisture resulted in an 11.08 % decrease in weight in the above temperature range. This value bears a close resemblance to the moisture percentage of the MS (Table II).

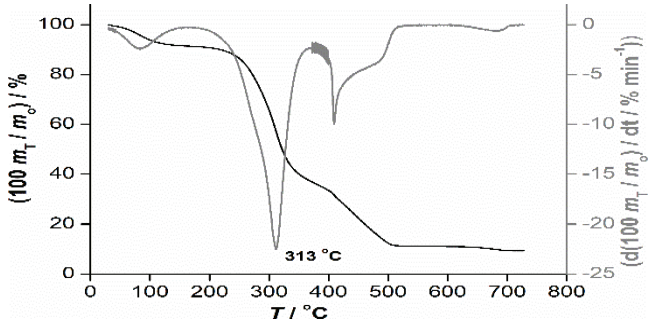

Fig. 2. TG analysis of MS at 20 °C min^{-1}.

The maximum weight loss occurred between the 200–467 °C range, which is a result of thermal decompositions of hemicellulose, cellulose and partial decomposition of lignin present in the biomass sample.[20] In this range, the mass loss is about 74 %. The main peak in the DTG curve is observed at ~313 °C due to the thermal decomposition of the above components present in MS. As the temperature is increased beyond 500 °C weight loss that is not very significant takes place due to no further breakdown of lignocellulosic material. Weight loss at the final temperature of 727 °C is 90.25 %. Thus, from the above observations, it can be inferred that the temperatures beyond 550 °C are more suitable for the conducting of activation, since the sample shows insignificant decomposition.

SEM-EDX analysis. The element-wise composition of raw MS and MSAC samples are given in Table II from which it is clear that the use of H_3PO_4, as an activating agent has a significant influence on the production of AC with the sufficiently high carbon content (68.64 %). The carbon percentage of the MSAC samples shows a marked increase as compared to the raw MS (53.68 %) after the activation process; however, oxygen, hydrogen, and nitrogen contents exhibit the opposite trend, as expected. Due to the high temperature carbonization and the activation process, the MS undergoes decomposition which occurs together with the expulsion of volatile compounds (*viz.*, oxygen, hydrogen, nitrogen), contained by the formed MSAC, thus making it carbon-rich. Also, the chemical activation of MS using H_3PO_4 selectively strips H and O away from it.

The morphology of MS is shown in Fig. 3a from which it can be seen that the basic structure of MS comprises longitudinal fibres and it seems that the pores are preserved in the fibrous cellular structure. However, after the chemical activation of MS to obtain MSAC, as seen in Fig. 3b, a more randomized pore/ /cavities distribution is obtained, which can be attributed to the modification of cellular structure by the acid activation agent. Rich cavities surface of MSAC will provide favourable adsorptive property towards MB dye molecules.

TABLE II. Ultimate, proximate and BET analysis of MS and MSAC

Proximate analysis	Content, wt.%		Surface property	Content, wt.%	
	MS	MSAC		MS	MSAC
Moisture	9.58	4.32	Bulk density, kg m^{-3}	86	503.23
Volatile material	71.92	15.32	Average pore diameter, nm	–	2.64
Ash	4.41	9.59	BET surface area, m^2 g^{-1}	95	510
Fixed carbon	14.09	70.77	Total pore volume, cm^3 g^{-1}	0.081	0.33
			Mesoporous volume, cm^3 g^{-1}	0.06	0.17
Ultimate analysis					
C	53.68	68.64			
H	4.04	1.23			
N	2.90	2.97			
O	43.45	23.97			
S	0.08	0.40			

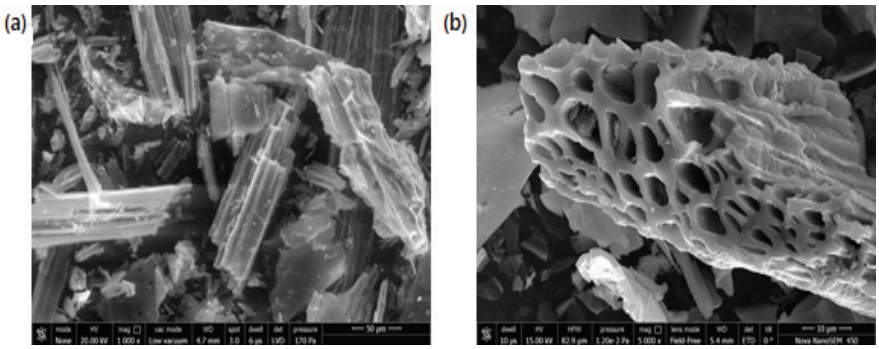

Fig. 3. Morphology of: (a) MS and (b) MSAC prepared with H_3PO_4 activation.

FTIR and BET surface area analysis. The sample surface functional groups are detected using FTIR spectroscopy. The FTIR spectra of the MS, MSAC before and after the MB adsorption as shown in Fig. 4a and b, respectively, and they show a variation of peaks with intensity and position arising out of the vibrational variations of the surface functional groups. The adsorption peak at 3500––3250 cm^{-1} (due to stretching vibration of O–H) was of low intensity in MSAC. The peak intensity reduces due to a corresponding reduction in H-bonding, happening as a result of a reaction between activating agent which in the present case is H_3PO_4 (acting as a dehydrating agent) and MS.[21]

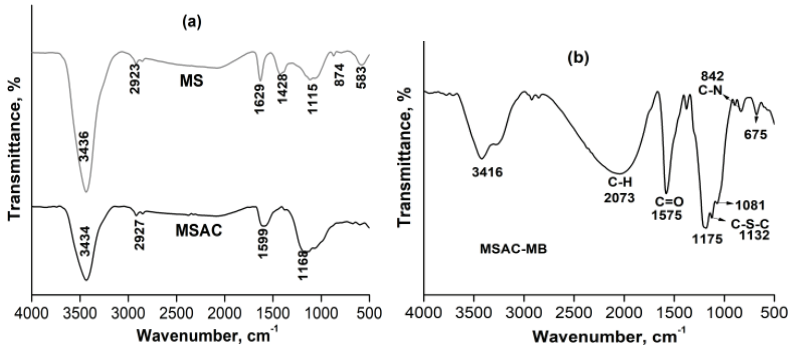

Fig. 4. FTIR spectra of: a) MS and MSAC and b) MSAC-MB.

The peaks corresponding to the bandwidth of 2902–2939 cm^{-1}, arising due to the asymmetric C–H stretching vibration of alkanes and alkyl groups, are more prominent for the raw MS *vis a vis* MSAC. The underlying phenomena behind this observation is a large scale hydrogen removal during the activation process. The ultimate analysis also depicts this trend of reduction in hydrogen and oxygen content of MSAC (Table II).

The band at 1600–1500 cm^{-1} (C=C band of the aromatic rings) shows the aromatization of adsorbent.[22] After activation with H_3PO_4, a peak at around

1168 cm^{-1} appear in the FTIR spectrum of MSAC, which corresponds to P–O–C vibrational variations of aliphatic phosphates groups. 1000–1250 cm^{-1} (stretching vibration of C–O and/or C–O–C in acids, phenols, alcohols, ethers, and/or esters groups).[23] The band about 914 and 756–697 cm^{-1} shows C–H out-of-plane bending in an aromatic ring. The peaks at 3434, 2927, 1599 and 1168 cm^{-1} are shifted to 3416, 2905, 1575 and 1132 cm^{-1}, respectively (Fig. 4b). This shift in the absorption peak suggested the interactions of dye molecules with the functional groups of MSAC.

The BET surface area, total pore volume, and mesoporous volume of MSAC were calculated as 510 $m^2\ g^{-1}$, 0.33 and 0.171 $cm^3\ g^{-1}$ respectively (Table II). The increases in the pore volumes and average pore radius after activation is a result of macropores deformation resulting in their transformation into mesoporous due to the H_3PO_4 effect.

Effect of an operational parameter on MB adsorption

Effect of adsorbent (MSAC) dosage. The adsorption of MB on MSAC was studied at an initial concentration of 30 mg L^{-1} by varying the quantity of adsorbent (0.05, 0.1, 0.15, 0.2, 0.25 and 0.3 g L^{-1}) at 30 °C temperature and pH 8. The experiments were carried out at a contact time of 180 min. As shown in Fig. 5a, the removal of MB shows an increasing trend up to 0.2 g, and beyond that it remains unaltered. At the equilibrium time, the removal shows an increase from 31.42 to 98.52 % with an increment in MSAC dosage from 0.05 to 0.2 g. The increased removal of MB is a result of an enhanced adsorbent surface area and the availability of more adsorption sites.

Effect of the initial concentration of MB on contact time. The effect of initial MB concentration in a range between 10–50 mg L^{-1}, at a fixed adsorbent dosage of 0.2 g at 30 °C temperature and a speed of 160 rpm, was studied and its effect on the adsorption of MB onto MSAC is shown in Fig. 5b. The plots of Fig. 5b can be bifurcated into three different regions:

– Region 1: corresponding to rapid adsorption during the first 30 min.

– Region 2: corresponding to the gradual equilibrium till the equilibrium state for each concentration is reached.

– Region 3: depicting the equilibrium state.

The results show that with an increase in initial MB concentration, a corresponding increase in the adsorption of MB on MSAC is observed. The MB adsorption increased from 52.63 to 198.45 mg g^{-1} at equilibrium, when the initial MB concentration is increased from 10 to 50 mg L^{-1}. Furthermore about this change in MB concentration, the equilibrium removal of MB exhibits a decrease from 99.65 to 79.38 %. This can be attributed to the fact that when the initial concentration increases, the mass transfer driving force increases, resulting in

higher MB adsorption. The comparable trends were obtained in similar studies of adsorption of MB on tea waste.[24]

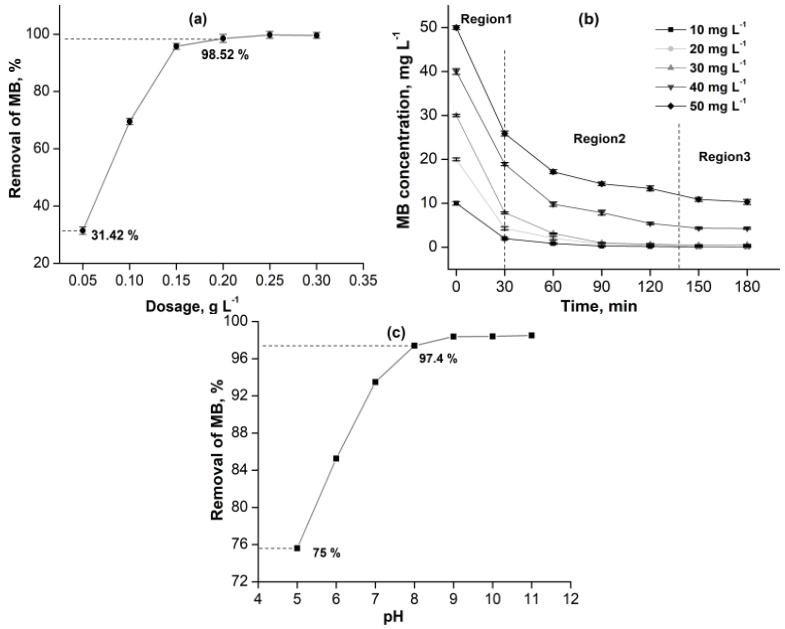

Fig. 5. Effect of: a) MSAC dosage on removal of MB (C_o = 30 mg L^{-1}, pH 8.0); b) contact time and initial concentration on MB adsorption (adsorbent dose = 0.2 g L^{-1}, pH 8.0); c) effect of pH on MB removal (C_o = 30 mg L^{-1}, adsorbent dose = 0.2 g L^{-1}); contact time = 180 min, temperature = 30 °C.

Also, it is evident from Fig. 5b that at an initial concentration ranging between 10 and 30 mg L^{-1}, the adsorption equilibrium is achieved in less than 60 min. However, when the initial MB concentration is increased to 40–50 mg L^{-1}, the corresponding time achieves the equilibrium becomes 150 min. However, the experimentation was carried at 180 min in order to ensure the attainment of the full equilibrium. The dye adsorption follows a sequential process in which at first instance the dye molecules has encounter the boundary layer effect, followed by the diffuse boundary layer film to the adsorbent surface, and finally the diffusion into the porous structure of the adsorbent.[25] Hence, higher initial concentrations of MB solutions will take a relatively longer contact time to attain the equilibrium due to the presence of a higher number of dye molecules.

Effect of pH. pH plays a prominent role in governing the adsorbent capacity in wastewater treatment processes. Fig. 5c presents the effect of pH on MB removal by MSAC. As the pH is changed from 5 to 8 the removal percentage of MB increased from 75 to 97.4 %.

The removal of MB increases rapidly up to pH 8 and then the equilibrium is reached. The maximum percentage removal of about 98.40 % is obtained in a pH range of 9–11. This variation is observed since the adsorption depends on the adsorbent surface and structure of MB.[25] Acidic medium promotes the protonation of MB, however as the pH increases the dye becomes more and more deprotonated. The low MB removal (indicated by dark blue colour) in the lower pH range can be due to the probable development of the positive charge at the MSAC surface, which inhibits MB removal from the dye.[10] However, beyond pH 8, when the medium becomes basic in nature, there seems to be a significant change in polarity, as MB removal increases (solution becomes light blue) monotonically with pH. Thus, a low pH (<6) is the unfavourable use of MSAC. As the initial pH (natural pH 6) of MB solution decreases, the number of negatively charged adsorbent sites decrease and the positively charged sites increases, which does not favour the adsorption of positively charged MB cations due to electrostatic repulsion.[26]

Adsorption isotherm

Distributions of the adsorbed molecules between the liquid and solid phases, when the adsorption process attains an equilibrium state, are shown by the adsorption isotherms. For the design purposes, the suitable models are needed which can be developed by fitting isotherm data into different isotherm models.[26] Various models are proposed in the literature to explain the data about the adsorption isotherms, among which Langmuir and Freundlich are the most commonly used models. In the present work, both models were applied to understand the relationship between the amount of dye adsorbed and its equilibrium concentration.[27]

The linear isotherm equations are as following:

Langmuir:

$$\frac{C_e}{q_e} = \frac{1}{Q_m K} + \frac{C_e}{Q_m} \tag{4}$$

$$R_L = \frac{1}{(1 + KC_o)} \tag{5}$$

Freundlich:

$$\ln q_e = \ln K_f + \frac{1}{n} \ln C_e \tag{6}$$

where is q_e / mg g^{-1}: the amount of adsorbed at the equilibrium time, C_o / mg L^{-1}: the initial solute concentration, C_e / mg L^{-1}: the equilibrium concentration of adsorbate in solution, Q_m / mg g^{-1}: the maximum adsorption capacity corresponding to the complete monolayer coverage, K / L mg^{-1}: the Langmuir constant

related to the energy of the adsorption, K_f, and $1/n$: the empirical constants dependent on the nature of adsorbent and adsorbate. The R_L value implies the favourable adsorption process at a temperature range from 30–50 °C.

Both K_f and $1/n$ are important in selecting an adsorbent as a separating medium, in which K_f / mg g^{-1} is the over-all adsorption capacity and $1/n$ is the heterogeneity factor. The adsorption will be chemical if the $n < 1$, linear if the $n = 1$, and if the $n > 1$ the adsorption will be a physical process.

The adsorption isotherms fitting the two models were shown in Fig. 6. From the values of constants for both isotherm were computed from the slope and the intercept of the linear plot, which and listed in Table III. The R^2 value obtained from the Langmuir isotherm (Fig. 6a) was higher than that obtained from the Freundlich isotherm (Fig. 6b). This evidence suggested that better fitting is achieved by the Langmuir isotherm. The maximum capacity obtained by Langmuir isotherm is 212.76 mg g^{-1}, showing the monolayer coverage and uniform surface adsorption on MSAC. The R_L value implies the adsorption to be unfavourable ($R_L > 1$), linear ($R_L = 1$), favorable ($0 < R_L < 1$) or irreversible ($R_L = = 0$).[28] In the present work value of R_L was found to be 0.0035 and thus it confirms that the prepared AC, MSAC is favourable for the adsorption of MB dye under the conditions used in this study. The values of n higher than unity shows that the adsorption of MB on MSAC is a physical process.

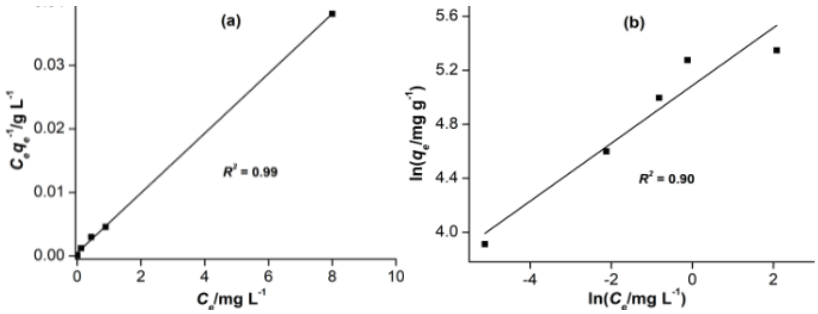

Fig.6. Linearized: a) Langmuir isotherm, b) Freundlich isotherm for MB adsorption by MSAC (pH 8, dosage = 0.2 g L^{-1}, T = 30 °C).

TABLE III. Langmuir, Freundlich adsorption isotherm constant for MB dye on MSAC

Langmuir isotherm			Freundlich isotherm		
Q_m / mg g^{-1}	K / L mg^{-1}	R^2	$1/n$	K_f / mg g^{-1} L mg$^{-1/n}$	R^2
212.76	9.179	0.999	0.2142	160.77	0.90

Adsorption kinetics

The experimentally obtained kinetic adsorption data were subjected to the pseudo-first-order kinetic and the pseudo-second-order kinetic model.[27]

Pseudo-first-order kinetic:

$$\log(q_e - q_t) = \log q_e - \frac{k_1}{2.303}t \quad (7)$$

Pseudo-second-order kinetic:

$$\frac{t}{q_t} = \frac{1}{k_2 q_e^2} + \frac{1}{q_e}t \quad (8)$$

Where is k_1 / 1 min^{-1}: rate constant of first order adsorption, q_e / mg g^{-1}: the amount of solute adsorbed at equilibrium, q_t / mg g^{-1}: the amount of solute adsorbed on the surface of the sorbent at any time, min.

Fig. 7a and b) shows the pseudo-first-order kinetic and pseudo-second-order kinetic model was fitted with the adsorption kinetic data of MB on MSAC. The slope and the intercept were used to calculate the model constant kinetic parameter, and were given with the correlation coefficients (R^2) in Table IV. The correlation coefficient, R^2 for the pseudo-second-order adsorption model has a high value is 0.99, and also its calculated equilibrium adsorption capacity, $q_{e,cal}$ is consistent with the experimental data. These facts suggest that the pseudo-second-order adsorption mechanism is predominant and that the overall rate of the dye adsorption process is chemisorption controlled.

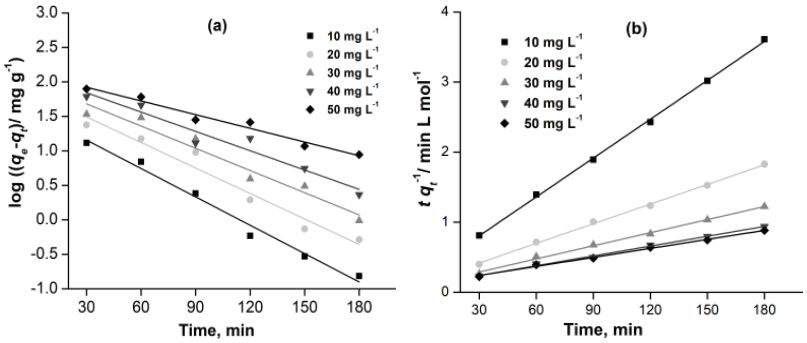

Fig. 7. a) Pseudo-first-order kinetics and b) pseudo-second-order kinetics for MB adsorption by MSAC (pH 8, dosage = 0.2 g L^{-1}, T = 30 °C).

TABLE IV. Pseudo-first- and pseudo-second-order kinetics constant for MB dye on MSAC

C_o / mg L^{-1}	Pseudo-first-order kinetic model				Pseudo-second-order kinetic model		
	$q_{e,exp}$ mg g^{-1}	$q_{e,cal}$ mg g^{-1}	k_1 L min^{-1}	R^2	$q_{e,cal}$ mg g^{-1}	k_2 g mg^{-1} min^{-1}	R^2
10	52.63	36.78	0.031	0.98	54.11	0.00135	1
20	105.1	72.6	0.028	0.94	107.06	0.00063	1
30	156.82	100.83	0.024	0.94	160.51	0.00037	1
40	208.65	132.53	0.021	0.93	213.67	0.00022	1
50	228.33	134.89	0.015	0.96	233.64	0.00016	0.997

Table V presents the adsorption capacities and BET surface area of the various biomass-based AC removal of dye. The surface area of MSAC is 510 m^2 g^{-1}, is about a fivefold increase in surface area as compared to raw MS; also, the surface area of MSAC is comparable to the AC produced from other biomass-based AC, prepared using the same chemical activation route as shown in Table V. It can be inferred that the adsorption capacity of MSAC is quite comparable or even greater than that of some adsorbents reported in references.

TABLE V. Adsorption capacity and BET surface area of other biomass-based AC prepared using H_3PO_4

Material	Dye	Activating agent	BET surface area, m^2 g^{-1}	Adsorption capacity, mg g^{-1}	Reference
MSAC	Methylene blue	H_3PO_4	510	212.76	Present study
Yellow mombin fruit stones	Dianix® royal blue CC	H_3PO_4	551	147.47	14
Tea waste	Methylene blue	–	–	85.16	24
Shrimp shell	Methylene blue	H_3PO_4	506	828	27

Adsorption mechanism for MB

Based on the above results, the activation process and the adsorption mechanism can be represented by Fig. 8. The prepared MSAC is rich in the hydroxyl group on their surface, which is also testified by the FTIR spectra.

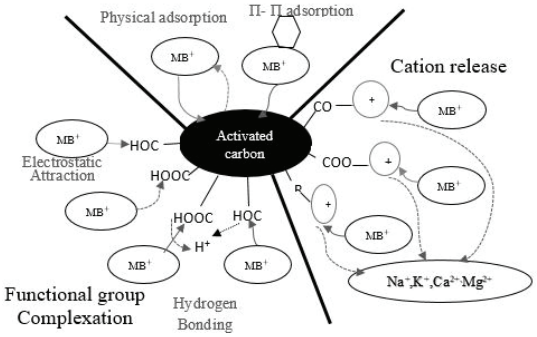

Fig. 8. Mechanism for MB adsorption onto MSAC.

The adsorption of MB by AC can be explained in terms of three major mechanisms: *i*) the electron-donor mechanism, *ii*) the π–π interaction and *iii*) the effect of solvent. An electron-donor mechanism is based on sharing of the electrons which occurs between the MSAC (adsorbent) and MB (adsorbate), the aromatic ring of MB acts as an electron acceptor and the surface functional groups, present on MSAC, act as donor.[29] The π–π interaction occurs due to the charge transfer happening between the π electrons of the benzene ring and the MSAC surface. The third mechanism, namely solvent effect, means that the adsorbed

water molecules have quite a high possibility of being attracted to the surface –O– groups, which leads to the formation of H– bonds between them. However, this interaction inhibits the adsorption capacity, as it may cover active sites on the MSAC.[30]

CONCLUSIONS

The present study shows that MSAC is a good low-cost adsorbent, derived from the agricultural waste. It is well suited for the removal of MB from aqueous solution. The dye adsorption is affected by various factors like adsorbent dosage, contact time, pH, and the concentration of dye. The equilibrium is practically achieved in less than 180 min. The characterization result showed that the BET surface area and the total pores volume of the MSAC is 510 m^2 g^{-1} and 0.32 cm^3 g^{-1}, respectively. Also, it has high carbon content (68.84 %) along with a highly porous surface with cracks, channels, and large holes. The Langmuir and the Freundlich adsorption isotherms are used for the analysis of equilibrium data. The Langmuir model better explains the data. The maximum adsorption capacity obtained was 212.76 mg g^{-1}, with the monolayer coverage of MB molecules at the outer surface of MSAC. The value of R_L was found to be 0.0035 and confirmed that the prepared MSAC is favourable for the removal of MB dye from wastewater. The pseudo-second-order kinetics model is best fitted for MB adsorption onto MSAC. These results show that the MSAC could be applied as a low-cost alternative to the commercial AC in the removal of MB dye from wastewater.

Acknowledgements. The authors would like to thank the staff of Material Research Centre, Malaviya National Institute of Technology, Jaipur (Rajasthan), India, for their kind support to make available analytical instruments. Also, financial help in form of project grant provided by Rajasthan Renewable Energy Corporation, Jaipur, India, is highly acknowledged.

ИЗВОД

АКТИВНИ УГАЉ ОД БИОМАСЕ СТАБЉИКЕ СЛАЧИЦЕ (*Sinapsis alba*) – СИНТЕЗА , КАРАКТЕРИЗАЦИЈА И ПРИМЕНА У ПРЕЧИШЋАВАЊУ ОТПАДНИХ ВОДА

KALPANA PATIDAR и MANISH VASHISHTHA

Department of Chemical Engineering, Malaviya National Institute of Technology, Jaipur 302017, Rajasthan India

Овај рад је фокиусиран на припрему активног угља од стабљика биљке *Sinapsis alba* (MSAC), добијеног хемијском активацијом H_3PO_4, као и испитивањем његове примене у уклањању боја из отпадних вода. Адсорпциони параметри (доза адсорбента, контактно време и pH раствора адсорбата), структура пора, морфологија, површинске функционалне групе, равнотежна кинетика и студија изотерми за уклањање метилен плавог (MB) коришћењем MSAC су такође испитивани. Приказани резултати показују да се доза адсорбента од 0,2 g L^{-1} и pH 8 могу сматрати оптималним за уклањање MB. SEM резултати указују да су поре MSAC веће од пора немодификоване биомасе (MS). Специфична површина добијена BET техником као и укупна запремина пора MSAC износе 510 m^2 g^{-1} и 0,33 cm^3 g^{-1}, редом. Равнотежни адсорпциони подаци корелисани су применом Lang-

muir и Freundlich модела. Боље слагање експерименталних података добијено је применом Langmuir модела са максималним адсорпционим капацитетом od 212,76 mg g^{-1} (MB на MSAC). Бездимензиони фактор, *RL*, указује на повољне услове као и природу сорпционог MSAC–MB система. Адсорпциона брзина најбоље је описана кинетиком псеудо-другог реда, што се може уочити из корелационих резултата. Добијени резултати показују се се адсорбент MSAC може користити у уклањању MB, као обновљива и економски исплатива алтернатива постојећим комерцијалним адосрбентима на бази активног угља.

(Примљено 3. новембра 2020, ревидирано 27. јануара, прихваћено 30. јануара 2021)

REFERENCES

1. I. Bazin, A. Ibn Hadj Hassine, Y. Haj Hamouda, W. Mnif, A. Bartegi, M. Lopez-Ferber, M. De Waard, C. Gonzalez, *Ecotoxicol. Environ. Saf.* **85** (2012) 131 (http://dx.doi.org/10.1016/j.ecoenv.2012.08.003)
2. L. Liu, D. He, F. Pan, R. Huang, H. Lin, X. Zhang, *Chemosphere* **238** (2020) (http://dx.doi.org/10.1016/j.chemosphere.2019.124671)
3. A. H. Jawad, M. Bardhan, A. Islam, A. Islam, S. S. A. Syed-Hassan, S. N. Surip, *Surfaces Interfaces* (2020) 100688 (http://dx.doi.org/10.1016/j.surfin.2020.100688)
4. V. Katheresan, J. Kansedo, S. Y. Lau, *J. Environ. Chem. Eng.* **6** (2018) 4676 (http://dx.doi.org/10.1016/j.jece.2018.06.060)
5. M. Rafatullah, O. Sulaiman, R. Hashim, A. Ahmad, *J. Hazard. Mater.* **177** (2010) 70 (http://dx.doi.org/10.1016/j.jhazmat.2009.12.047)
6. B. Hu, Y. Ai, J. Jin, T. Hayat, A. Alsaedi, L. Zhuang, X. Wang, *Biochar* **2** (2020) 47 (http://dx.doi.org/10.1007/s42773-020-00044-4)
7. W. Xing, X., Jiang, W., Li, S., Zhang, X. and Wang, *Waste Manage.* **89** (2019) 64 (http://dx.doi.org/https://doi.org/10.1016/j.wasman.2019.04.002)
8. A. Kumar, H. Gupta, *Environ. Technol. Innov.* **20** (2020) (http://dx.doi.org/10.1016/j.eti.2020.101080)
9. S. Charola, H. Patel, S. Chandna, S. Maiti, *J. Clean. Prod.* **223** (2019) 969 (http://dx.doi.org/10.1016/j.jclepro.2019.03.169)
10. R. K. Gautam, A. Mudhoo, M. C. Chattopadhyaya, *J. Environ. Chem. Eng.* **1** (2013) 1283–1291 (http://dx.doi.org/10.1016/j.jece.2013.09.021)
11. D. Garg, C. B. Majumder, S. Kumar, B. Sarkar, *J. Environ. Chem. Eng.* **7** (2019) (http://dx.doi.org/10.1016/j.jece.2019.103365)
12. S. Archin, S. H. Sharifi, G. Asadpour, *J. Clean. Prod.* **239** (2019) (http://dx.doi.org/10.1016/j.jclepro.2019.118136)
13. Y. Gao, Q. Yue, B. Gao, A. Li, *Sci. Total Environ.* **746** (2020) 141094 (http://dx.doi.org/10.1016/j.scitotenv.2020.141094)
14. M. J. P. Brito, C. M. Veloso, L. S. Santos, R. C. F. Bonomo, R. da C. I. Fontan, *Powder Technol.* **339** (2018) 334 (http://dx.doi.org/10.1016/j.powtec.2018.08.017)
15. R. T. Zrybko, C.L., Fukuda, E.K. and Rosen, *J. Chromatogr. A* **767** (1997) 43–52 (http://dx.doi.org/https://doi.org/10.1016/S0021-9673(96)01068-0)
16. Statista, https://www.statista.com/statistics/263930/worldwide-production-of-rapeseed-by- country (visited October 25, 2020)
17. T. C. Purohit, P., Tripathi, A.K. and Kandpal, *Energy* **31** (2006) 1321 (http://dx.doi.org/10.1016/j.energy.2005.06.004)
18. K. Patidar, M. Vashishtha, *Water Air Soil Pollut* **231** (2020) 526 (https://doi.org/10.1007/s11270-020-04893-4)

19. S. Maiti, S. Purakayastha, B. Ghosh, *Fuel* **86** (2007) 1513 (http://dx.doi.org/10.1016/j.fuel.2006.11.016)
20. D. Vamvuka, E. Kakaras, E. Kastanaki, P. Grammelis, *Fuel* **82** (2003) 1949 (http://dx.doi.org/10.1016/S0016-2361(03)00153-4)
21. A. Kumar, H. M. Jena, *Results Phys.* **6** (2016) 651 (http://dx.doi.org/10.1016/j.rinp.2016.09.012)
22. S. J. C. E. J. Prahas, D. Kartika, Y. Indraswati, N. Ismadji, *Chem. Eng. J.* **140** (2008) 32 (http://dx.doi.org/https://doi.org/10.1016/j.cej.2007.08.032)
23. Y. Sun, H. Li, G. Li, B. Gao, Q. Yue, X. Li, *Bioresour. Technol.* **217** (2016) 239 (http://dx.doi.org/10.1016/j.biortech.2016.03.047)
24. M. T. Uddin, M. A. Islam, S. Mahmud, M. Rukanuzzaman, *J. Hazard. Mater.* **164** (2009) 53 (http://dx.doi.org/10.1016/j.jhazmat.2008.07.131)
25. S. Senthilkumaar, P. R. Varadarajan, K. Porkodi, C. V. Subbhuraam, *J. Colloid Interface Sci.* **284** (2005) 78 (http://dx.doi.org/10.1016/j.jcis.2004.09.027)
26. K. Aisan, H. Z. Mousavi, R. Alimorad, H. Shirkhanloo, *J. Serbian Chem. Soc.* **83** (2018) 651 (http://dx.doi.org/10.2298/JSC170827112K)
27. L. Liu, X. He, C. Yu, X. Bai, Y. Ye, L. Wang, B. Zhang, *Powder Technol.* **326** (2018) 181 (http://dx.doi.org/https://doi.org/10.1016/j.powtec.2017.12.034)
28. K. C. Bedin, A. C. Martins, A. L. Cazetta, O. Pezoti, V. C. Almeida, *Chem. Eng. J.* **286** (2016) 476 (http://dx.doi.org/10.1016/j.cej.2015.10.099)
29. Y. Tang, Y. Zhao, T. Lin, Y. Li, R. Zhou, Y. Peng, *J. Environ. Chem. Eng.* **7** (2019) (http://dx.doi.org/10.1016/j.jece.2019.103398)
30. S. Fan, Y. Wang, Z. Wang, J. Tang, J. Tang, X. Li, *J. Environ. Chem. Eng.* **5** (2017) 601 (http://dx.doi.org/10.1016/j.jece.2016.12.019).